HAL
archives-ouvertes.fr

Transverse momentum balance of b-jet pairs in PbPb collisions with the CMS experiment at the LHC

Stanislav Lisniak

▶ **To cite this version:**

Stanislav Lisniak. Transverse momentum balance of b-jet pairs in PbPb collisions with the CMS experiment at the LHC. High Energy Physics - Experiment [hep-ex]. Université Paris-Saclay, 2016. English. NNT : 2016SACLX069 . tel-01490097

HAL Id: tel-01490097

https://pastel.archives-ouvertes.fr/tel-01490097

Submitted on 14 Mar 2017

HAL is a multi-disciplinary open access archive for the deposit and dissemination of scientific research documents, whether they are published or not. The documents may come from teaching and research institutions in France or abroad, or from public or private research centers.

L'archive ouverte pluridisciplinaire **HAL**, est destinée au dépôt et à la diffusion de documents scientifiques de niveau recherche, publiés ou non, émanant des établissements d'enseignement et de recherche français ou étrangers, des laboratoires publics ou privés.

NNT : 2016SACLX069

Thèse de doctorat de l'Université Paris-Saclay préparée Ecole Polytechnique

Ecole doctorale n°576
Particules, Hadrons, Énergie, Noyau, Instrumentation, Imagerie, Cosmos et Simulation (PHENIICS)
Spécialité de doctorat: Physique des particules

par

M. Stanislav Lisniak

L'asymmétrie de l'impulsion transverse des paires des jets de b dans les collisions d'ions lourds dans l'expérience CMS au LHC

Thèse présentée et soutenue à Ecole Polytechnique, le 27 octobre 2016.

Composition du Jury :

M.	Hervé Borel	Chercheur CEA Service de Physique Nucléaire, CEA	(Président du jury)
M.	Matthew Nguyen	Chargé de recherche Laboratoire Leprince-Ringuet	(Directeur de thèse)
Mme.	Brigitte Cheynis	Directeur de recherche Institut de Physique Nucleaire de Lyon	(Rapporteur)
M.	Julien Faivre	Maître de conférences Laboratoire de physique subatomique et de cosmologie de Grenoble	(Rapporteur)

Résumé

Les collisions d'ions lourds à haute énergie produisent un nouvel état de la matière appelé le plasma de quarks et de gluons. Une des signatures les plus manifestes du plasma de quarks et de gluons est le phénomène de jet quenching. La perte d'énergie des partons traversants le QGP résulte dans une suppression de la section efficace, autant que dans un déséquilibre des paires de jets. Dans cette thèse, le jet quenching est sondé via le déséquilibre de l'impulsion transverse de paires de jets. Une telle étude a déjà été conduite pendant le run 1 du LHC. Le but principal de cette thèse est d'identifier le quenching des jets issus de quarks b. La comparaison du quenching des jets de b à celui de jets non-identifiés nous renseigne sur la dépendence de la parte d'énergie en la saveur des quarks, mais également sur la différence entre le quenching des quarks et des gluons.

Le chapitre 1 de cette thèse motive les mesures effectuées en présentant les mesures passées de sondes du QGP. Dans le chapitre 2, sont présentés le détecteur CMS et les générateurs de simulation utilisés dans cette thèse. Les échantillons simulés utilisés sont également décrits. Les objets physiques, tels que trajectoires ou jets, ne sont pas directement mesurés par le détecteur mais doivent être reconstruits à partir des données brutes, tels que signaux dans le trajectomètre ou tours du calorimètre. Cette reconstruction d'objets est décrite au chapitre 3. Les trajectoires sont reconstruites à partir des coups dans le trajectomètre, grâce à des algorithmes de "tracking". Le tracking fut une part majeure du travail de thèse. Son résultat en est que les trajectoires déplacées, issues de saveurs lourdes, sont recouvrées pendant le tracking, rendant possible l'analyse présentée. De plus, la rapidité de la reconstruction a été substantiellement améliorée, un point crucial pour les algorithmes de déclenchement qui reconstruisent les événements en ligne, rendant leur acquisition possible. À l'aide d'une approche multivariée, la sélection

des trajectoires a également été améliorée et un gain d'efficacité de 10% obtenu, pour un taux de trajectoires fortuites identique.

L'analyse du déséquilibre d'impulsion transverse est présentée au chapitre 4. De manière à enregistrer autant de données que possible dans la bande passante disponible, le déclenchement de haut niveau a été utilisé. Deux analyses sont conduites en parallèle : le déséquilibre en impulsion transverse des jets inclusifs (non-identifiés) et des jets de b. L'analyse de paires de jets devient délicate dans les collisions PbPb centrales du fait de la présence d'un fond combinatoire. Des interactions dures multiples sont en effet probables dans les collisions d'ions lourds centrales. Il en résulte que le "second" jet d'une interaction dure peut être éclipsé par un "premier" jet d'une autre interaction, et ainsi perdu. Pour résoudre ce problème, le fond combinatoire est soustrait et l'inefficacité corrigée. L'analyse des paires de jets de b diffère de l'analyse inclusive par l'application d'un algorithme d'étiquetage sur les deux jets. Puisque l'efficacité de l'étiquetage dépend de la cinématique du jet de b, les corrections d'efficacité sont calculées en fonction de la centralité de l'événement, et de l'impulsion ou la pseudorapidité du jet. Le résultat est la mesure, pour la première fois, du déséquilibre des paires de jets de b, et une comparaison à celui des jets inclusifs. Il est observé que les jets de b sont atténués d'une façon similaire aux jets inclusifs. Le chapitre 5 comprend une discussion des résultats au moyen d'un modèle simple de perte d'énergie. L'ajustement combiné du facteur de modification nucléaire et du déséquilibre des impulsions transverse nous éclaire sur les mécanismes sous-jacents de pertes d'énergie. Pour conclure, les améliorations possibles futures de l'analyse sont discutés.

Acknowledgments

First of all, I would like to express my gratitude to countless people who operate at CMS and LHC and deliver high performance of these amazing and extremely complicated machines. This dissertation was performed under the attentive supervision of Matthew Nguyen. His guidance during the analysis of data and careful reading of the manuscript has made it what it is now and also shaped me as a physicist, as a researcher, as a person. Whatever I am today is the result of a long list of random events and deliberate choices. Your motivation was crucial in the moments I thought I have lost, your passion – in the moments of despair, your advices – in the moments of stupidity. Thank you, Matt, for being such an incredible supervisor!!! It was also great to work together with Yetkin Yilmaz, to clash with him sometimes during coffee-time in order to become a little bit more open-minded. I am grateful to jury members, Hervé Borel, Brigitte Cheynis and Julien Faivre, for the comments and questions which significantly improved the manuscript. The work was done in the Laboratoire Leprince-Ringuet, and I am really grateful to Jean-Claude Brient, Pascal Paganini, Frederic Fleuret, Raphael Granier de Cassagnac and the wonderful staff of the lab for the environment that is created for the researchers and for me particularly. My special thanks to Ludwik Dobrzynski, for his advice to enter the Master program of Ecole Polytechnique and the support during the doctoral thesis. I am indebted to professor Vladimir Skalozub who set me on the path of learning high energy physics and fired my curiosity about the quark gluon plasma. I am very thankful to my friend Afi Aflatooni whose support was crucial at many points in my life. Finally, I would like to thank my wife Olia for being my inspiration and support throughout three years of this thesis, and simply for making this world so wonderful!

Contents

List of Figures

List of Tables

Introduction

1.1 Historical developments

1.1.1 The rise and glory of quantum chromodynamics

The first step towards identifying the nuclear structure of matter came when E. Rutherford scattered alpha particles off a thin gold foil in 1909 [38]. A century later, as we shall discuss, scientists at the Relativistic Heavy Ion Collider (RHIC) were again using gold nuclei, but this time to explore the *sub*nuclear structure of matter. Rutherford's discovery of the atomic nucleus was later complemented by his discovery of the proton [39] and of the neutron by J. Chadwick in 1932 [40] which completed the nuclear model.

By that time, the merging of special relativity with quantum mechanics had been achieved by P. Dirac who had also noticed that his equation simultaneously described particles with positive and negative energy. Simplifying, this is the consequence of the fact that the main relation of the special relativity $E^2 - p^2 = m^2$ defines energy only up to a sign. Particles with a "negative" energy were later associated to the anti-electron, or positron, which was discovered in the same year of 1932 by C. D. Anderson [41].

There is a universal principle, the principle of least action, which allows one to express any physical law in the form of a single function – the Lagrangian $\mathcal{L}$ – and to deduce the physics by the requirement of the minimum action $S = \int d^4x\mathcal{L}$. In the Lagrangian formalism, one can combine Dirac's equation of the electron and

Maxwell's equations of the electromagnetic field into a single function:

$$\mathcal{L}(A_\mu, \bar{\psi}, \psi) = \bar{\psi}(i\gamma^\mu D_\mu - m)\psi + F_{\mu\nu}F^{\mu\nu}, \tag{1.1}$$

where ψ is the (so far, classical) fermion field with mass parameter m and charge e, and $F_{\mu\nu} = \partial_\mu A_\nu - \partial_\nu A_\mu$ is the tensor of the electromagnetic field where A_μ represents the electromagnetic potential. The covariant derivative $D_\mu = \partial_\mu - ieA_\mu$ allows the fermion field (in this case, electrons and positrons) to interact with the boson field (photons). Substituting the Lagrangian into the Lagrange-Euler equations one obtains Maxwell's and Dirac's equations of classical electromagnetism.

The Maxwell equations have a symmetry which was crucial to the physics in 20th century: gauge invariance. One can change the value of the potential with the so-called *gauge transformation*,

$$A'_\mu(x) = A_\mu(x) - \partial_\mu \alpha(x), \tag{1.2}$$

for an arbitrary function $\alpha(x)$, while the physical quantities of electrical and magnetic fields $\vec{E}$ and $\vec{B}$ will not change. The Lagrangian 1.1 is also invariant under this transformation if one changes the fermion field as $\psi'(x) = U(x)\psi(x) = e^{-i\alpha(x)}\psi(x)$. This is called the U(1) symmetry and is directly connected to the electric charge of the field. Indeed, according to the Noether's theorem [42], every symmetry corresponds to a conserved current. In the case of the U(1) symmetry the conserved current is the electromagnetic current: $J^\mu = e\bar{\psi}\gamma^\mu\psi$ with the conservation law $\partial_\mu J^\mu = \partial\rho/\partial t + \nabla \cdot \vec{j} = 0$.

By analogy with quantum mechanics, where quantum equations can be achieved from classical ones by replacing the phase-space coordinate (position and momentum) of a particle by the corresponding operators, quantum fields can be obtained from classical fields by making them operators. Note that as opposed to the classical particle with 6 degrees of freedom, the field has infinite number of degrees of freedom. This was done by P. Dirac who considered the field as an infinite ensemble of the harmonic oscillators, and introduced the idea of creation and annihilation operators to the quantum field. This has led to the appearance of the

quantum electrodynamics (QED). The fortunate situation that the electromagnetic coupling constant $\alpha = e^2/4\pi = 1/137$ is small allowed the derivation of the electromagnetic interaction in a perturbative series expanded around α. Thus, one can calculate the physical quantity up to some order and be assured that the next order would bring only smaller corrections than the previous one. QED calculations were extremely successful and allowed to predict any process involving electrons and photons. In fact, the current QED computations of the anomalous magnetic moment [43] agree with the experimental value with up to 10 significant figures making it the most accurate prediction in the history of physics.

There was a huge problem behind the success of QED. Any computation beyond the tree-level diagram (i.e. the leading order of the perturbative expansion) has lead to the infinite result. The source of the divergence is that at very short length-scales (smaller than the Compton length $\hbar/mc$) the uncertainty principle allows the creation of new (virtual) particles for a very short period of time. But the closer one looks, the more one sees! The summation over all such virtual states returns a divergent result. Surprisingly, H. Bethe was able to compute the precise value of the Lamb shift of the hydrogen atom which is due to "the interaction of the electron with the radiation field. This shift comes out infinite in all existing theories, and has therefore always been ignored." [44]. His idea was that "this effect should properly be regarded as *already included in the observed mass of the electron*". In total, there are only 3 divergent contributions in QED, connected to the self-energy of the electron, photon and their interactions. As a result, one can *renormalize* the bare value of the photon and electron fields and the electron charge so that the renormalized value contains only the finite terms. One measures the electron charge only through its interaction with the electromagnetic field hence there is no reason to assume that the bare value in the Lagrangian coincides with what we measure. For a deep but amusing discussion about renormalization see the conversation between Mr. Egghead Theorist and Smart Experimentalist in part III of "Quantum Field Theory in a Nutshell" by A. Zee [45]. Surprisingly, while the theory of renormalization was born through the marriage of $\hbar$ and c, its consequences lie well beyond the quantum theory. K. Wilson applied its methods to statistical mechanics [46], where the divergent correlations near the critical

point behave similarly. For a review of the renormalization without application to the field theory see Ref. [47].

The consequence of renormalization is of the utmost importance for all of high energy physics. Given the physical value at one energy scale, one can calculate it at another energy scale. In particular, the coupling constant α in QED increases with the energy scale q as

$$\alpha(q^2) = \frac{e^2}{4\pi} = \frac{\alpha(\mu^2)}{1 - \frac{\alpha(\mu^2)}{3\pi}\log\frac{q^2}{\mu^2}}, \tag{1.3}$$

where μ is some previous energy scale at which the coupling was found, e.g. at the electron mass at rest $\mu = m_e$ the coupling $\alpha = 1/137$. The coupling constant grows with the energy: at rest it is equal to 1/137 while at the energy of Z boson mass it is equal to 1/128, as measured in e^+e^- collisions at LEP [48]. The intuition behind the running coupling is the *vacuum polarization phenomenon*: the (infinite) bare electron charge interacts with the vacuum around it and creates multiple electron-positron (in general, fermion-antifermion) pairs around it, thus "screening" its electric charge. With increasing energy (smaller distances) one penetrates this screening layer and starts to see the bare charge [49].

The development of QED was accompanied by extensive research on the experimental side. The study of cosmic rays led to the discovery of the muon, pion, kaon and to hundreds of hadrons of different masses. In 1960s the diversity of particles which were considered all elementary was referred to as a "particle zoo", and a reductive classification of them was highly sought. The situation became more clear with the hypothesis that all hadrons are composed of quarks by M. Gell-Mann and Z. Zweig [50, 51]. While the model was quite successful, the Ω^- baryon was composed of three strange quarks, which seems to violate the Pauli exclusion principle (because quarks are fermions). This suggested the existence of a new quantum number later called *color*. Another mystery of that time was the strong interaction which binds the atomic nucleus. Since the strong force is short range, its mediator must be massive, and based on these arguments H. Yukawa predicted the π meson [52]. However both these problems were finally solved with the creation of the quantum chromodynamics (QCD).

Quantum chromodynamics is a quantum field theory based on the non-Abelian gauge symmetry group SU(3) [49]. The transformation of the matter field is similar to electrodynamics: $\psi = U\psi$ but now U is an element of the SU(3) group which can be defined as a set of 3x3 unitary matrices satisfying the conditions $\det U = 1$ and $U^\dagger U = 1$. This translates into 8 independent values in the matrix and hence there are 8 generators of the group $T^a = 1/2\lambda_a$, where λ_a are 3x3 Gell-Mann matrices defined elsewhere [53]. The generators of the group define the Lie algebra $[T^a, T^b] = f^{abc}T^c$, where f^{abc} are antisymmetric structure constants. The form of the Lagrangian is similar to Eq. 1.1, but now the gauge transformation of the field has to be defined as $A'_\mu = UA_\mu U^\dagger + iU\partial_\mu U^\dagger$, while the gauge (gluon) field itself is multicomponent: $A_\mu = A^a_\mu T^a$. The field tensor $F_{\mu\nu} = F^a_{\mu\nu}T^a$ is defined as $F^a_{\mu\nu} = \partial_\mu A_\nu - \partial_\nu A_\mu + f^a_{bc}A^a_\mu A^a_\nu$.

The Yang-Mills Lagrangian is an analog of the Maxwell's equations in the non-Abelian case:

$$\mathcal{L} = -\frac{1}{4g^2}F^a_{\mu\nu}F^a_{\mu\nu} \tag{1.4}$$

Although the Yang-Mills Lagrangian looks very similar to the QED photon field, there are principle differences: it contains self-interacting terms of the 3rd order $f^{abc}A^{b\mu}A^{c\nu}\partial_\mu A^a_\nu$ and 4th order like $(f^a_{bc}A^a_\mu A^b_\nu)^2$. This means that gluons interact with themselves. The corresponding non-linear Yang-Mills equations cannot yet be solved analytically and are among seven "Millennium prize problems" defined by Clay Mathematics Institute [54].

The perturbative approach to quantum chromodynamics was very fruitful. It was found in the experiment, for example, by measuring ratio of e^+e^- cross-sections into hadrons to into muons, that the number of colors is 3 [55]. But as in the case with QED, QCD diagrams become divergent in the expansion. Renormalization has saved the situation again, proving that QCD is the appropriate physical theory. However, the non-Abelian nature of the gluon field made the QCD coupling of the strong interaction behave differently from the QED:

$$\alpha_s(q^2) = \frac{g^2}{4\pi} = \frac{\alpha_s(\mu^2)}{1 + \frac{\alpha_s(\mu^2)}{4\pi}(11 - \frac{2}{3}N_f)\log\frac{q^2}{\mu^2}}, \tag{1.5}$$

where N_f is a number of flavors. It decreases with increasing energy (decreasing distance)! Indeed this was observed in multiple experiments and is summarized in Fig. 1.1. The reason behind this different behavior is the ability of the gluon field to interact with itself which produces an "anti-screening" effect.

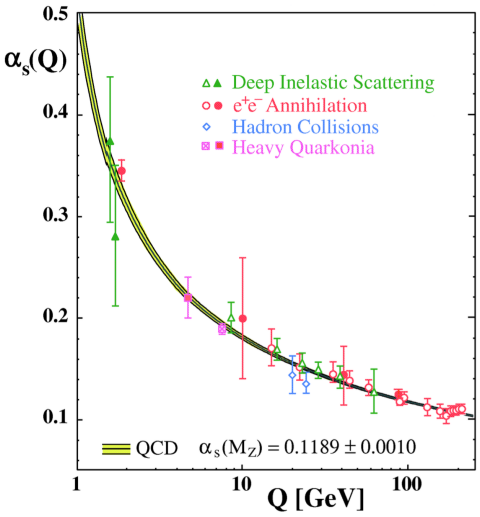

Figure 1.1: Experimental measurements of the strong coupling at different energies [1].

This phenomenon, also referred to as an *asymptotic freedom*, justifies the use of the perturbative approach at high energies where the coupling constant becomes small. On the other hand, at low energy α_s is of the order of unity and the expansion breaks down. Another problem of QCD is that free quarks are not observed in nature. This property, known as *confinement*, can be explained with the quark interaction potential increasing with the distance between them. When the distance becomes too large a quark-antiquark pair can be produced from the energy of the interaction. As a result, two quark-antiquark pairs appear and no free quark is observed.

1.1.2 QCD on the lattice

The rise of computing power in the second half of the 20th century gave rise to numerical computations in theoretical physics. Quantum field theory was not an exception and lattice QCD methods were developed. In order to formulate the infinite-dimensional field theory on the finite lattice one has to formulate

the quantum field theory by means of functional methods. This approach was first introduced by P. Dirac [56] and later developed by R. Feynman [57]. The idea behind this brilliant method relies on the superposition principle of quantum mechanics. As defined in Ref. [57]: "In quantum mechanics the probability of an event which can happen in several different ways is the absolute square of a sum of complex contributions, one from each alternative way. The probability that a particle will be found to have a path $x(t)$ lying somewhere within a region of space time is the square of a sum of contributions, one from each path in the region. The contribution from a single path is postulated to be an exponential whose (imaginary) phase is the classical action (in units of $\hbar$) for the path in question. The total contribution from all paths reaching x, t from the past is the wave function $\psi(x, t)$. This is shown to satisfy Schroedinger's equation."

Formally, the total amplitude of transition between point a and b can be written as

$$\sum_{allpaths} e^{iS/\hbar} = \int \mathcal{D}x(t) e^{iS[x(t)]/\hbar} = \int \mathcal{D}x(t) e^{i/\hbar \int d^4x \mathcal{L}[x(t)]}, \tag{1.6}$$

where the integration is performed over all possible paths $x(t)$ the particle can propagate from a to b, and $S[x(t)]$ corresponds to the classical action. The field has an infinite number of degrees of freedom and must be integrated among any possible field configurations, but generally the amplitude can be written in a similar manner. E.g. for a field ϕ, the amplitude can be written in the form ($\hbar$ is omitted)

$$\int \mathcal{D}[\phi] e^{i \int d^4x \mathcal{L}(\phi)}. \tag{1.7}$$

At this moment, the time is real. For lattice computations it is useful to make a Wick's rotation into the imaginary time: $t \to it$. Such a translation changes the metric to Euclidean and moreover the action becomes

$$iS = i \int dt d^3x \mathcal{L} \to S_E = -\int d^4x \mathcal{L}_E. \tag{1.8}$$

After that, the path integral

$$Z = \int \mathcal{D}[\phi] e^{-S_E} \tag{1.9}$$

is also called the partition function and is the central subject of statistical mechanics. One can use Monte-Carlo methods such as the Metropolis-Hasting algorithm [58] to construct a canonical ensemble with a probability of states proportional to e^{-S_E}. The idea to discretize space-time and define QCD on the lattice belongs to K. Wilson [59]. Lattice QCD is constructed as follows:

- space-time is discretized by N_S space sites and N_T time sites with a lattice parameter a. The continuum limit is achieved by $a \to 0$. Any derivative is replaced by a finite difference.

- the gauge field is defined by means of the *link* variables $U_\mu(n) = e^{iagA^a_\mu T^a}$, where n is the space-time discretized position and A^a_μ are components of the gauge field. Such a variable is a unitary matrix defined for the edge which connects sites n and $n+\mu$. In order to obtain a gauge independent Lagrangian, one needs to set constraints on the link variables: $U_\mu(n)' = \Omega(n)U_\mu(n)\Omega^\dagger(n+\mu)$, where $\Omega(n)$ is the SU(3) gauge transformation, i.e. under the gauge transformation link variables are multiplied at their ends. One can easily check then that the product of link variables along any path transforms in a similar way. This means that any closed path is *gauge invariant*.

- The smallest such path is called a *plaquette* and is defined as $U_{\mu\nu}(n) = U_\mu(n)U_\nu(n+\mu)U_{-\mu}(n+\mu+\nu)U_{-\nu}(n+\mu)$, as shown in Fig. 1.2.

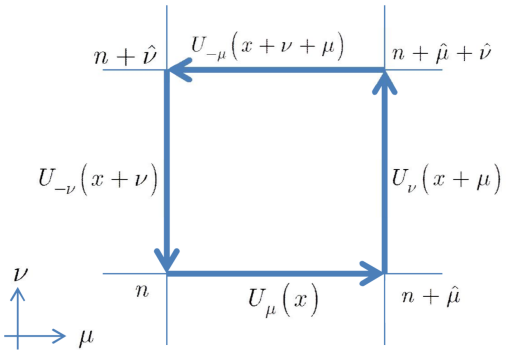

Figure 1.2: The smallest closed loop of links on the lattice, the plaquette.

One can show then that $U_{\mu\nu}(n) = exp[ia^2F_{\mu\nu}(n)+O(a^3)]$. The Wilson gauge

action

$$S_G = \frac{2}{g^2} \sum_n \sum_{\mu<\nu} \mathbb{R}\mathrm{e}\,\mathrm{Tr}[1 - U_{\mu\nu}(n)] \tag{1.10}$$

tends to the continuous Yang-Mills action in the limit of vanishing lattice parameter $S_G = \frac{a^4}{2g^2} \sum_n \sum_{\mu,\nu} \mathrm{Tr}[F^2_{\mu\nu}(n)]$.

- Now, by updating link variables with probabilities $P \sim e^{-S_G}$ one can construct canonical ensemble and extract non-perturbative properties of gluon field on any commercially available laptop.

The quark field is defined on the lattice sites, but unfortunately there is no unique and unambiguous method to define quarks on the lattice and this is still an active field of research. For a comprehensive review of lattice QCD physics see Ref. [60].

Lattice computations allow one to predict non-perturbative effects. For example, Fig. 1.3 presents the results of the lattice computation of light hadron masses by Budapest-Marseille-Wuppertal collaboration showing an excellent agreement to the experimental data. The masses of light quarks have to be fixed. Therefore, π and K-mesons are treated as input to the calculations.

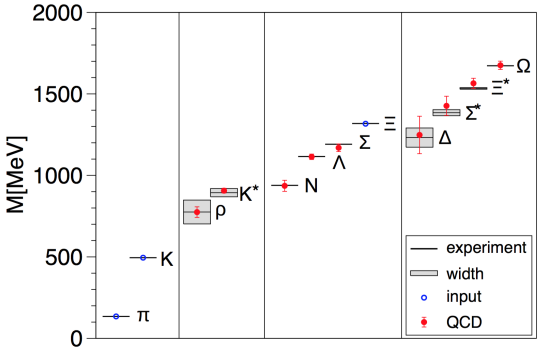

Figure 1.3: Light hadron spectrum in QCD from lattice computations by Budapest-Marseille-Wuppertal collaboration and comparison to experimental data. [2].

As was mentioned above, the trace of any product of link variables along the closed curve is gauge invariant making a physical observable. An important variable that falls into this class is the Wilson line, which is the trace of the product of the link variables along the space dimension by the distance r, then time dimension t and in the reverse direction r and t to close the loop. The associated quantity is the Polyakov loop, which is defined at the site of the lattice and is the product of links

along the temporal direction: $P(\vec{n}) = \mathrm{Tr} \prod_{j=1}^{N_T} U_4(\vec{n}, j)$. It can be shown that the correlation of Polyakov's loops can be used to identify the potential $F_{q\bar{q}}$ between quarks located at spatial sites n and m:

$$\langle P(m) P(n)^\dagger \rangle \sim e^{-aN_T F_{q\bar{q}}(|m-n|)}. \tag{1.11}$$

The result of such a computation is shown in Fig. 1.4 (left) from Ref. [3]. The linear increase of the quark-antiquark potential is direct evidence of the confinement mechanism. In fact, the string between quark and anti-quark can also be observed on the lattice as on Fig. 1.4 (right) [4].

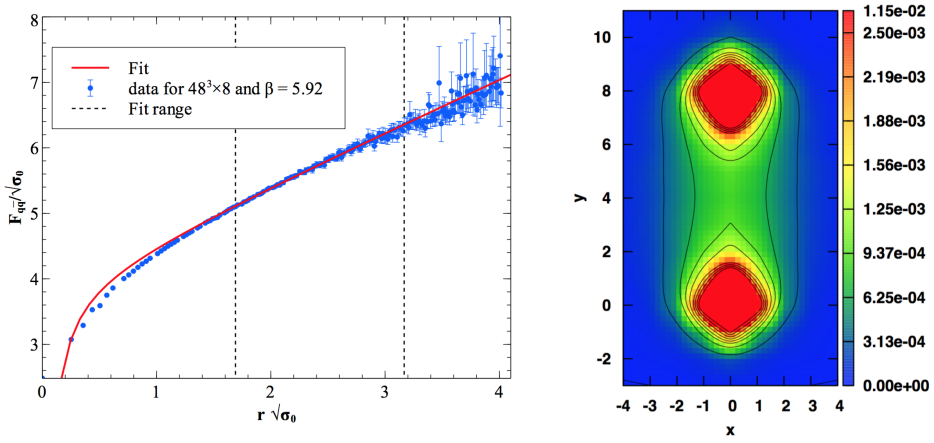

Figure 1.4: String tension derived from the lattice computations [3] (left) and Lagrangian density of a system with a static quark-antiquark pair [4] (right).

When two quarks become separated in space, the Polyakov loop $\langle P(n) \rangle \sim e^{-aN_T F_{q\bar{q}}(\infty)}$ becomes the measure of the energy of the free quark. In the *confinement phase*, where free quarks are not observed, it should be infinite, and hence the $\langle P(n) \rangle = 0$, while in the *deconfinement phase* where the quark may be found free, $\langle P(n) \rangle \neq 0$, thus serving as an order parameter. The deconfinement phase is also called a *quark-gluon plasma* (QGP) (the term was proposed by E. Shuryak in [61]), emphasizing the fact that quarks are free in this state. Such a transition is shown on Fig. 1.5 (left) from calculations in Ref. [5]. Other thermodynamical calculations can be also performed on the lattice. For example, Fig. 1.5 (right) shows the computations of the pressure as a function of temperature for different QCD systems [6]. One can see that even at very high temperatures the pressure of the

ideal gas limit (depicted with arrows) is not achieved which indicates the presence of strong interactions between the constituents.

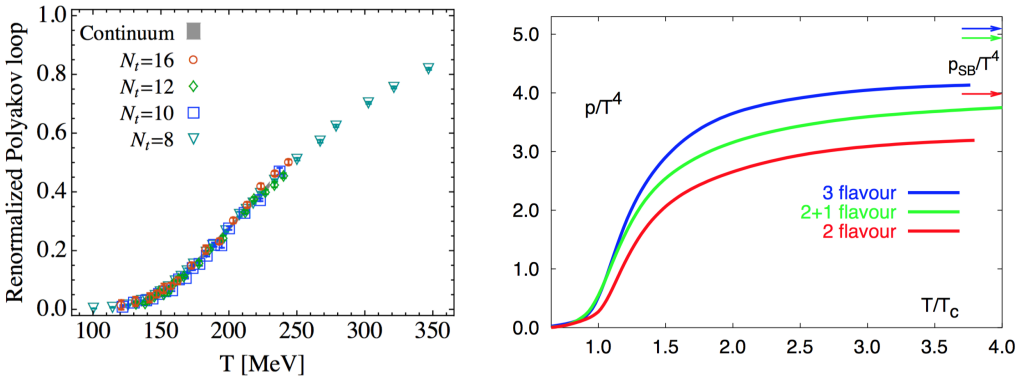

Figure 1.5: Polyakov loop as a function of the lattice temperature (left) [5] and the pressure in lattice QCD as a function of temperature (right) [6]

In the limit of infinite quark masses when only the gluon field is simulated, the nature of the confinement-deconfinement phase transition is believed to be of the first order. As incorporating small quark masses into lattice computations became feasible, it turned out that in the physical region the transition is a smooth *crossover* (Fig. 1.6) with a transition temperature of around $T_c \sim 170$ GeV (or, equivalently, 2 trillion Kelvin).

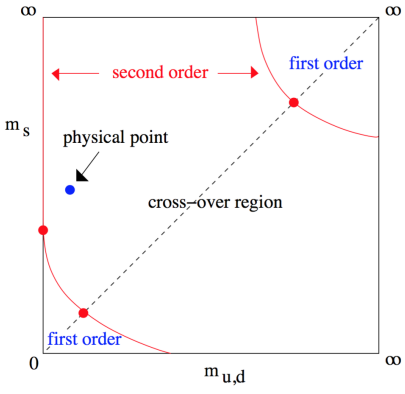

Figure 1.6: The critical behavior of QCD for different quark masses [7]

According to the computations, the energy density at which the transition occurs is $\epsilon_c \sim 1$ GeV/fm^3. Is it achievable in the experiment?

Based on geometrical considerations, Bjorken [62] connected the energy of the

outgoing particles at central rapidity $\frac{dE_T}{dy}$ with the energy density:

$$\epsilon = \frac{1}{\pi R^2} \frac{1}{c\tau} \frac{dE_T}{dy}, \tag{1.12}$$

where R is the nuclear radius and τ is the effective thermalization timescale. For a thermalization time of 1 fm/c, he estimated that collisions at the SPS collider would achieve and energy density of around 1 GeV/fm^3. At RHIC the calculation was improved and the energy density was estimated to be about 5 GeV/fm^3 [63]. The corresponding energy density achieved with the LHC was estimated in heavy ion collisions at $\sqrt{s} = 2.76$ TeV to be 14 GeV/fm^3 [64]. This is well above the critical energy density for a QGP phase transition.

1.2 The QGP in heavy ion experiments

The temperature achieved in heavy ion experiments is above the deconfinement transition, and as we will see they indeed provide evidence of a new state of matter. But in order to interpret heavy ion collision data, they must be connected to data from proton-proton collisions where the QGP is not expected to be formed. This is done with help of the Glauber model, described below. Later in this section we will briefly describe the impact of the quark-gluon plasma on energetic partons from hard scattering. This will allow us to review and interpret the results of heavy ion collisions in the latest collider experiments.

1.2.1 Collision centrality

The Glauber model is an essential instrument in the experimentalist's toolbox, providing a connection between proton-proton and nucleus-nucleus collisions. It was first introduced by Glauber in 1959 [65]. The discussion here follows Ref. [8].

A heavy nucleus can be regarded as an extended object consisting of multiple nucleons which are distributed according to the Fermi distribution:

$$\rho(r) = \rho_0 \frac{1 + w(r/R)^2}{1 + \exp(\frac{r-R}{a})} \tag{1.13}$$

where R is the nucleus radius, a characterizes the skin thickness, and w describes the deviation from a spherical shape. The Glauber model assumes the nucleus consists of independent nucleons which makes it possible to derive the cross-section of nucleus-nucleus processes.

From the nucleus density distribution one can determine the (marginal) probability per unit area of the given nucleon to be located at the end of a vector $\vec{s} = (x, y)$:

$$T_A(\vec{s}) = \int \rho(x, y, z) dz. \tag{1.14}$$

A similar quantity can be constructed for nucleus B. The vector $\vec{s}$ and the impact

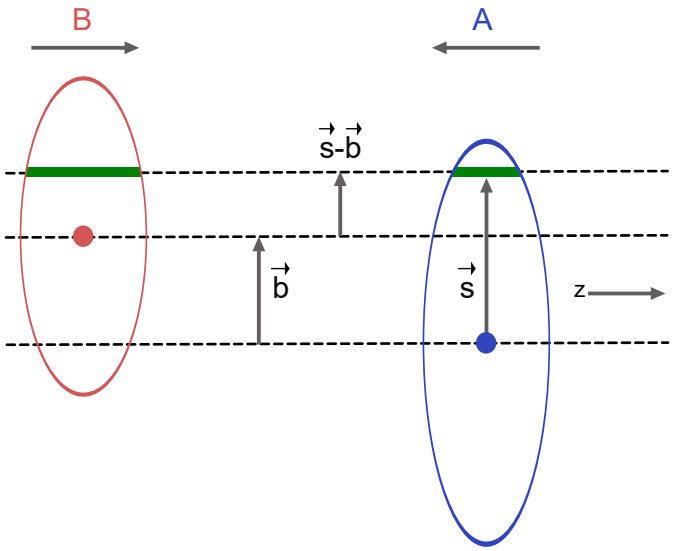

Figure 1.7: Schematic representation of a collision of nuclei A and B, the impact parameter $\vec{b}$, and the vector $\vec{s}$. The overlapping regions are depicted in green.

parameter $\vec{b}$ of the collision are depicted in Fig. 1.7. Given the impact parameter $\vec{b}$, one constructs a *thickness function*,

$$T_{AB} = \int T_A(\vec{s}) T_B(\vec{s} - \vec{b}) d^2\vec{s}, \tag{1.15}$$

which is the joint probability per unit area for the nucleon-nucleon interaction. Given the nucleon-nucleon inelastic cross-section σ^{NN}, the probability of the interaction to occur between a nucleon from A and a nucleon from B is $\sigma^{NN} T_{AB}$. Since in total there are AB possible binary combinations between nucleons from A and B, then the probability to have n interactions out of AB is defined by the binomial distribution

$$P(n, \vec{b}) = \binom{n}{AB} \left[\sigma^{NN} T_{AB}(\vec{b})\right]^n \left[1 - \sigma^{NN} T_{AB}(\vec{b})\right]^{AB-n} \tag{1.16}$$

The total probability of inelastic interaction as a function of impact parameter is simply a sum of the above equation,

$$\frac{d\sigma_{inel}^{AB}}{db^2} = p_{inel}(\vec{b}) = \sum_n P(n, \vec{b}) = 1 - \left[1 - \sigma^{NN} T_{AB}(\vec{b})\right]^{AB}, \tag{1.17}$$

and defines the total cross section,

$$\sigma_{inel}^{AB} = \int_0^\infty db 2\pi b \Big(1 - \big[1 - \sigma^{NN} T_{AB}(\vec{b}) \big]^{AB} \Big), \tag{1.18}$$

which supports the naive scaling of nucleon-nucleon cross-section to the number of nucleons in A and B. For the hard scattering process, the cross-section σ^{NN} is small, therefore one can approximate (using $\int d^2\vec{b} T_{AB}(\vec{b}) = 1$)

$$\sigma_{inel}^{AB} \approx AB\sigma^{NN}. \tag{1.19}$$

The number of collisions, defined as

$$N_{coll}(\vec{b}) = \sum_n P(n, \vec{b}) = ABT_{AB}(\vec{b})\sigma^{NN}, \tag{1.20}$$

provides an important connection between the impact parameter $\vec{b}$ and experimental observables. Another useful quantity to characterize heavy ion collision is the number of participants. For each nucleon in A, one can find total number of interactions with nucleons in B, and vise versa. In other words, let us assume nucleus A consists of 1 nucleon and calculate total number of interactions with B and multiply by A, then repeat for nucleus B and add them.

$$\begin{aligned} N_{part}(\vec{b}) = A \int d^2\vec{s} T_A(\vec{b}) \Big(1 - \big[1 - \sigma^{NN} T_B(\vec{s} - \vec{b}) \big]^B \Big) \\ + B \int d^2\vec{s} T_B(\vec{s} - \vec{b}) \Big(1 - \big[1 - \sigma^{NN} T_A(\vec{s}) \big]^A \Big) \end{aligned} \tag{1.21}$$

The above approach is called the Optical Glauber model. The Monte Carlo Glauber model is a simpler, but more computationally demanding approach, and is used in modern heavy ion event generators [8, 66]. Consider nucleons distributed according to Eq. 1.13. Two balls can interact if the distance between their centers is $\pi d^2 < \sigma^{NN}$. In the simplest model where nucleons are considered as solid "balls", this equation defines their diameter. An example collision is illustrated in Fig. 1.8. By simulating A+B collisions multiple times, one can obtain $\langle N_{coll} \rangle$ and $\langle N_{part} \rangle$. In general, results from the Optical and Monte-Carlo Glauber models are in good agreement.

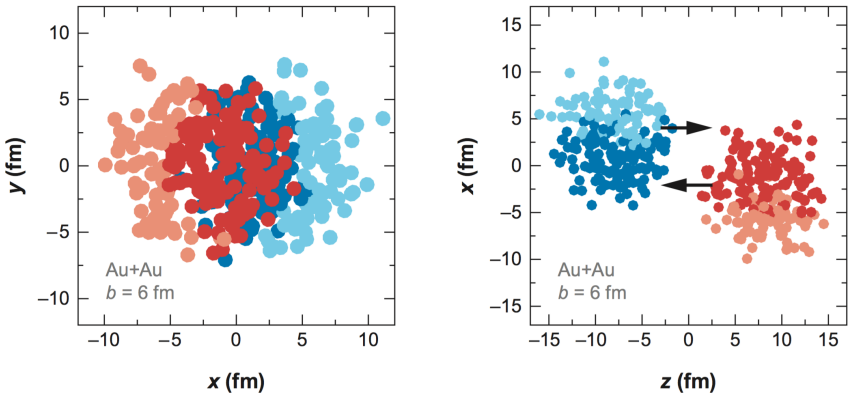

Figure 1.8: Heavy Ion collision (Au+Au) in the Monte-Carlo Glauber model, with impact parameter $b = 6$ fm. The darker circles represent the participating nucleons.[8].

Neither the impact parameter $\vec{b}$ nor the N_{coll} nor N_{part} are observed in experiment. One can notice, however, in the simulation, that large $\vec{b}$ (called peripheral) events have smaller event multiplicity and calorimeter energy, while small $\vec{b}$ (called central) events have orders of magnitude larger multiplicity. Under the assumption that the impact parameter is a monotonic function of the particle multiplicity, it is possible to build a one-to-one correspondence between the impact parameter and experimental observables.

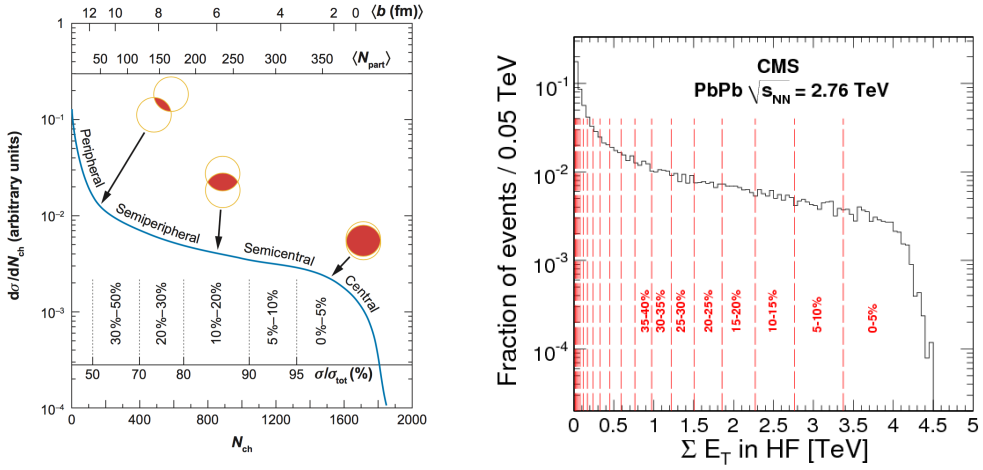

Figure 1.9: Example of the correspondence between charged particle multiplicity N_{ch} and model parameters $\vec{b}$ and N_{part} [8] (left). Centrality classes determination in CMS with forward energy calorimeters [9] (right).

As long as the total distribution of the experimental parameter (charged particle multiplicity N_{ch}, forward hadron energy E_{HF}, etc.) is observed, the centrality classes are determined as a percentile of the distribution in data and simulation. Figure 1.9 (left) shows the distribution of charged particles, the correspondence

to the model parameters $\vec{b}$ and N_{part}, and different classes of events. Experimentally, a particular class of events is often defined as a range of collision centrality, although the $\langle N_{part} \rangle$ of the class is often quoted instead, to facilitate comparisons between experiments (which may measure centrality differently). On the right, the centrality determination in CMS experiment is shown for 5 TeV data by means of percentiles of the energy in hadron calorimeter (see Sec. 2.2 for more information about CMS detector). The forward calorimeter is used for centrality determination in order to limit the bias of centrality classes by the hard process of interest.

In the PbPb collisions, two nuclei are the same and A=B=208, hence they are also called AA collisions as opposed to pp for proton-proton collisions. Averaged across impact parameter values, the mean number of collisions $\langle N_{coll} \rangle = T_{AA}\sigma^{NN}$ where A^2 was incorporated into the definition of T_{AA}. Different values of T_{AA} are tabulated for different centrality classes, e.g. in Ref. [67].

In order to qualify the difference between effects in pp and AA collision, one can compare the experimental outcome in AA collisions with the scaled pp result under the Glauber assumptions, i.e. the superposition of multiple pp collisions. The nuclear modification factor is a quantity that captures this information:

$$R_{AA} = \frac{\text{yield in AA}}{\langle N_{coll} \rangle \times \text{yield in pp}} = \frac{d^2N/dp_T d\eta}{T_{AA} d^2\sigma^{NN}/dp_T d\eta}. \tag{1.22}$$

The suppression ($R_{AA} < 1$) or the enhancement ($R_{AA} > 1$) is considered as an evidence of nuclear effects. In particular, for the observable considered in this analysis, it is the consequence of the parton energy loss which is discussed in Sec. 1.2.3.

1.2.2 QCD factorization and nuclear modification factor

Because of asymptotic freedom, the QCD coupling $\alpha_s(Q)$ decreases with high energy, which allows perturbative computations of hard processes. Although the direct computation of hadron-hadron process involves an infinite number of Feynman diagrams, an accurate approximation can be done which reduces computation

of hadron-hadron cross-sections to the parton-parton cross-sections:

$$\sigma_{AB\to h} = \sum_{a,b,c} \int dx_1 dx_2 dz f_{a/A}(x_1) f_{b/B}(x_2) \sigma_{ab\to c}(x_1, x_2) \mathcal{D}_{c\to h}(z), \tag{1.23}$$

where the perturbative parton-parton cross-section $\sigma_{ab\to c}(x_1, x_2)$ is surrounded by two non-perturbative, but universal terms:

- parton distribution functions (PDF) $f_{a/A}(x_1)$ describe the probability to find a parton of flavor a with fraction x_1 of momentum of the initial hadron A. This function can be found by probing the partonic structure of the nucleon with electrons. In the nucleus, the PDFs are modified, which leads to the notion of the nuclear PDF (nPDF).
- fragmentation functions (FF) $\mathcal{D}_{c\to h}(z)$ describe the probability for a parton c to fragment into a hadron h with a fraction z of parton momentum. These functions can be obtained in e^+e^- collisions.

The formula 1.23 is known as a QCD factorization theorem [68]. In the case when the final state is a jet one simply sets $\mathcal{D}_{c\to h}(z) = \delta(1-z)$.

The assumption under this theorem is that the characteristic timescale of the QCD hard process is much smaller than that among partons belonging the same proton or of their evolution into the final hadrons. Effectively, one can consider the partons to be "frozen" during the hard scattering timescale, and the nucleus to consist of free partons. From the perspective of hard process, nucleus A can be considered as a superposition of A independent nucleons

$$f_{a/A}(x_1) = A f_{a/N}(x_1), \tag{1.24}$$

and therefore the hard inclusive cross-section in AA collisions is simply $\sigma_{AA}^{hard} = A^2 \sigma_{NN}^{hard}$, or in more general form (averaged across centrality dependence of a particular hard process):

$$\sigma_{AA}^{hard} = \langle N_{coll} \rangle \sigma_{NN}^{hard}. \tag{1.25}$$

The hard process should then scale with the mean number of binary collisions.

This justifies the definition or nuclear modification factor R_{AA} (formula 1.22) that measures the deviation from the binary collisions scaling.

1.2.3 Parton energy loss. Light vs Heavy Quarks

Depending on the kinematics, the parton can lose energy by two mechanisms:

- collisional energy loss, or elastic scatterings with the medium constituents, dominates at low particle momentum
- radiative energy loss, or inelastic scatterings with the medium in the form of bremsstrahlung radiation, dominates at higher momentum.

Energy loss is well-studied in the QED plasma [69]. The main difference between QED and QCD comes from the non-Abelian nature of QCD: the fact that gluons can interact among themselves. The coupling of hard scattered quarks and gluons to the quark-gluon plasma is different and mainly defined by the vertex couplings which are caused by the Casimir factors of the SU(3) gauge group: for q–qg vertex $C_F = 4/3$, for g–gg $C_A = 3$, and for g–qq $T_F = 1/2$. In the asymptotic limit of the soft radiation off the original parton, the number of gluons radiated by the gluon is $C_A/C_F = 9/4$ times larger than radiated by quark. This is also the reason why gluon jets have larger multiplicity than the quark jets.

The bremsstrahlung radiation is suppressed in the cone with angle θ_0 around the quark by the factor $\left(1 + \frac{\theta_0^2}{\theta^2}\right)^{-2}$. This phenomenon is called the "dead cone" effect [70], and dead cone angle $\theta_0 = M/E$. Because of its mass dependence, the dead cone angle is negligible for light quarks, but is significant for the heavy c and b quarks.

For studies of parton energy loss models in a realistic QGP (which is encountered in heavy-ion collisions) one has to deal with the following complications, among others: the final state is not a parton, but rather a collection of hadrons produced by the non-perturbative fragmentation process, that partons can be produced at any point in the QGP, that the QGP is non-uniform and time-dependent, and also that its finite size leads to fluctuations. There are different models with various

approaches to treat these problems, as an example the computations from the AMY model are presented on Fig. 1.10[10]. One can see that for low p_{T} collisional and radiative energy loss mechanisms are comparable, while for higher p_{T} the radiative energy loss dominates.

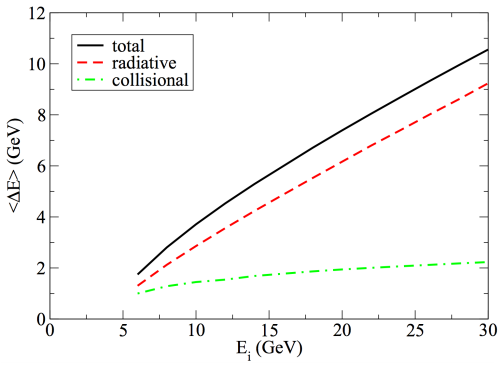

Figure 1.10: The mean energy loss of a quark jet with initial energy E_i passing through the nuclear medium created in central collisions (b = 2.4 fm) at RHIC. The jet starts from the center of the medium and propagates in plane [10].

As a result of the medium-induced energy loss, the following consequences are observed:

- a suppression of high-p_{T} hadrons and jets, also known as the *jet quenching* phenomenon [19],
- unbalanced back-to-back high-p_{T} di-hadron and dijet correlations [71],
- modified jet fragmentation [72],
- flavor-dependent energy loss implies more suppression for gluons and light quarks than for heavy quarks $\Delta E(g) > \Delta E(q) > \Delta E(c) > \Delta E(b)$ which should result in e.g. flavor-dependent jet quenching results [21].

For more information about the parton energy loss as well as the models of jet quenching see Ref. [68].

1.2.4 Heavy Quark production mechanisms at the LHC

Although the quark flavor defines the rate of the energy loss, not all the heavy quarks are *primary*, i.e. produced directly in the hard scattering. The b quark production at the leading-log order can be split into 3 categories [73]:

Flavor creation (Fig. 1.11a) corresponds to the production of $b\bar{b}$ pair by means of gluon fusion and $q\bar{q}$ annihilation. The typical topology for this configuration is back-to-back pair of b-quarks. Although this process is leading-order, it is not dominant for inclusive b-jet production at LHC energies.

Flavor excitation (Fig. 1.11b) is an additional source of b-quarks coming from hard scattering of initial state (sea) b-quark by a gluon (or a light quark) to the final state. As the other quark does not participate in the hard scattering, except for recoil, it should typically appear in the forward rapidity region with rather low p_{T}.

Gluon splitting (Fig. 1.11c) is a process where b quarks are not produced directly in the hard process. Rather $b\bar{b}$ pairs are produced in the parton shower or the fragmentation process of outgoing light parton. Typically, two b-quarks are separated by a small angle in the final state.

This analysis uses the Pythia 6 event generator which is described in Sec. 2.3.2. Because Pythia is a leading order generator, only the flavor creation process can be modeled with matrix elements, while flavor excitation and gluon splitting are simulated with initial and final state radiation, respectively.

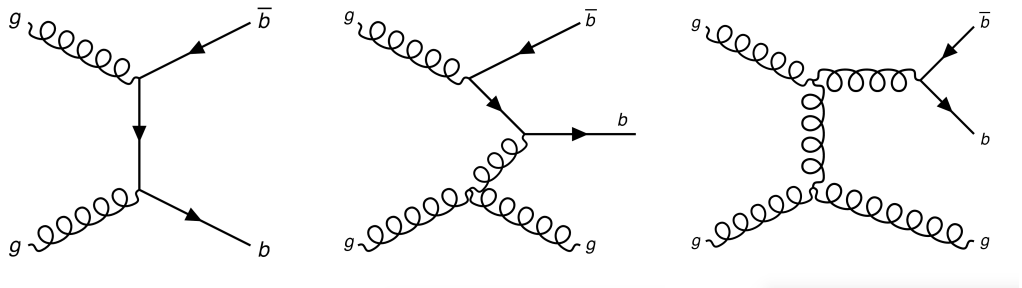

(a) Flavor Creation (b) Flavor Excitation (c) Gluon Splitting

Figure 1.11: B-jet production mechanisms at next-to-leading order in pQCD.

Figure 1.12 shows the comparison of the b-jet cross-section in CMS pp data and in Pythia, where the latter is separated into the three production mechanisms. A tight b-tagging requirement is applied to get rid of light jet contamination (b-tagging is discussed in Sec. 3.3). One can see that in general Pythia does a good job predicting the b jet cross-section, and it is not flavor creation that has biggest contribution. Despite that, flavor creation is the most important process for the

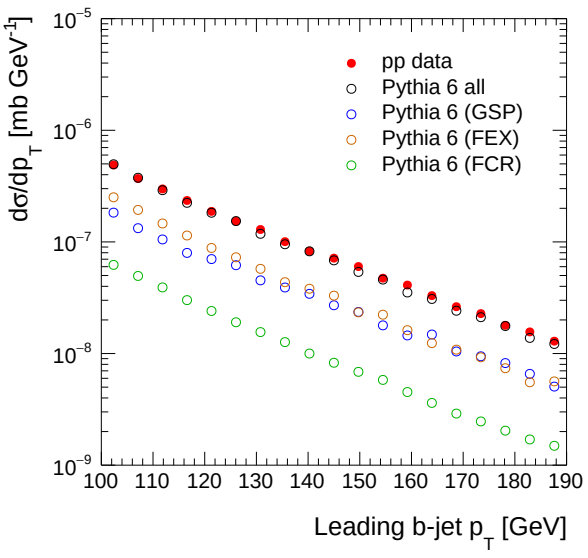

Figure 1.12: Leading b-jet spectrum in CMS pp data and predicted by Pythia in components: flavor creation (FCR), flavor excitation (FEX) and gluon splitting (GSP).

analysis described in Chapter 4, as it produces a well correlated pairs of primary b-jets. In the flavor excitation, b-quark pairs become decorrelated after the interaction of one of them with the light parton. This process is in fact mismodeled by Pythia and one has to apply correct reweighting factors to reproduce the correct contributions of different processes; this procedure is described in Sec.2.3.6. The gluon splitting mechanism produces non-primary b-jets and it is preferred to minimize the contribution of this process.

1.2.5 First results on jet quenching

The jet quenching phenomenon is widely believed to be the signature of parton energy loss in hot nuclear matter and it was first predicted by Bjorken [74]. Historically, the first observation of jet quenching was made at Relativistic Heavy Ion Collider (RHIC)[11]. Figure 1.13 shows a di-hadron correlation in the azimuthal plane in p+p, d+Au and Au+Au collisions. This distribution is obtained by measuring the azimuthal separation between the hadron with large transverse momentum (trigger particle) and associated particles in the event. The near-side peak (small $\Delta\phi$) is formed from the particles coming from the same jet as a trigger particle. The double-peak structure can be understood in term of dijet

events. In Au+Au collisions however, the away-side peak disappears which is an experimental observation of jet quenching.

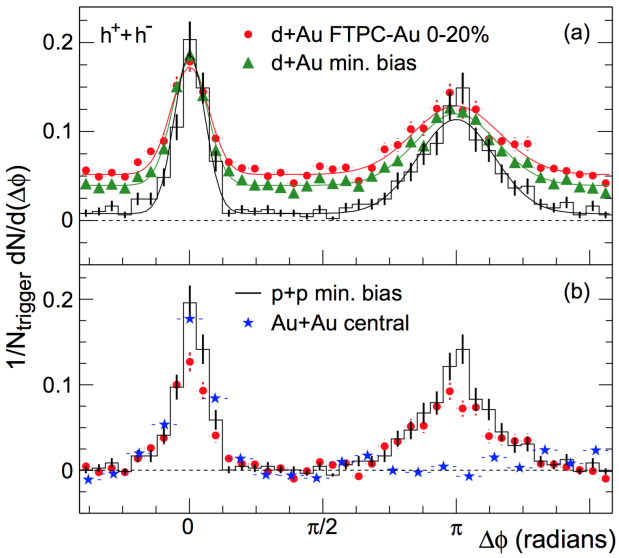

Figure 1.13: Two-particle azimuthal correlations for pp, d+Au and Au+Au collisions in $\sqrt{s} = 200$ GeV collisions from STAR experiment at RHIC [11].

Jet quenching leads to the suppression of high-p_{T} particles production. Figure 1.14(left) shows the suppression of high-pt π^0 particles from the PHENIX experiment [12]. Photons and weak bosons $\mathrm{W}^{\pm}$ and Z do not participate in strong interaction, and therefore the medium should be transparent to them. Figure 1.14(right) is a compilation of results from the CMS experiment of suppression of different particles species in PbPb collisions at $\sqrt{s} = 2.76$ TeV. Indeed, charged hadrons show a large suppression ($0.1 < R_{AA} < 0.5$) while there is no suppression for γ, W, and Z bosons.

1.2.6 Jet definition

Jets are experimental signature of hard scattered partons, and consist of a collimated spray of hadrons. They were first observed at SLAC in 1975 [75] as an obvious structure in event displays. Since that time jet reconstruction algorithms have been developed and in the widespread use nowadays. These algorithms have to satisfy a number of important properties which are described in this section.

The basic properties and challenges of jet reconstruction can be inferred from the

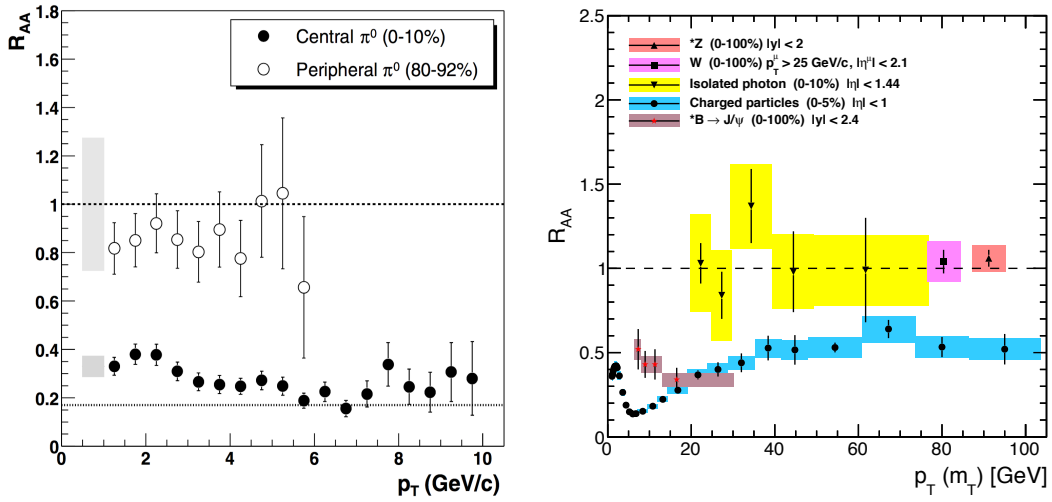

Figure 1.14: Left: Nuclear modification factor R_{AA} for π^0 in central and peripheral Au+Au collisions at $\sqrt{s_{NN}} = 200$ GeV from the PHENIX experiment at RHIC [12]; Right: Nuclear modification factor for different particle species in Pb+Pb collisions at $\sqrt{s_{NN}} = 2.76$ TeV from the CMS experiment at the LHC [13, 14, 15, 16, 17]

splitting function for a quark to radiate a gluon [76]:

$$dP_{q\to qg} = C_F \frac{\alpha_s}{2\pi} \frac{d\theta^2}{\theta^2} \frac{1+z^2}{1-z} dz, \tag{1.26}$$

where z is the ratio of initial quark energy to the quark energy after the splitting, while $1-z$ is the fraction of initial energy carried by the radiated gluon, α_s is the QCD coupling, θ is the angle between the quark and radiated gluon, and $C_F = 4/3$ is the color factor. Three observations can be immediately made with this formula:

- Asymptotic freedom $\alpha_s(Q) \to 0$ for large Q suppresses radiation for hard particles, therefore the harder the initial parton energy the more collimated jet will be,
- there is a high (divergent!) probability of low-energy (infra-red) emission with $z \to 1$,
- there is a high (divergent!) probability of collinear emission with small θ.

It turns out that these divergences cancel out nicely with higher order virtual corrections giving the same infinities but with the opposite sign. However, for the

experimentalist this gives two important requirements the jet reconstruction must be insensitive to (see Fig. 1.15):

- addition of low-pt particles (infra-red safety)
- collinear splitting a hard particle onto two (collinear safety)

and in general they are referred as IRC (infra-red and collinear) safety, and is a basic requirement for the jet algorithm. If the jet reconstruction is not IRC safe, then the divergent contributions do not cancel and perturbative predictions do not make sense. Other desirable attributes of a jet algorithm are minimal sensitivity to hadronization, the underlying event and pile-up, and fast implementation.

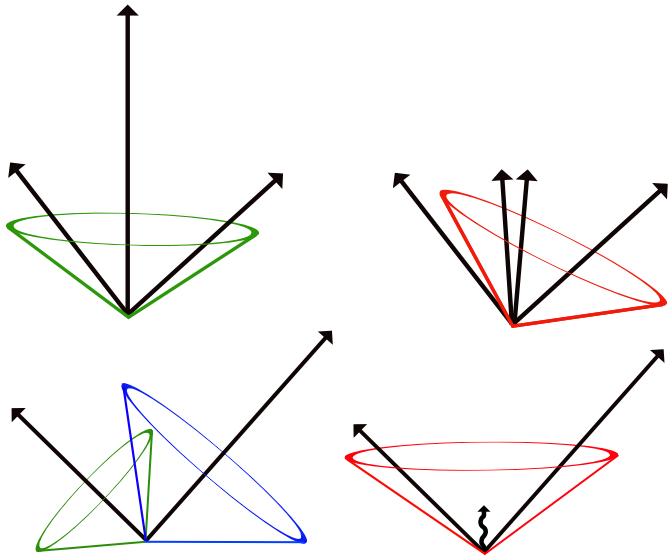

Figure 1.15: Top: Collinear unsafe jet algorithm produces different cones without (left) and with (right) collinear splitting of a particle. Bottom: Infrared unsafe jet algorithm produces different cones without (left) and with (right) radiation of a soft particle.

Imagining a jet, one immediately thinks about a cone of collimated particles. As a result, the first algorithms were cone algorithms. A cone can be characterized by the axis and the radius R in $\eta - \phi$ space: $R = \sqrt{\Delta\eta^2 + \Delta\phi^2}$. An example is the iterative cone algorithm [27], which proceeds as follows:

- take a highest p_{T} particle (seed)
- sum up the 4-momenta of particles in the vicinity R around jet axis
- if the new axis coincides with original - call it a jet and remove particles from the event, otherwise repeat with the new axis

- repeat until no seeds above threshold are left

This algorithm is not IRC safe. If the highest p_{T} particle splits into two, then a different cone will be found by the algoritm (Fig. 1.15, top). Imagine we have two stable cones around two particles separated by $R < \Delta R < 2R$ (Fig. 1.15, bottom). If we add a soft particle in-between, then the two cones are not stable cones anymore, and a new cone around the soft particle arises and is a stable cone. IRC safety is a very important issue: it makes little sense that the high-p_{T} jets are modified by adding a soft particle in-between. Although efforts were made to improve the algorithm (e.g. SIScone [77]), the current state-of-the-art is not a cone algorithm.

Sequential clustering algorithms are based on a different approach: they combine particles based on their transverse momenta and try to reverse-engineer the QCD branching process. Because of this, they are IRC safe by construction and are preferred by theorists. They were not preferred by experimentalists because of the long running time, until the FastJet [78] implementation, which offered a dramatic timing improvement. Sequential clustering is based on the two distance measures:

- distance between two particles $d_{ij} = min(k_{T,i}^{2p}, k_{T,j}^{2p})\frac{R_{ij}}{R}$
- momentum-space distance between the particle and the beam axis $d_{iB} = k_{T,i}^{2p}$

where $R_{ij}^2 = \Delta\eta_{ij}^2 + \Delta\phi_{ij}^2$, and the algorithm is defined as follows:

- compute all d_{ij} and d_{iB} and find the smallest
- if d_{ij} is the smallest - combine particles i and j and recompute distances
- if d_{iB} is the smallest - then call the particle i a jet and remove from the event
- repeat until all particles are clustered

The constant R scales the distance between particles d_{ij} so that jets are at least separated by R. The p parameter defines the algorithm behavior and there are basically three distinct behaviors with respect to the value of p

- $p = 1$: *k_T algorithm*[79]. This algorithm clusters soft particles first which results in a fluctuating jet shape and is very susceptible to the UE fluctuations

- $p = 0$: *Cambridge/Aachen algorithm*[80]. The distance measure is momentum independent and clustering is based on the spatial separation only. k_T and C/A algorithms do a good job at resolving jet substructure.

- $p = -1$: *anti-k_T algorithm*[18]. It clusters hard particles first and resulting cones are circular in $\eta - \phi$ space. Also this algorithm is the least sensible to underlying event and pileup effects.

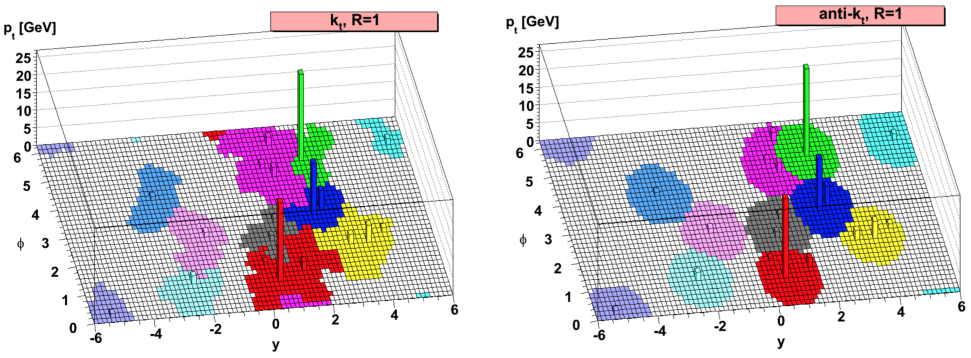

Figure 1.16: Jet reconstruction with k_T (left) and anti-k_T (right) algorithms on the same data and with the same radius parameter R [18].

The anti-k_T algorithm is widely used in jet reconstruction because of many reasons: it is IRC safe, the shape of the jet is defined by hard particles, rather than soft particles (which results in a conical jet when a hard particle is surrounded by only soft particles) and because it is reasonably fast, using the FastJet implementation.

1.2.7 Jet quenching with jets

Using detectors available at the LHC, a measurement of the parton kinematics can be made by using fully reconstructed jets. The nuclear modification factors R_{AA} of jets were measured at ALICE [81], ATLAS [82] and CMS [19]. Figure 1.17 shows jet R_{AA} as a function of number of participants N_{part}. The increasing suppression is observed with larger N_{part} showing that this effect is centrality dependent.

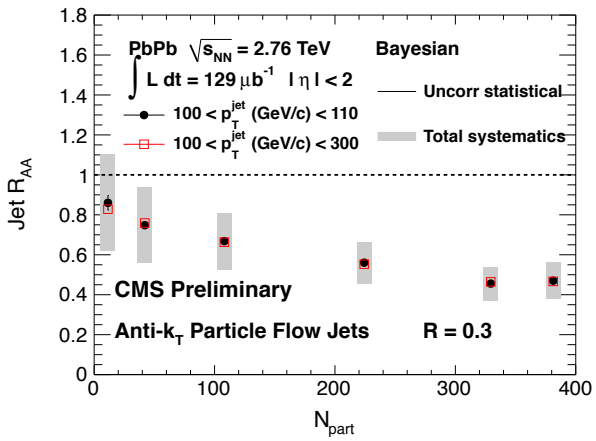

Figure 1.17: Nuclear modification factor R_{AA} of jets as a function of number of participants N_{part} from CMS at 2.76 TeV [19].

The first observable to probe jet quenching measured at the LHC is transverse momentum balance of dijet pairs in PbPb collisions [83, 71]. Quenching imparts a net imbalance to dijet pairs, which exceeds that produced by QCD radiation and detector resolution effects, as measured from pp collisions. The cause of this anomalous imbalance is that the quenching varies jet-by-jet, due to variation of both the path-length through the quark-gluon plasma, as well as via fluctuation of the parton energy loss process itself [84].

In this measurement, the leading (highest p_{T}) and subleading (second-highest p_{T}) jets are selected as a dijet pair, and their transverse momentum balance is measured. By selecting on the leading jet, we preferentially pick out jets which have suffered little quenching, whereas the subleading recoil jets tend to sample a larger path-length, and therefore suffer a larger quenching. Quenched jets tend to deposit energy at very low p_{T} and large angle such that the quenched energy is no longer associated with the reconstructed jet [71, 85]. In this way, the dijet imbalance becomes a particularly sensitive probe of the interaction of hard scattered partons with the quark-gluon plasma.

Figure 1.18 presents the measurement of dijet asymmetry $\frac{p_{T,1}-p_{T,2}}{p_{T,1}+p_{T,2}}$ for different centrality classes in PbPb collisions with CMS at $\sqrt{s_{NN}} = 2.76$ TeV. In the top left panel the result of the peripheral PbPb collisions is compared to pp collisions and no significant difference is observed. The asymmetry from the simulation where there is no jet quenching also agrees with the peripheral PbPb data. In the

central bin the asymmetry distribution is shifted towards larger asymmetry values indicating the presence of jet quenching.

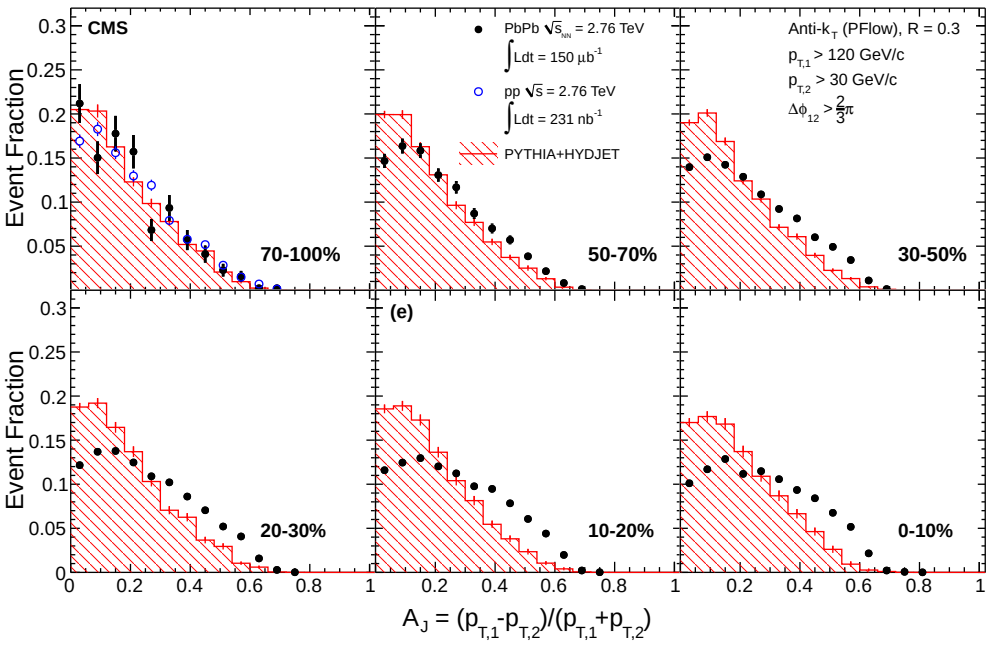

Figure 1.18: Transverse momentum asymmetry distribution of jets in different centrality bins from CMS at $\sqrt{s_{NN}} = 2.76$ TeV [20]. The most peripheral bin also contains measurement of momentum asymmetry in pp collisions for comparison.

The dependence of jet quenching on parton mass and flavor remains poorly known. As radiative energy loss is thought to be the dominant mechanism, gluons are expected to lose more energy than quarks, due to their larger Casimir color factor. On the other hand, radiation from massive quarks is expected to be suppressed in the direction of propagation, the so-called dead-cone effect, at least for energies not much larger than the quark mass. The suppression of the D meson measured by ALICE [21] is indeed different from the suppression of b hadrons measured via non-prompt J/ψ by CMS [17] as shown on Fig. 1.19 (left). The data should be interpreted with caution as a nuclear modification factor is sensitive to effects unrelated to parton energy loss, like kinematic effects of the $B \to J/\psi$ decay or the difference in the fragmentation of b and c quarks.

Jets initiated by b quarks are an excellent observable to test expectations of flavor dependent energy loss, given that they are readily identifiable via b-tagging methods. The first steps in this direction were already taken via the measurement of b-jet spectra and nuclear modification factors in pPb [86] and PbPb [22] (Fig. 1.19).

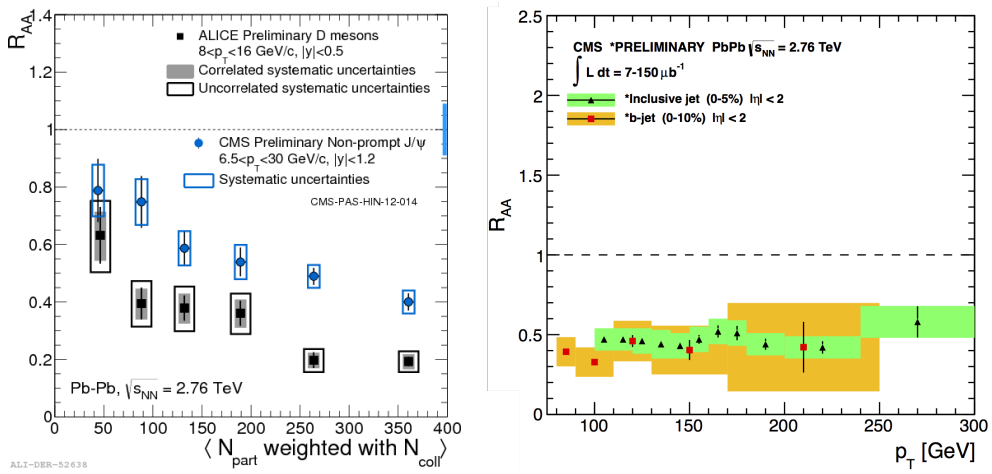

Figure 1.19: Flavor dependent studies of the nuclear modification factor R_{AA}. The suppression is larger for D mesons [21] than for for non-prompt J/ψ [17] (left), no difference is observed for suppression of inclusive jets vs b-jets in the most central collisions (right) [19, 22].

While no strong dependence of quenching on parton species was evident, the uncertainties on these spectra measurements are fairly sizable. By contrast, dijet asymmetries offer reduced sensitivities to experimental effects such as the jet energy scale. In addition, they largely remove an irreducible background from the final state splitting of gluons into b-quark pairs, as we briefly explain in what follows.

1.2.8 The motivation

As it was discussed in Sec. 1.2.5, the jet quenching phenomenon was discovered at RHIC and studied extensively at LHC. Flavor dependent studies of jet quenching, on the other hand, are not very conclusive yet. The nuclear modification factor of b-jets presented on Fig. 1.19 is a subject to large systematic uncertainties. One of the main reasons is the low b-tagging efficiency: most b-jets are very hard to find, especially in central collisions (see Sec. 3.3 for more information about tagging). In spectra measurements (which is a basis for the R_{AA} calculation) one has to correct for the efficiency effect, hence increasing the uncertainty. On the other hand, the dijet imbalance (Fig. 1.18) uses ratio of jet momenta and hence only the *relative* inefficiency has to be corrected for.

Another motivation to use back-to-back pair of b-jets is the contribution of the NLO production modes which may give non-primary b-jets. As illustrated in

Fig. 1.20 (left), the overall contribution of the gluon splitting process to the inclusive b-jet spectrum is about 40%. However, from the azimuthal angle distribution $\Delta\phi$ on Fig. 1.20 (right) one can see that back-to-back pairs of b-jets tend to be produced directly in the primary hard scattering.

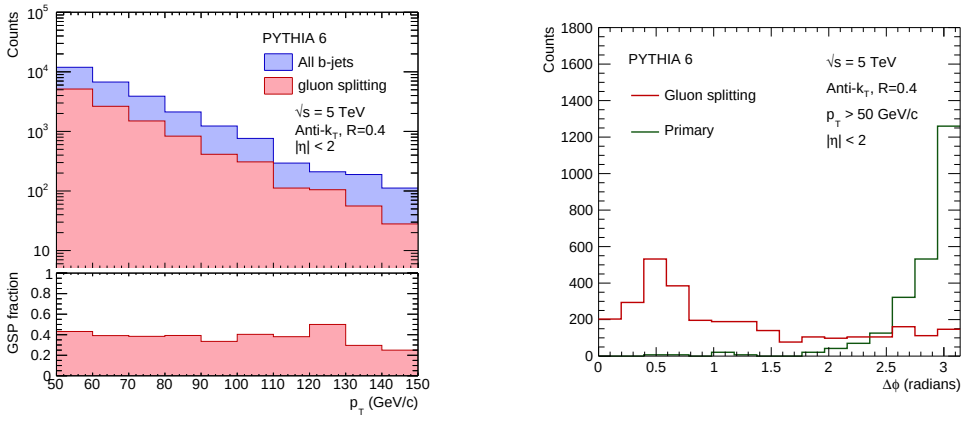

Figure 1.20: An illustration of b-jet production modes in PYTHIA6. Left: The inclusive b-jet p_{T} distribution, and the contribution from gluon splitting. Right: $\Delta\phi$ distribution between b-jet pairs, for primary and gluon splitting b-jets.

The difference or the similarity between inclusive and b-tagged dijet imbalances can provide information about the flavor dependence of the energy loss. This measurement was performed with CMS detector which is described in Chapter 2. The reconstruction of objects used in the analysis (tracks, jets and b-tagging discriminator) is covered in Chapter 3. Finally, the data taking process and the analysis of transverse momentum imbalance of inclusive and b-jets are described in Chapter 4.

Experimental setup and simulation

2.1 Large Hadron Collider

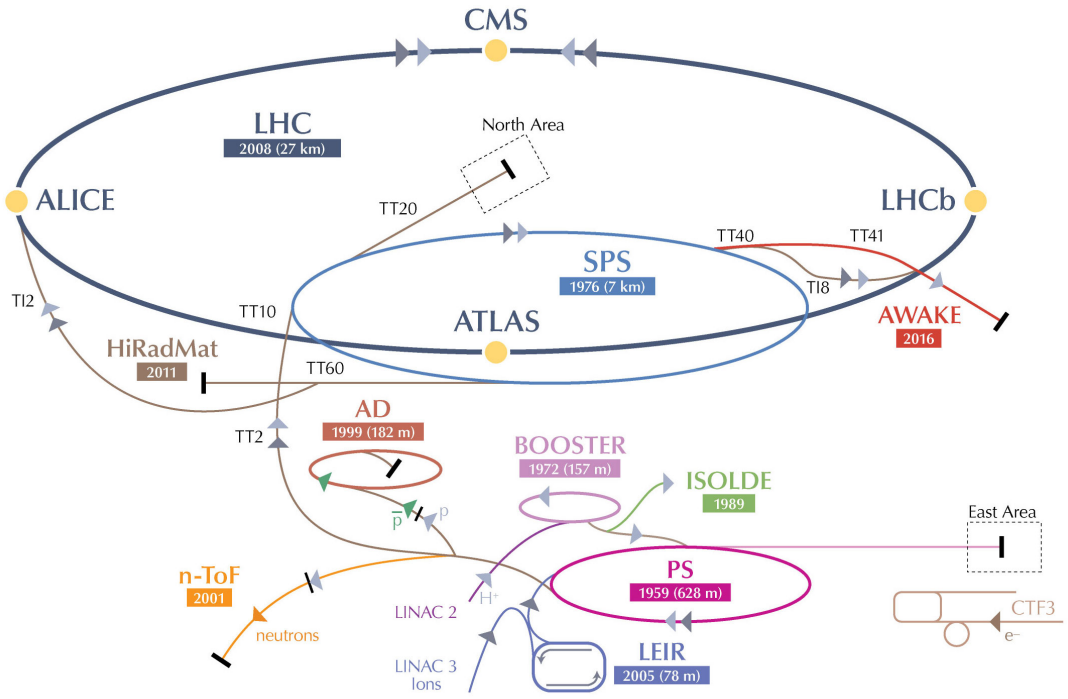

Figure 2.1: The Large Hadron Collider and associated accelerators [23].

The Large Hadron Collider (LHC) is the most powerful particle accelerator in the world. The LHC consists of a 27-kilometer ring of superconducting electromagnets containing two beams of accelerating particles in an ultrahigh vacuum. The beams collide at 4 main experiments: CMS, ATLAS, ALICE and LHCb. The LHC accelerated protons at a center-of-mass energy of up to $\sqrt{s} = 8$ TeV in Run 1 (2009 – 2013) and $\sqrt{s} = 13$ TeV in Run 2 (2015 – present) and Pb nuclei at $\sqrt{s} = 2.76$ TeV per nucleon in Run 1 and $\sqrt{s} = 5.02$ TeV per nucleon in Run 2.

The LHC relies on other accelerators. Protons exit the LINAC 2 linear accelerator at an energy of 50 MeV and enter the Proton Synchrotron Booster where they are accelerated to 1.4 GeV followed by the Proton Synchrotron (PS) accelerator where they acquire 25 GeV of energy. The last step before entering the LHC is the Super Proton Synchrotron (SPS) in which particles are accelerated up to 450 GeV. At the LHC they are accelerated to their maximum energy of 6.5 TeV which corresponds to 13 TeV center-of-mass energy at the collision.

Heavy ions are created from vaporized lead Pb-208 and accelerated first with the LINAC 3 linear accelerator, followed by the Low Energy Ion Ring (LEIR) which splits the long pulses of the lead ions into short bunches containing ∼220 million lead ions and accelerates bunches of lead ions up to 72 MeV suitable for the injection into the PS [87]. Then ions follow the same route as the protons to their collisions at LHC at 5 TeV per nucleon center-of-mass energy.

During the 2015 heavy ions run, the LHC delivered 600 μb^{-1} of integrated luminosity, out of which 550 μb^{-1} has been recorded by the CMS experiment (Fig. 2.2, right). Out of the delivered data 404 μb^{-1} passed tight quality requirements and is used in this analysis. As part of the heavy ion run, proton beams were also collided at the same center of mass energy as heavy ions, as a reference. The LHC delivered 29.52 pb^{-1} of integrated luminosity during the pp reference run and CMS recorded 27.87 pb^{-1}, out of which 25.8 pb^{-1} is used (Fig. 2.2, left).

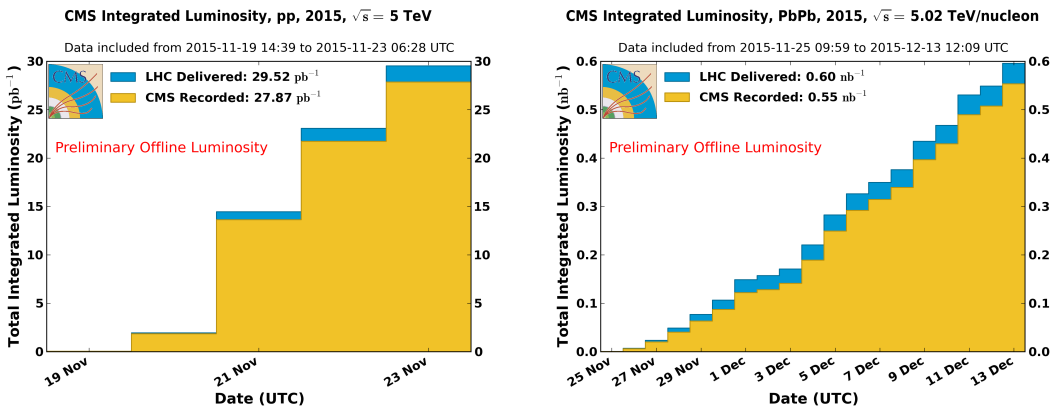

Figure 2.2: Integrated luminosity delivered by the LHC and recorded by CMS during the 2015 pp reference (left) and heavy ion (right) runs [24].

2.2 CMS detector

The CMS detector (Fig. 2.3) is a general-purpose detector located at 70 m underground near Cessy (France). It is suited for a wide range of phenomena in particle physics: properties of the Higgs boson, the search for physics beyond the Standard Model, such as supersymmetric particles or signs of extra dimensions, as well as the study of the quark-gluon plasma created in heavy ion collisions.

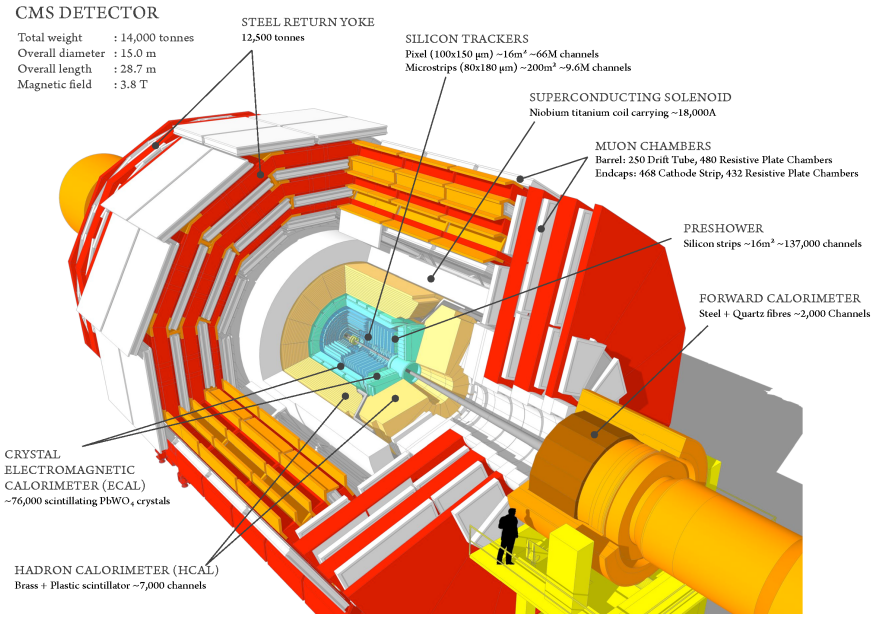

Figure 2.3: The CMS detector [25].

The main strengths of CMS detector are:

- good muon identification and momentum resolution in a wide range of energies
- good charged particle reconstruction efficiency and momentum resolution
- the ability to reconstruct secondary vertices from b-decays due the the inner tracking system close to the interaction point
- good electromagnetic energy resolution
- hermetic coverage of detectors out to large η to measure all particles including the neutrino (via its missing energy)

For more information about the detector see Ref. [27].

The core of the CMS detector is a 13 meters long, 6 meters in diameter 4 Tesla superconducting magnet. It is surrounded by an iron structure which guides the return magnetic field and is layered with muon detectors. All other detectors are located inside the magnet.

2.2.1 Tracking system

The CMS tracker is the first detector particles traverse after the collision. The purpose of the tracker is to detect the position of the particles with the minimum impact on the particles' velocity. The amount of material inside the active volume of the tracker is 0.4 X_0 at midrapidity and 1 X_0 at $\eta \sim 1.6$ [88].

In order to avoid the shallow incident angles between particles and detector surfaces, the detector is split by two parts: barrel layers which are parallel to the beam line and cover approximately ± 1 unit of pseudorapidity, and endcaps which are perpendicular to the beam line.

The detector closest to the interaction point is the pixel detector, which consists of 3 layers in the barrel and 2 layers in the endcap. Each pixel has dimensions of 100x150 μm with 66 million pixels total, which achieves a spatial resolution of about 10 μm in $r - \phi$ and 20 μm in the z dimension. The reason for such high granularity of the pixel detector is twofold. First of all, the density of particle flux is the highest near the interaction point. Secondly, the pixel detectors play a crucial role in the early stages of the tracking and in the vertexing which is vital to this analysis in particular. The occupancy of the pixel detector is $\sim 0.01\%$ in pp collisions and $\sim 1\%$ in PbPb collisions.

Beyond the pixel layers, the tracker consists of microstrip layers. In the barrel, the inner barrel (TIB) and outer barrel (TOB) layers have a minimum size of 80 μm $\times$ 10 cm and 180 μm $\times$ 25 cm respectively. The increased size of strips is possible because of lower flux density of particles. The first two strip layers of the inner and outer barrel are made of "stereo" modules, i.e. two strips on top of each other with the small angle of 100 mrad between them. This allows for the 23(52)

μm resolution in the z coordinate of the particle as opposed to 10(25) cm of the single strip layers.

The tracker endcap (TEC) consists of 9 disks of stereo and mono layers arranged in disks centered on the beam line. The transition space in between barrel and endcap layers is filled with the inner disks (TID).

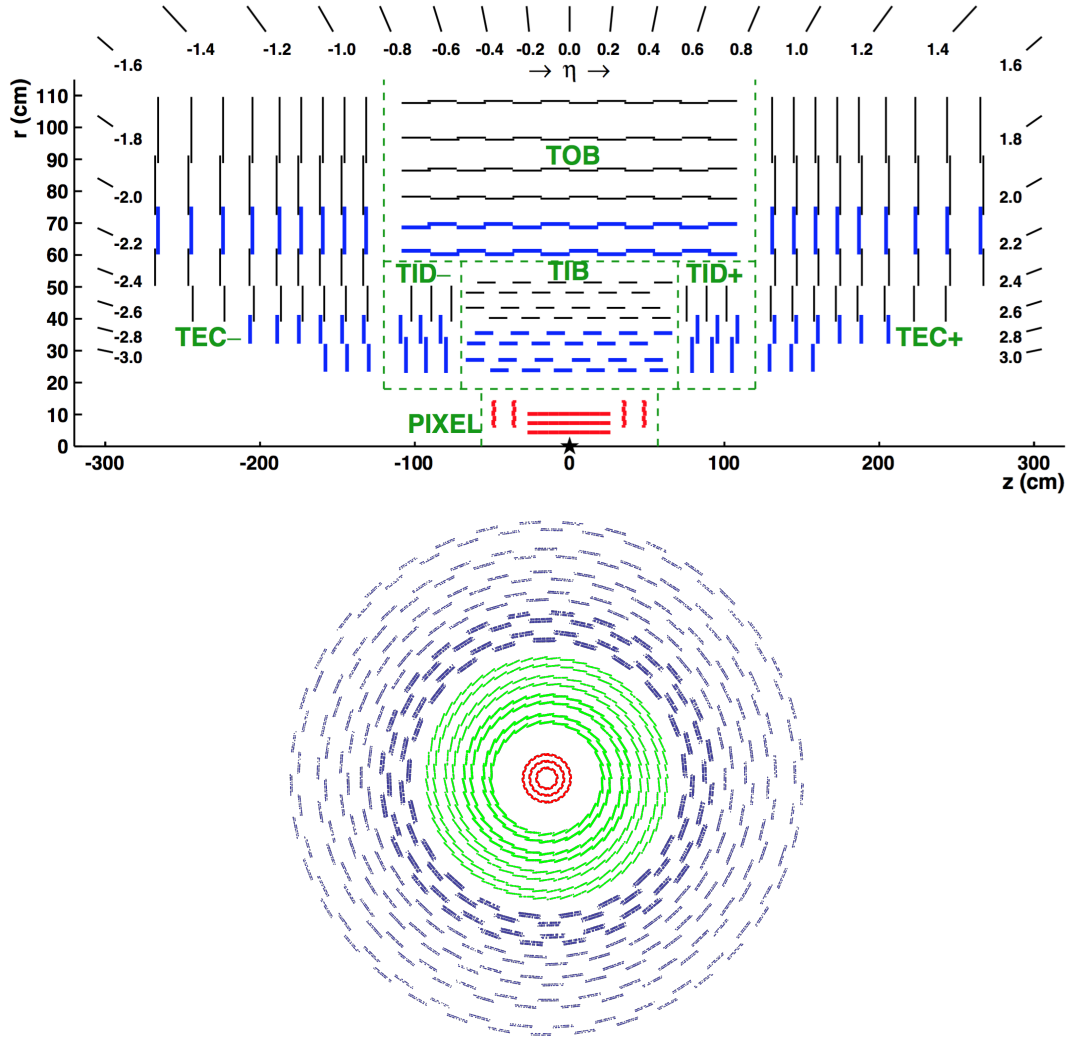

Figure 2.4: Tracker layout in the longitudinal view (top) [26], the dashed lines enclose the barrel layers; the transverse view of the barrel layers (bottom).

Figure 2.4 (top) shows a schematic cross-section of half of the tracker. Blue lines represent stereo layers, black lines represent single layers of strips, pixel layers are shown in red and the star represents an approximate interaction point. Horizontal layers form the central barrel while vertical lines form the endcaps. In Figure 2.4 (bottom) the result of the simulation is shown. Multiple tracks were propagated through the tracker barrel and their intersection points with the detector modules

(hits) are shown: pixel layers (red), TIB strip layers (green) and TOB strip layers (blue) are shown only. Layers of the inner barrel seem doubled because they are overlapped in the z axis to prevent the gaps between modules.

The performance of the CMS tracker is presented in Fig. 2.5, where the transverse momentum and impact parameter resolutions for muons are shown. The resolution of transverse momentum p_{T} measurement is around 1% at midrapidity while the transverse impact parameter d_0 can be measured with a precision of $\sim 10\ \mu m$, which is crucial for the b-jet identification in this analysis.

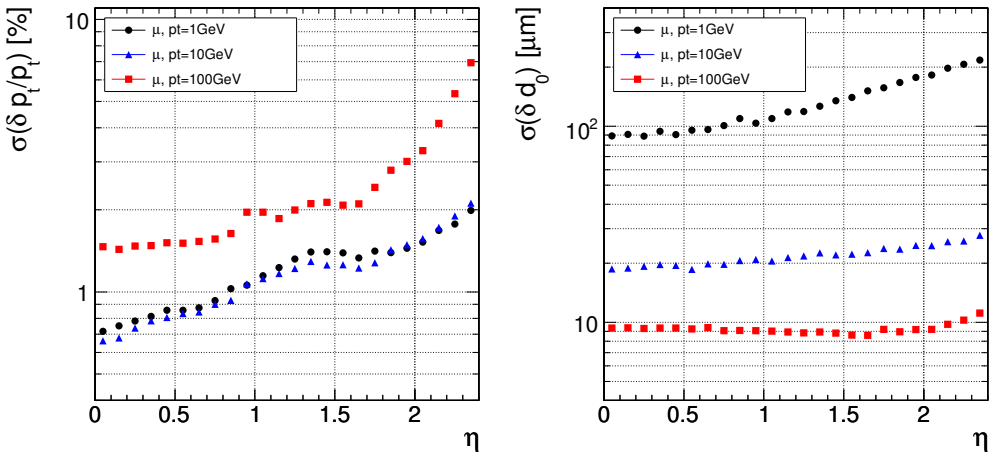

Figure 2.5: Resolution of charged particles in CMS: transverse momentum p_{T} (left) and transverse impact parameter d_0 (right) [27].

2.2.2 Electromagnetic calorimeter

The Electromagnetic Calorimeter (ECAL) is designed to absorb the energy of photons and electrons. The ECAL of CMS is a homogeneous calorimeter made of 61200 lead tungstate ($PbWO_4$) crystals in the central barrel and 7324 crystals in each of the two endcaps [89]. Such crystals were chosen for their short radiation length ($X_0 = 0.89$ cm) and fast response. In the barrel, the crystals have a front face cross-section of 22×22 mm^2 corresponding to 0.0174 in $\Delta\phi$ and $\Delta\eta$ and a length of 230 mm, corresponding to 25.8 units of radiation length X_0. In the endcap the crystals have a front face cross section of 28.6×28.6 mm^2 and a length of 220 mm which corresponds to 24.7 X_0.

The performance of the ECAL is one of the strengths of CMS, providing an elec-

tron energy measurement with resolution of only $\sigma/E = 2.8\%/\sqrt{E}$ in the barrel region [90].

2.2.3 Hadron calorimeter

As opposed to the homogeneous ECAL, the CMS hadron calorimeter (HCAL) is a sampling calorimeter, i.e. it is made of repeating layers of brass absorber and plastic scintillating plates with embedded optical fibers that collect the emitted light and transfer it to the read-out system [91, 92]. The choice of the technology and materials is dictated by the compact size of CMS and the requirement to locate the calorimeter inside the coil.

The barrel part of the HCAL (HB) covers a pseudorapidity of $-1.4 < \eta < 1.4$ and has segmentation $\Delta\eta \times \Delta\phi = 0.087 \times 0.087$ with 2304 towers total. The energy resolution of the HB is $\sigma/E = 70\%/\sqrt{E}$ for pions [93].

The η segmentation of the endcaps (HE) has lower granularity and varies from 0.09 to 0.35 covering pseudorapidity range of $1.3 < |\eta| < 3.0$ with the same total number of towers. The outer detector (HO) is located in the barrel region outside of the magnet coil and serves as a "tail-catcher". It reduces the non-gaussian tails in the energy resolution and improves the missing energy resolution of the calorimeter.

Located between $3 < |\eta| < 5$ units of pseudorapidity, the hadron forward calorimeter (HF) is made of quartz fibers. Particles which pass through the fibers produce Cherenkov radiation which is carried by the fibers to the photomultipliers. In total, the HF contains 1800 towers. In heavy ion collisions it is used to determine collision centrality. In this way, the centrality determination is the least biased by the presence of jets of interest in the barrel region.

The hadron and electromagnetic calorimeters capture nearly all the energy from jets. Since the granularity of the ECAL is much finer than of the HCAL, the final calorimeter towers are formed by addition of the signal from ECAL and HCAL into the $\eta - \phi$ bins corresponding to the HCAL cells. In the end there are 4176 such towers which are usually presented as a "lego" plot as on Fig. 2.6.

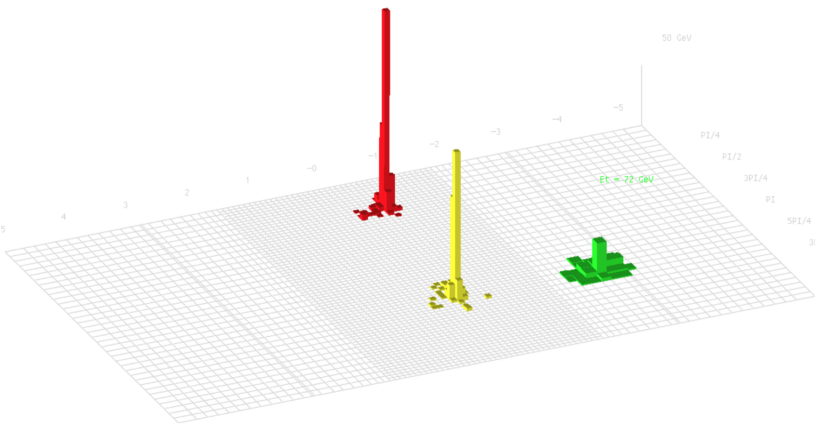

Figure 2.6: Segmentation of CMS calorimeters in $\eta - \phi$ space [27]

2.2.4 Muon chambers

The cross-section of a muon interacting with ordinary matter is small and therefore the muon easily penetrates calorimeters and the magnet. The muon chambers are located outside of the magnet and are the most distant of the detectors from the interaction point. Because of the large surface to be covered and also different radiation radiation exposure at different rapidities, the muon detector is made from three different types of gaseous chambers [94].

The barrel region ($|\eta| < 1.2$) consists of drift tubes (DT) containing 250 chambers organized in 4 layers. In the endcaps, Cathode Strip Chambers (CSC) cover the pseudorapidity range up to 2.4 units of pseudorapidity. In addition, Resistive Plate Chambers (RPC) which provide a fast response with a good time resolution but with coarser resolution of the position measurement than DT and CSC are used in both barrel and endcaps (Fig. 2.7, left).

The kinematics of the muon is measured with the muon chambers as well as in the tracker. At low muon momentum the multiple scattering and energy loss before the first muon chamber make the resolution in the muon chambers much larger than in the tracker. At very high momentum these effects can be neglected and the spatial resolution of chambers dominates. By combining two measurement one can improve the resolution of the muon momentum across the full range (Fig. 2.7, right).

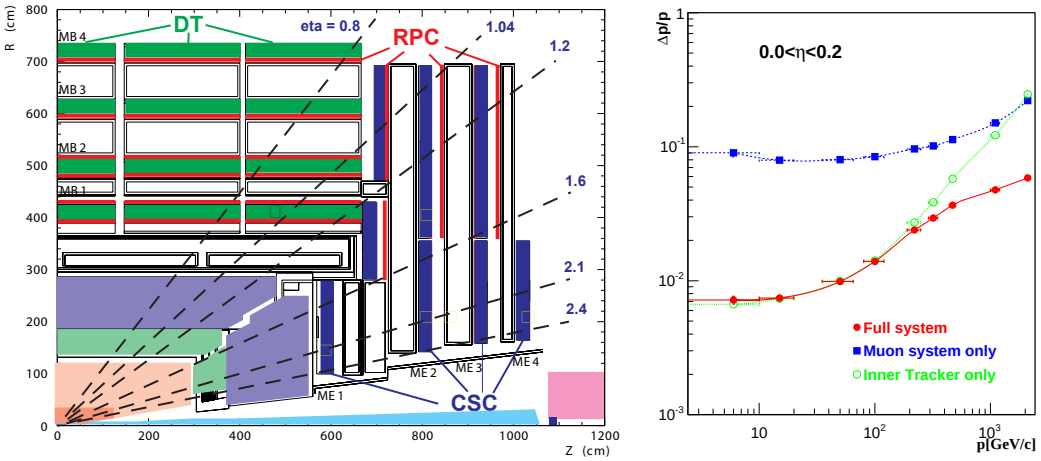

Figure 2.7: The layout of the CMS muon system (left); the resolution of the muon momentum measurement using muon systems only, tracker only and the combined measurement denoted as full system (right) [27].

2.2.5 Trigger

At the design luminosity, the LHC delivers $\sim 10^9$ collisions per second, while only $\sim 10^3$ can be recorded. Therefore, a triggering system is employed in order to reject events on-line. Such a rejection factor cannot be achieved solely by a computing farm because of bandwidth limitations. Instead a two level triggering system is employed, consisting of hardware and software triggers.

The level-1 trigger is composed of custom hardware processors located directly at the detector [95]. The decision is based on the "trigger primitive" objects like photons, electrons, muons or jets above predefined energy thresholds made of reduced granularity data. The design value of L1 rate is 100 kHz and is defined by the average time the full detector information is propagated through the readout system.

After the successful triggering of the Level-1 trigger, the data is transferred to the High Level Trigger which is designed to reduce the L1 output rate of 100 KHz to the average rate of 400 Hz available to the storage systems [96]. In total, the HLT was executed on approximately 13,000 CPU cores at the end of 2012. The HLT runs the software close to the full reconstruction, but is designed to reject an event as early as possible. The software is made as a set of HLT algorithms which run in a predefined order reconstructing and selecting physical objects.

Each algorithm is a sequence of programs of increasing complexity. For example, the selections based on the calorimeter and muon detectors are applied before the track reconstruction starts which is a more time-consuming step. When the event is selected by the HLT, it is routed to at least one of the streams and recorded by the data acquisition system (DAQ) locally on disk and eventually transferred to the CMS Tier-0 computing center for the permanent storage. A small fraction of the events is sent to an express stream which is reconstructed with high priority such that the reconstructed data is available hours after it is recorded to perform rapid data analysis. Calibrations, such as alignment and dead channel masks, are derived from the express stream and applied for the prompt calibration which follows two days later.

The Tier-0 is the top layer of the huge data storage and processing infrastructure called Worldwide LHC Computing Grid (WLHCG) [97] which is shared by all experiments. The Tier-0 accepts data from CMS DAQ and performs the first (prompt) reconstruction. Later data is sent to the large Tier-1 centers in CMS collaborating countries for data archiving, calibration, reconstruction and skimming (selecting subset of the data). From the Tier-1 the data is transferred to Tier-2 computing centers which are located in multiple laboratories around the world for the final analysis and storage of the processed data. The architecture of the system is designed to use the network resources to take optimal advantage of the available CPU and disk distributed around the world. More information about CMS computing systems can be found in Ref. [98].

2.3 Simulation

2.3.1 General issues

Monte-Carlo generators play an essential role in the preparation of the experiment and help the experimentalist to understand how the detector affects the measurements. Monte Carlo generators such as PYTHIA and HERWIG, are typically based on leading order pQCD calculations. This is insufficient for the physics of jets where the higher order and non-perturbative processes are essential in describing the jet structure.

The total cross-section of hard scattering partons can be calculated at the predefined order in pQCD with the remainder of the higher order. The computation of cross-section of exclusive final states, which is required in modeling of jets, is problematic due to collinear and infrared divergences. The collinear divergence appears when the outgoing parton splits collinearly into two particles separated by a small angle (e.g., as in $q \to qg$). Such term in the perturbative series is of the order of 1 at all orders of the perturbation series leading to the infinite result. The same happens when the soft particle is produced at any angle which is called a soft (or infrared) divergence. This problem is solved with the Kinoshita-Lee-Nauenberg theorem [99] which proves that the final state collinear and soft divergences cancel with the virtual corrections in the total cross-section. The virtual corrections are difficult to compute and one has to rely on "shortcuts" to make the generation process efficient.

Parton Showers is the approach to deal with multiple particle splitting before and after collision. As a consequence of the uncertainty principle, the radiation of the incoming particles becomes harder and harder approaching the hard scattering and softer and softer moving away from it. The hard space-like virtual fluctuations appear for a shorter period of time than soft ones, hence they become unimportant to the collision if they occur early. And respectively, the outgoing parton is the virtual off-shell particle which undergoes cascade of hard splittings first. The usage of shower algorithms allows one to compute the hard scattering cross-section up

to the Leading-Log (LL) order.

The Final State Radiation is the time-like showering of the outgoing parton. When the branching happens, the mother parton disappears and is replaced by daughter partners which then evolve separately. The variable that is used for the splitting is quite important. PYTHIA 6 uses invariant mass ordering of the splitting [100], while HERWIG uses angular-ordered showers [101]. In the end, the sum of all cross-sections of multiple final states is equal to the one of the hard scattering.

The Initial State Radiation is a set of virtual fluctuations that happen before the collision and would have collapsed if there was no collision. But some of those fluctuations can interact in the hard scattering and cannot recombine any longer. The natural description of the ISR shower is by the evolution of the parton densities using DGLAP equations. The shower can be developed to reconstruct the full picture of the partons available at the collision. However, the more efficient approach is to reconstruct the backward evolution given the hard scattering in the event until some non-perturbative scale.

Parton showers describe the structure of parton splitting before and after the collision with a reasonable accuracy without an infinite number of perturbative terms. On the other hand, matrix elements computations are exact up to an expansion order and preferred for largely separated object (e.g., jets). Their results must be merged to overlap double-counting. For more information about matching Parton Showers to Matrix Elements see Ref. [102].

The parton showers decrease the energy of the parton from the hard scattering scale down to the hadronization scale. At this scale, the coupling becomes large and the perturbative expansion breaks down hence one has to rely on models rather than first principles. One of such models is Lund model [103]. In this model the potential between quarks is described with linear potential $V(r) = \kappa r$ which is supported by the Lattice QCD computations [3] (Fig. 2.8). This potential represents a string of tension κ between two particles. As two quarks are separated apart, the potential between them grows and the creation of additional quark-antiquark pair happens thus breaking the string and creating two mesons. The production of baryons is obtained by creating a pair of di-quarks on the

string break. For the general review of physics behind Monte-Carlo generators see Ref. [104].

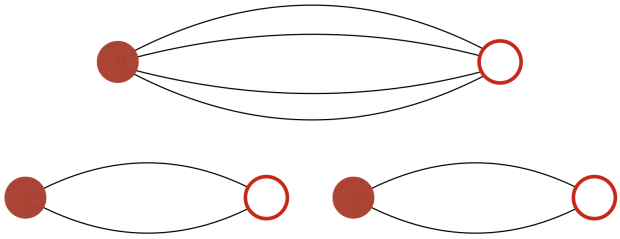

Figure 2.8: An illustration for the string breaking in the Lund model. The $q\bar{q}$ pair is being separated increasing the string potential (top), the quark-antiquark pair is born between the original pair thus breaking the string and forming two mesons (bottom).

2.3.2 PYTHIA

PYTHIA is a general purpose leading-order generator which uses the Lund model for the hadronization. Currently, two versions of Pythia are used: Pythia 6 [105] and Pythia 8 [106] which are quite different. For example, Pythia 8 uses transverse-momentum ordered parton showers, while Pythia 6 uses mass-ordered. Although Pythia 8 is currently a standard in LHC experiments, it failed to describe the transverse momentum balance of dijets in this analysis. Figure 2.9 shows the comparison of transverse momentum balance of dijets in pp data and simulation. It is obvious that Pythia 6 describes data better than Pythia 8, and therefore it was used in simulation studies in this analysis. However, neither of them describe the data perfectly, which is a reminder that a simulation may "look like data and feel like data, and if one is not careful they are accepted as if they were data." (J.D. Bjorken [107]). Although one observable may be well described by the simulation, another one may disagree with the data substantially.

2.3.3 Heavy ions generators

The physics of heavy ion collisions cannot be derived from first principles and relies on the models. First of all, one is interested in the modification of the hard scattering in the presence of the medium. This can be done by modifying the Pythia event as in Pyquen event generator [108]. It includes the simulation of the

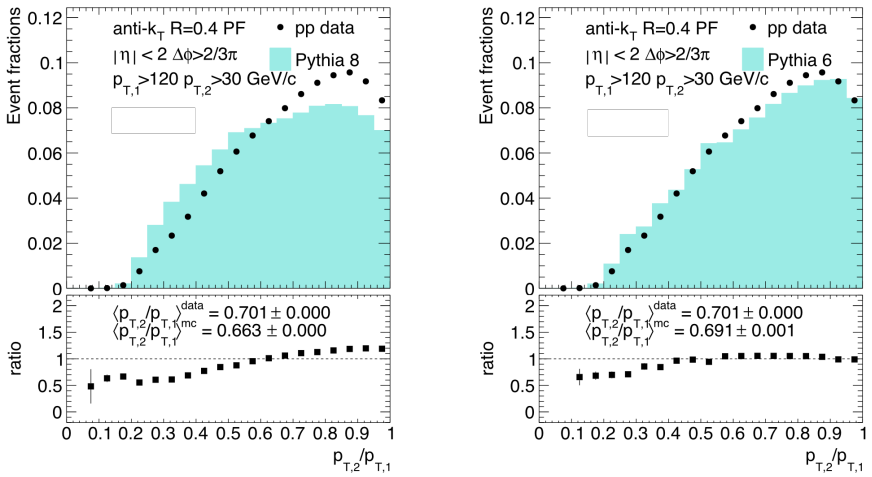

Figure 2.9: Data-simulation comparison of transverse momentum balance of dijets with Pythia 8 and Pythia 6.

parton scattering inside the medium and incorporates the collisional and radiative energy loss corresponding to the path length through the quark-gluon plasma.

In the Hydjet event generator [109], Pyquen is used to produce hard collisions proportionally to the number of binary nucleon-nucleon collisions at a given impact parameter according to the Glauber model. The other part of the heavy ions event is the soft component from the underlying event, which is modeled as the hydrodynamical flow. The hadron spectrum is modeled as a thermal distribution while the collective flow is introduced under the assumption that the ellipticity of the system is dictated by the initial overlap of the nuclei.

Although heavy-ion generators can simulate the underlying event as well as the hard scattering, such a "full" approach is not practical for the studies of hard scattering. Instead, the hard scattering signal event is simulated separately and later "embedded" into the heavy ions background event either simulated by a heavy ion event generator or even real data [110]. This approach makes sense as long as the hard scattering is much harder than the soft background of underlying event. The embedding technique is extremely useful for the investigation of jet performance in heavy-ions collisions and is used in this analysis as well.

2.3.4 Reconstruction of MC event

The purpose of event generators is to mimic the scattering of accelerated particles (e.g., protons or nuclei), and the output of the generator is a set of particles just after the collision. In order to simulate the full reconstruction of the event, one has to take into account the propagation of particles through the matter of the detector. This is generally achieved with the Geant4 simulation toolkit [111]. Geant4 can simulate the passage of particle in the wide range of energies (from 250 eV up to TeV scale) and handle complex geometries of the detector.

As a result of the event generation and simulation, the experimentalist sees the event as if it was recorded during the data taking, but with a full control at every stage. Then one can isolate the problems of event reconstruction from the real physical observation. For example, from the knowledge of the true particle trajectories and the hits that are left in the tracker one can tune the track reconstruction to the optimal parameters as well as estimate which part of original trajectories has been correctly found (efficiency) or how many random, or combinatorial, tracks have been found together with the real tracks (purity).

Another important application of the simulation is to obtain experimental jet resolution. One defines jets using an appropriate jet clustering algorithm such as anti-k$_T$, as described in Sec. 1.2.6. One can use the reconstructed particles to obtain *reconstructed jets* as well as generated particles (before propagating them through the detector) to obtain *generated jets*. The matching between generator jets and reconstructed jets is usually made by the requirement of the angular distance $\Delta R = \sqrt{\Delta\phi^2 + \Delta\eta^2}$ be less than the radius parameter of the jet algorithm. By comparing energies of generated and reconstructed jets one can identify detector response as well as jet resolution.

B-jets in Pythia6

As this analysis considers transverse imbalance of b-dijets, one has to define the b-jet in the simulation. The jet is matched to the flavor if there is a parton of any p_{T} in the $\Delta R = \sqrt{\Delta\phi^2 + \Delta\eta^2} < 0.3$ vicinity of the reconstructed jet. In order

to resolve ambiguities, the following hierarchy is assumed: if there is a b-quark in the vicinity, the jet is considered a b-jet; if not, but there is a c-quark then it is a c-jet; otherwise this jet is considered a "light" jet. The hierarchy is necessary because the b-quark typically decays into a c-quark.

2.3.5 Samples for the analysis

In this analysis two set of samples have been used: Pythia 6 for simulations of proton-proton collisions and Pythia 6 + Hydjet embedded samples for PbPb collisions. In order to augment the statistics some samples were generated with some phase space restrictions and then merged. The procedure is dependent on the properties of the hard scattering, and not on the underlying event in PbPb collisions therefore the merging procedure is the same for pp and PbPb samples.

Merging samples with different minimum $\hat{p}_{\mathrm{T}}$

The cross-section of hard inelastic parton scattering is a falling spectrum: the probability of the collision with parton momentum (denoted as $\hat{p}_{\mathrm{T}}$) of 140 GeV is 1000 times smaller than with probability of 40 GeV. In order to propagate the full phase space with the reasonable statistics the samples with different minimum $\hat{p}_{\mathrm{T}}$ were generated and then merged with the following weights formula: weight = σ/N where σ denotes the cross-section of the hard process, and N is the number of events in the corresponding $\hat{p}_{\mathrm{T}}$ bin.

Figure 2.10 shows the merging of Pythia 6 QCD samples with different minimum $\hat{p}_{\mathrm{T}}$. Points with error bars show the cross-section of hard process with $\hat{p}_{\mathrm{T}}>$ 30 GeV sample. One can see that the statistics for $\hat{p}_{\mathrm{T}}>$ 100 GeV is not satisfactory. The line represents 3 samples with $\hat{p}_{\mathrm{T}}> 30, 50, 80, 120$ GeV overlaid. Without proper weighting samples do not represent the spectrum correctly. The red points shows the merged spectrum with negligible error bars.

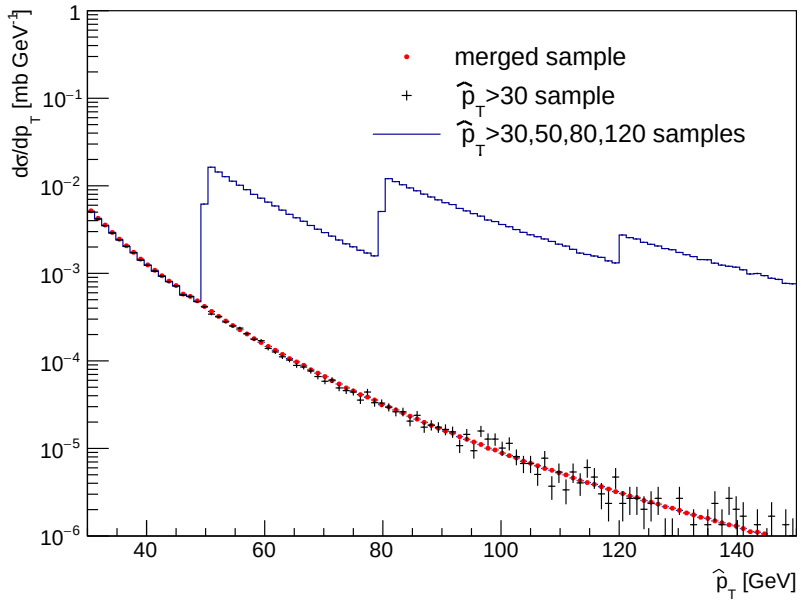

Figure 2.10: Merging of samples with different minimum $\hat{p}_{\mathrm{T}}$. Statistical errors on the merged sample are insignificant along the full $\hat{p}_{\mathrm{T}}$ range.

b-jet sample

This analysis requires a sample of b-jets. In QCD sample, only $\sim 3\%$ of jets originate from b-quark. As a result, the effective size of the sample for b-jets is decreased 30 times. In order to increase the number of b-jets in the simulation, a dedicated sample which filters on events with a b-quark is used. The usefulness of this sample comes from the fact that the generation of the pp event is much faster than the full simulation through the detector and reconstruction. Therefore one can generate 30 times more events and reconstruct only the portion of them without an impact on the timing of the simulation process and storage.

Figure 2.11 shows the spectrum of inclusive leading jets (no requirement on the flavor) from the QCD sample, the spectrum of leading b-jets from the QCD sample, and the spectrum of leading b-jets from the filtered b-jet sample. The latter has obviously more b-jets while the sample size is approximately the same. In principle one can then merge the QCD sample with the b-jet filtered sample with the appropriate weighting. However in this analysis it was not done and two samples were used as follows: if at least one jet in the event is required to be a b-jet then a b-jet sample was used, otherwise a QCD sample was used.

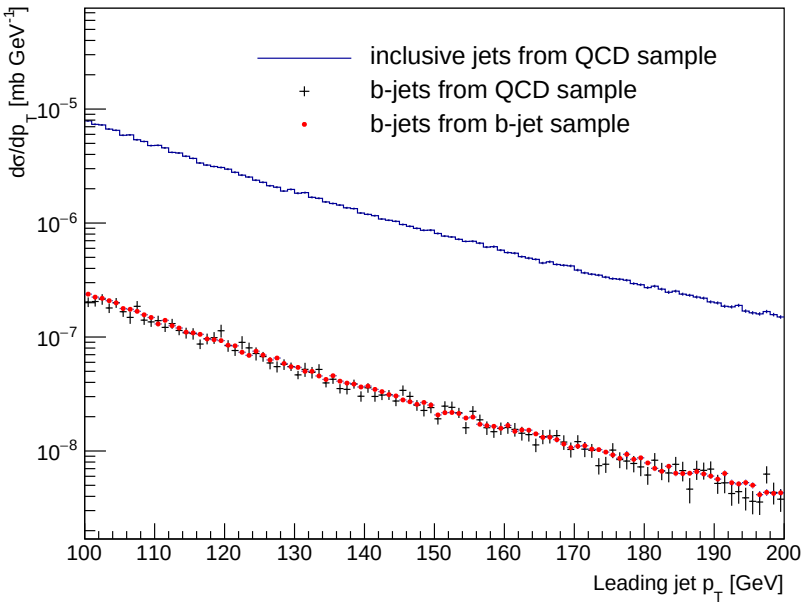

Figure 2.11: Merging of QCD and b-jet filtered samples. Statistical errors on the merged sample are insignificant along the full jet momentum range.

b-jet sample augmented with flavor creation

This analysis requires a pair of back-to-back b-jets presented in the event. The main contribution to such configuration comes from the Flavor Creation process of the b-jet production because other processes produce mainly different topologies. As is described in Sec. 1.2.4, this process is only a small part of the b-jet production at LHC, therefore a dedicated sample of Flavor Creation events (with Pythia setting MSEL=5) was created. This sample was later united with the Flavor Creation events from the b-jet sample and the weighting factor was recomputed for such events. The final b-jet sample augmented with Flavor Creation events was then used in the analysis.

2.3.6 Flavor process reweighting

The analysis described in Chapter 4 is focused on b-jet pairs separated by $\Delta\phi > 2/3\pi$ azimuthal angle requirement (back-to-back). The identification of b-jets (b-tagging) will be described in Sec. 3.3. Without providing too many details here, one can assume that in the data the b-jet selection is very pure: 90% of selected

dijets are both b-jets. When the analysis selection was applied, the transverse momentum balance of dijets was studied in pp data and Pythia 6.

Figure 2.12 shows the distributions of subleading to leading jet p_{T} ratio ($x_{\mathrm{J}} = p_{\mathrm{T},2}/p_{\mathrm{T},1}$) and azimuthal angle between jets ($\Delta\phi$) for b-tagged dijets in pp data compared to PYTHIA6 b-jet events, where the latter is separated into its component processes, described in Sec. 1.2.4: flavor creation (FCR), flavor excitation (FEX) and gluon splitting (GSP). The agreement between data and PYTHIA is poor compared to what is observed for inclusive dijets. PYTHIA shows a tendency towards imbalanced pairs, that is less apparent in the data. Pairs from the FEX and GSP processes tend to larger imbalance. This is expected as the underlying heavy flavor production process is more likely to lead to a 3-jet topology. A lobe of imbalanced jets appears in the simulation, which is dominated by the FEX process, and which is much less prominent in data.

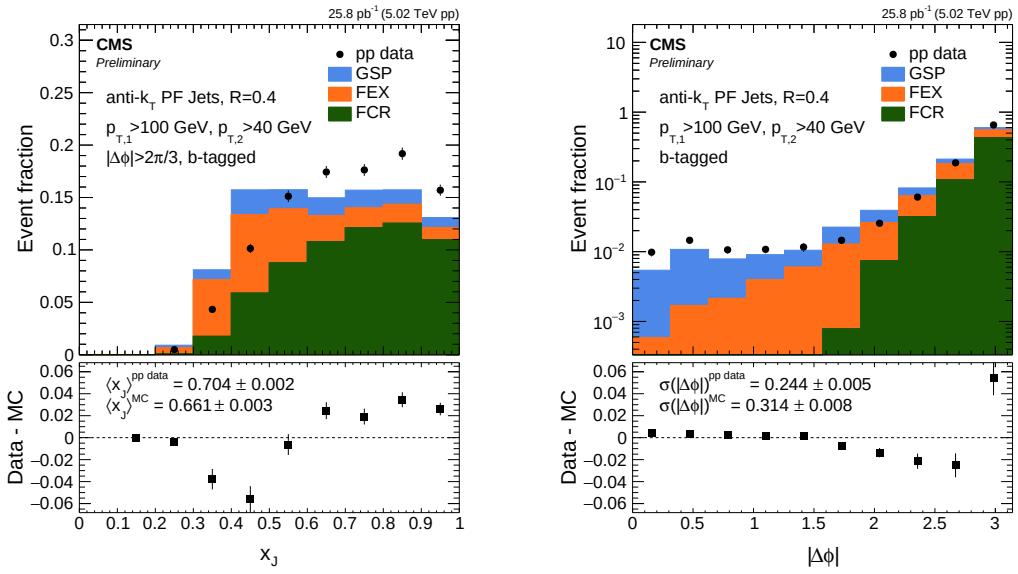

Figure 2.12: The distributions of x_{J} (left) and $\Delta\phi$ (right) in the leading-subleading analysis in Pythia 6 and pp data.

The "order" of the partner b-jet is shown in Fig. 2.15. The contribution of the third jets is larger in simulation than in data, and is dominated by FEX events. Based on this fact, we make the hypothesis that the NLO processes, FEX and GSP, are mismodeled in PYTHIA, which is, strictly speaking, a leading order generator. To obtain a better description, we perform what we refer to as *flavor process reweighting*, according to the following procedure. Three exclusive categories of

events are defined:

1. The top two jets are b-tagged and back-to-back ($\Delta\phi > 2/3\pi$)
2. The first and third jet are b-tagged and back-to-back ($\Delta\phi > 2/3\pi$)
3. The first and third jet are b-tagged and nearby ($\Delta\phi < 1/3\pi$)

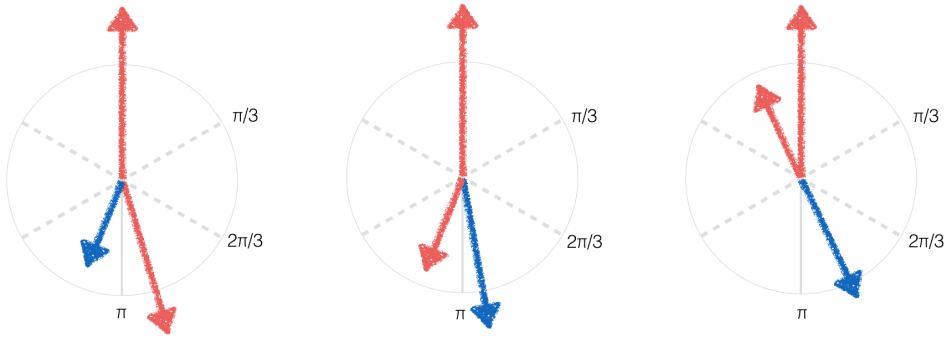

Figure 2.13: Categories of events used for process reweighting. Red arrows denote b-tagged jets, blue arrows denote light jets.

In simulation, these categories are dominated by FCR, FEX, and GSP events, respectively. We then reweight the simulation such that the relative abundance of these three categories of jets are the same as they are in data. The relative occurrence of the production processes in these categories are shown in Tab. 2.1. It is obvious that each category of events is dominated by corresponding process, therefore the relative frequency of each category determines fractions of processes as well. Table 2.2 shows relative occurrence of three categories in data and MC. It is obvious that while the first category (dominated by the FCR) is dominant in data, the second one (dominated by the FEX) is dominant in the simulation. Reweighting is performed so that relative frequencies of categories (Tab. 2.2) agree in data and simulation.

Category	FCR	FEX	GSP
$\lvert\Delta\phi_{1,2}\rvert > 2\pi/3$	57%	26%	17%
$\lvert\Delta\phi_{1,3}\rvert > 2\pi/3$	11%	62%	27%
$\lvert\Delta\phi_{1,3}\rvert < \pi/3$	0%	17%	83%

Table 2.1: Relative contributions of production process in PYTHIA to jet pair categories.

Category	Data	MC
$\lvert\Delta\phi_{1,2}\rvert > 2\pi/3$	56%	46%
$\lvert\Delta\phi_{1,3}\rvert > 2\pi/3$	37%	49%
$\lvert\Delta\phi_{1,3}\rvert < \pi/3$	7%	5%

Table 2.2: Relative contributions of jet pair categories in pp data and PYTHIA.

Figure 2.14 shows the x_J and $\Delta\phi$ distributions after reweighting. Figure 2.15 shows the order of the partner b-jet before and after reweighting. An improved description of all of these observables is found after reweighting.

The b-jet Monte Carlo is reweighted for all subsequent comparisons. One has to be careful with applying the weighting factors. Only the events with b-dijets have to be reweighted, while events with a single b-jet must not be corrected. The reason is that as it was shown on Fig. 1.12, the total b-jet cross-section is correctly described by Pythia. The application of weights in this case leads to the improper description of b-jet cross-section and, in particular to this analysis, to the underestimation of mistagging of non-b-jets, as will be discussed in Sec. 4.7. Therefore only when events with b-dijets are selected, the weighting is applied. The weighting procedure allows us to obtain a better description of the b-dijet kinematics in the simulation, and is used in the measurement of transverse momentum imbalance, that is discussed in Chapter 4.

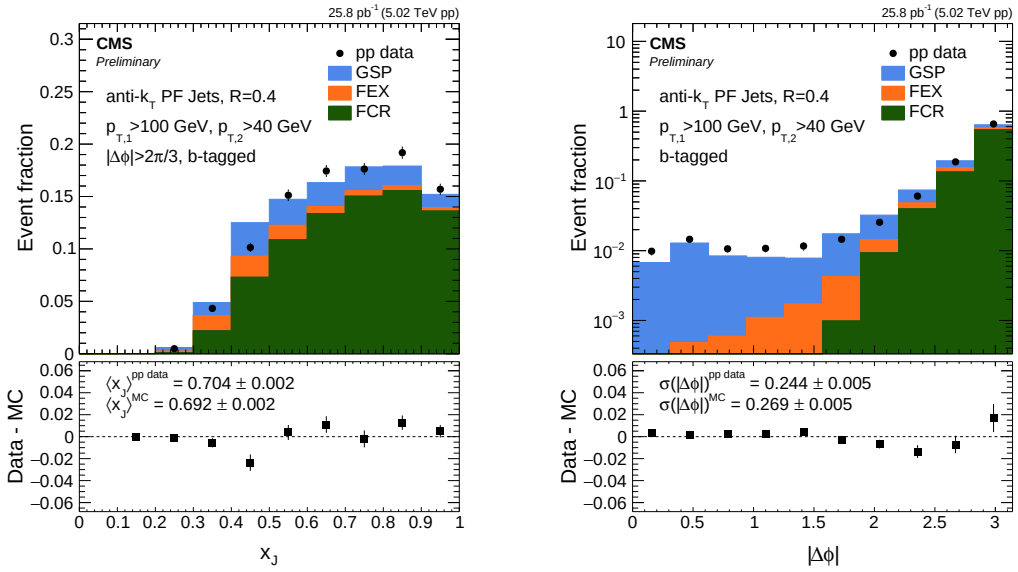

Figure 2.14: The distributions of x_J (left) and $\Delta\phi$ (right) after flavor process reweighting in Pythia 6 and pp data.

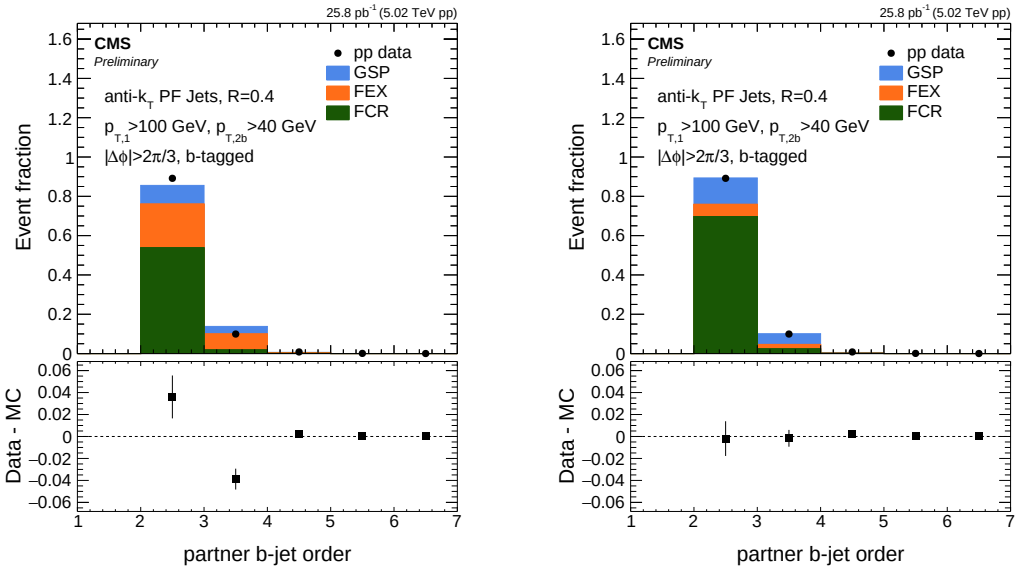

Figure 2.15: The distribution of the order of the partner b-jet before (left) and after (right) flavor process reweighting in Pythia 6 and pp data.

Object reconstruction and selection

3.1 Charged particle tracking

Charged particles that are created in high energy collisions move away from the collision area and traverse thin silicon layers of the tracker detector. Ionizing the material of the tracker, particles provide a position measurement (called a *hit*) along the trajectory. The problem of tracking is to reconstruct the initial particle trajectories from the set of hits in order to provide a high precision measurement of momenta of charged hadrons.

The tracking development described in Sec. 3.1.2 and 3.1.3 was a major component of the thesis project and fulfilled CMS authorship requirements.

3.1.1 Track reconstruction

As the CMS magnet is a solenoid, the magnetic field in the tracker is close to uniform [112] such that charged particles follow helical paths. In order to describe the helix one needs five independent parameters, for example, direction of propagation (2 parameters), radius, pitch (longitudinal distance between turns) and azimuthal angle. Among different parameterizations, the following is the most suitable for tracking purposes:

- the transverse momentum, p_{T}, which defines the curvature,
- transverse d_{xy} and longitudinal d_z impact parameters - the distance of closest approach of the track to the beam axis,

- the azimuthal ϕ and polar θ angles of the tangent to the track at the point of closest approach.

An example of a collision with 100 tracks is shown on Fig. 3.1. Typically one can see $\sim 10^2 - 10^3$ tracks in pp collision and $\sim 10^3 - 10^4$ in PbPb collisions. This results in ~ 100 thousand hits in the detector. It is clear that a brute force combinatorial approach is not practical and one needs to incorporate knowledge of the track model (helix) to eliminate hit combinations that do not correspond to real charged particles. One can also restrict some of the parameters of the helix, e.g. restricting impact parameters d_{xy} and d_z to be close to zero to effectively allow for only 3 degrees of freedom which speeds up track finding. After the track is found, its hits can be removed to speed up the reconstruction of subsequent tracks and allow for more complicated configurations.

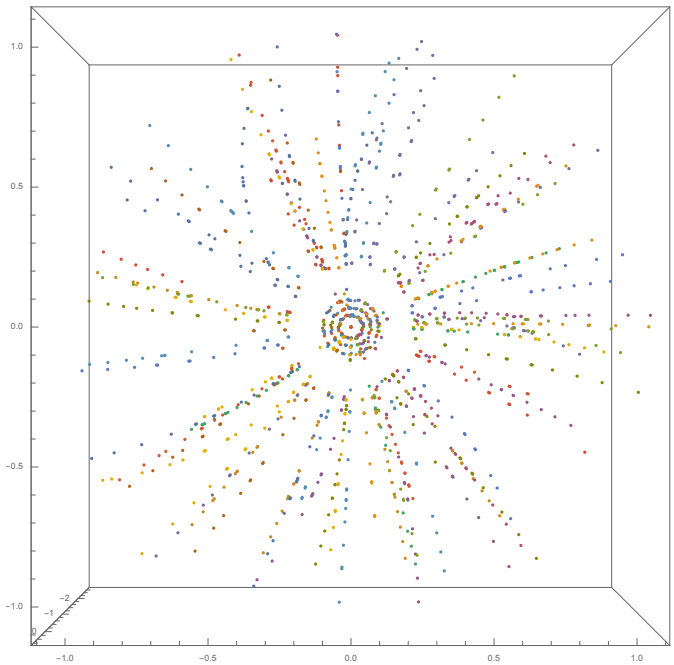

Figure 3.1: The set of hits in CMS tracker corresponding to 100 tracks. Hits of the same color correspond to the same track.

The discussion below follows [26]. In general, the track reconstruction consists of the following steps:

Seeding is combining several hits into a *seed* in order to produce an initial estimate of the track trajectory. Usually it is done from the inside, where the tracker device has the highest resolution (e.g. the pixel layers in CMS) or from the outside

where the particles density is lowest. In order to fit a helix trajectory at least 3 points are necessary. For the Run 2 settings of heavy ion collisions the seeds are produced with 3 pixel hits (pixel triplet) or 2 pixel hits and the primary vertex requirement (pixel pairs). Other combinations are also possible (and used for pp reconstruction) like combinations of pixel and strip layers (mixed triplets) or seeding with strip layers only. In order to reduce the number of seeds, they are required to satisfy some conditions of p_{T}, their consistency with primary vertex, etc.

Track following. When the initial trajectory parameters are defined, the outward projection onto the subsequent layers allows for a significant reduction in the number of combinatorial candidates. The track finder is based on the Kalman filter [113, 114, 115] which estimates parameters of the trajectory for each consecutive layer and predicts the intersection of the trajectory with the next layer. This is usually the most time consuming step. During the propagation through the tracker layers the particle loses energy and deviates from its original direction. This is taken into account by including the estimated scattering angle in the uncertainty of trajectory parameters as well as the adjustment of the momentum of the trajectory by the predicted mean energy loss given by the Bethe-Bloch equation [116]. If there are no hits compatible with the track trajectory found, a "ghost" hit may be added to represent the case when the particle failed to produce a hit in the module e.g., because of its inefficiency. From each track candidate reconstructed so far, the new candidates are formed by adding only one hit from the detector module. In order to avoid a rapid increase of the combinatorial candidates, only a limited number of them are retained at each step (the default is 5). This parameter should depend on the complexity of the tracking problem. For example, if this parameter is 5 in a very dense environment, after propagating to 10 layers, one could theoretically produce 10 million trajectories from a single seed.

Track fitting is carried out after the full trajectory is formed. The Kalman filter is used in this step two times: to propagate the fitting from the inside to the outside of the tracker and in the opposite direction. This allows to define a

track parameters at any surface along the track and to extrapolate the trajectory inside to the interaction region and outside to the calorimeter and muon detectors. The more sophisticated estimation of track propagation between layers takes into account inhomogeneity of the magnetic field in the detector. The final fits are passed then to the selection step.

Track selection is a set of cuts assigned to separate *real* tracks which result from the propagation of real particles from *fake* tracks which results from combinatorial hits which happen to form trajectories that resemble helices. For example, χ^2 of the track fit per degree of freedom per layer must not exceed 0.15, and number of hits in the track cannot be less than 13, etc.

3.1.2 Iterative tracking

The CMS tracking software exploits an iterative approach to the reconstruction of charged particles [26]. Tracks that can be found more easily are reconstructed first, then the hits corresponding to these tracks are removed from the event and the next iteration proceeds.

During the first heavy-ion run in 2010 – 2011, only a single iteration was used, which targeted primary tracks (i.e., tracks compatible with the primary vertex) with p_{T} above 1 GeV. The tracking for LHC Run 2 has been significantly improved using four iterations described below. The main difference between the iterations are the parameters of the seeding step, where only a few layers are used.

The **Primary step** reconstructs tracks with p_{T} above 900 MeV which compatible with the primary vertex. This step contributes to the majority of tracks found and it was the only step in the heavy-ion tracking during Run 1 of the LHC.

The **Low-p_{T} step** is dedicated to tracks with p_{T} above 400 MeV. This step does not play a significant role in the b-jet measurement, but is very important for the research of collective phenomena in heavy-ion collisions. Due to the large bending angle of low-p_{T} tracks and (relatively) large multiple scattering, the number of combinations grows very fast with decreasing track p_{T}. As a consequence, this step made the tracking extremely slow. However, with an additional refitting

step of the seeds (between seeding and track finding steps) the number of seed candidates was reduced more than twice and the reconstruction time was improved significantly. Without seed refitting, the seed resolution is poor and track finding has to deal with tracks of $p_{\mathrm{T}} \sim 300$ GeV. Because of the falling spectrum of tracks, this defines the majority low-p_{T} tracks which are then followed but discarded in the selection step. The additional refitting of seeds makes a more sharp cut on the seed p_{T}, and decreases the number of candidates for the track finder. In the end, the number of tracks above 400 MeV is left almost unchanged (Fig. 3.2, left), while total number of tracks is decreased. On the Fig. 3.2 (right) the duration of the low-pt step is shown as a function of the particles number in the collision for the standard triplet (green) and refitted seed track (red).

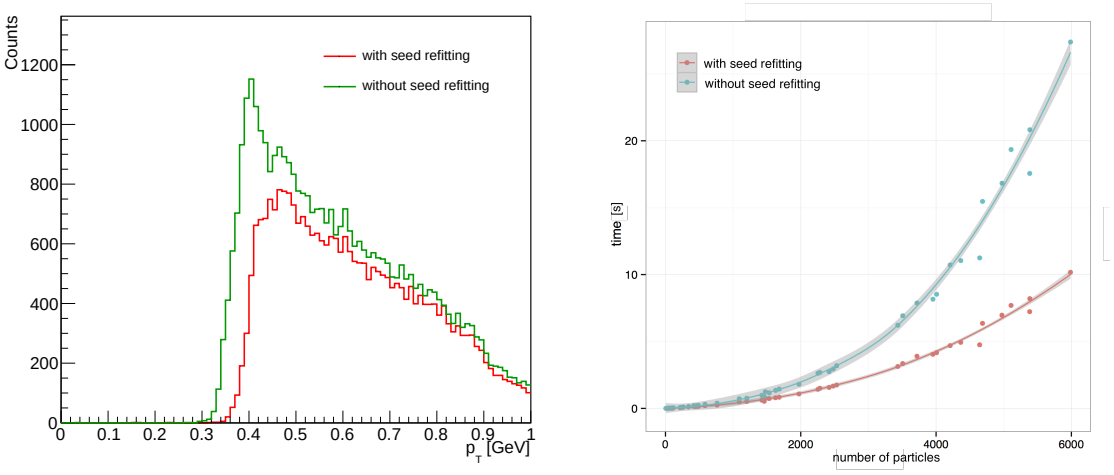

Figure 3.2: Distribution of track p_{T} from the low-p_{T} step after the full reconstruction with and without seeds refitting (left). The timing of low-p_{T} step vs number of particles in the event, lines are the polynomial fits to the data points (right).

The **Detached step** is an iteration dedicated to the reconstruction of tracks with impact parameter up to 5 mm. This step plays a crucial role in the b-jet identification as will be described in Sec. 3.3. Figure 3.3 shows the comparison of the distribution of the impact parameter significance i.e. ratio of the track impact parameter value to its estimated error in the transverse plane for tracks reconstructed without the detached step (red), tracks with detached step (blue) and for the pp reconstruction (green). The distribution of the impact parameter in pp is still wider because the pp reconstruction has additional exotic iterations such as mixed triplets and pixel-less seeding which are unfeasible for the heavy-ion

reconstruction by timing constraints.

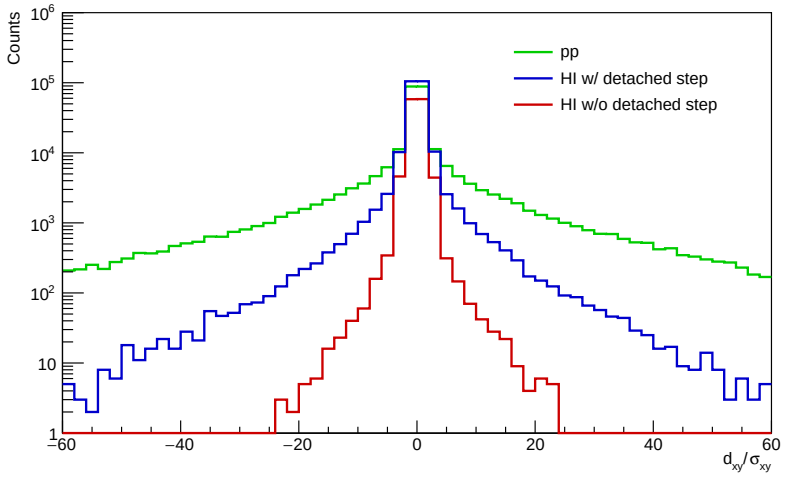

Figure 3.3: Transverse impact parameter significance distribution. Red: original heavy-ion reconstruction, blue: heavy-ion reconstruction with detached step, green: pp reconstruction.

Pixel pair step is dedicated to primary tracks which have only 2 pixel hits and a very tight condition on the primary vertex. Although the single hit efficiency in the pixel detector is very high $\sim 97\%$ [117], around 10% of tracks have 2 out of 3 pixel hits. These tracks arise when a particle crosses a non-active area in one of the three pixel layers. This step is intended to recover such tracks. In this case the primary vertex position is crucial to determine the parameter of the track and it is constrained 40 times tighter than for the primary step.

The contribution of different iterations to the total number of reconstructed tracks and to the total timing is shown on Fig. 3.4.

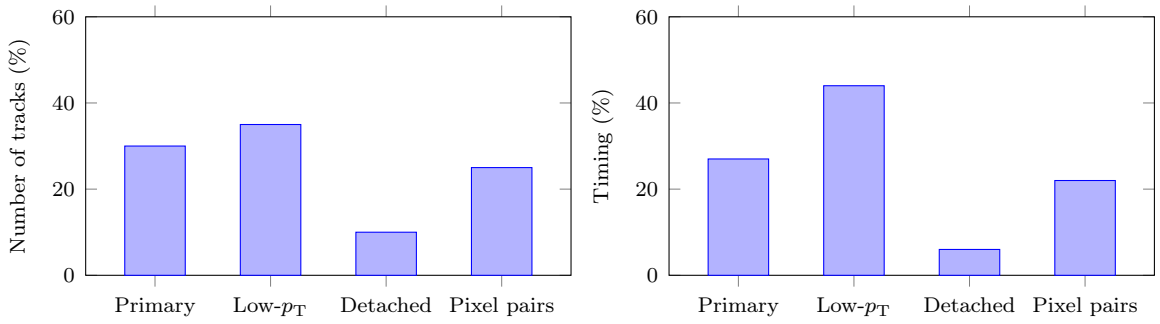

Figure 3.4: Contribution of each iteration to the total number of reconstructed tracks (left) and reconstruction time (right) in PbPb collision.

The improvement of the track reconstruction to b physics was demonstrated on

the reconstruction of B-mesons from the $B^+ \to J/\psi + K^+$ decay [28]. Figure 3.5 shows the signal and background fits to the invariant B-meson mass distributions with only one primary step tracking (left) and with all tracking iterations including detached step (right). The detached step which recovers tracks with large impact parameter from B-meson decays results in the increase of the signal yield almost twice from 21 to 38 candidates.

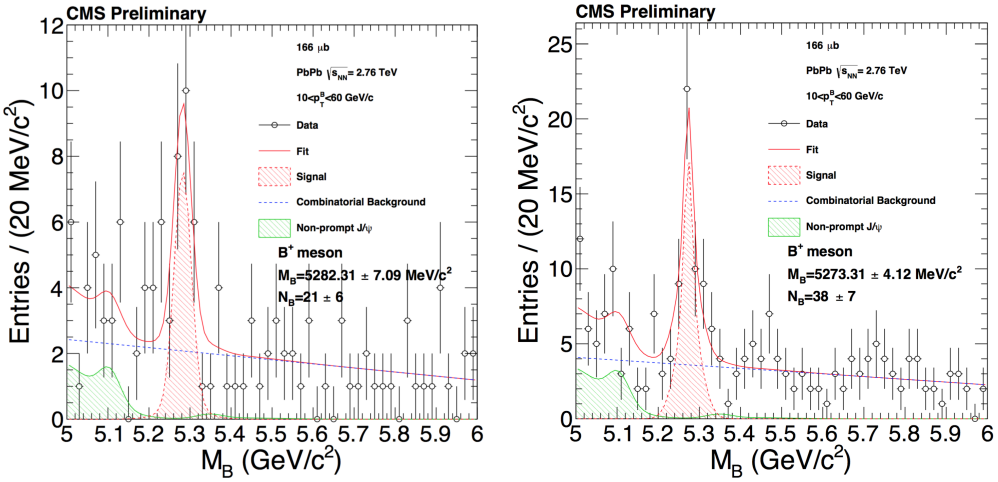

Figure 3.5: B meson reconstruction with only one primary iteration (left) and all iterations (right). The signal yield is increased from 21 to 38 candidates. [28]

3.1.3 Track selection

The track reconstruction is not perfect. The finite spatial resolution of hits, in particular in the strip layers, and in general the combinatorial nature of the problem give rise to fake tracks, i.e. tracks that only appear as a particle trajectory while there was no particle that moved along it. Because of the multiple Coulomb scatterings in the tracker silicon layers the track is subject to deviations from the ideal helix model. Sometimes the particle participates in nuclear interactions inside the tracker and does not propagate anymore, leaving not enough hits in the tracker. In both cases the track may not be reconstructed. These two effects are absorbed into the definitions of

- **efficiency** is the fraction of correctly reconstructed in the total number of primary tracks (i.e. tracks originating from the collision area) created in the event (Fig. 3.6 left)

- **fake rate** is the fraction of fake tracks in the set of reconstructed particles (Fig. 3.6 right)

In the simulation one can identify which particle leaves a particular hit. The track is considered to be reconstructed correctly if at least 75% of its hits come from the same particle. Given the definition of reconstructed track, it is easy to find the efficiency and fake rate in simulation. The efficiency and fake rate plotted as a function of the track transverse momentum p_{T} in PbPb collisions are shown on Fig. 3.6. The track can also be reconstructed multiple times i.e., the simulated track is associated to several reconstructed tracks, but the contribution of such tracks is small.

Along with simulation definition there are data-driven methods for the tracking efficiency determination based on the relative frequencies of three- to five-prong decays of reconstructed D^{*} and they are found to be compatible with the simulation within 6.5% uncertainty [35] (for more details about data-driven efficiency estimation see Ref. [118]).

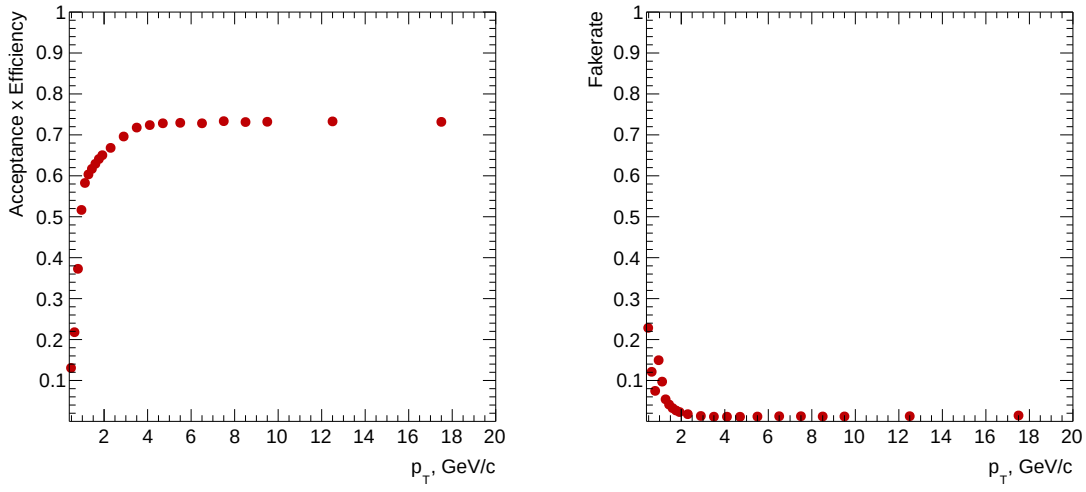

Figure 3.6: Efficiency (left) and fake rate (right) as a function of track p_{T} in PbPb collisions.

The task of the track selection is to reduce the number of fake tracks with the smallest possible decrease of the correctly reconstructed tracks. Traditionally it is made with a cut-based selection on the following variables:

- χ^2 per degree of freedom of the track fit
- d_{xy}/σ_{xy}, transverse impact parameter significance
- d_z/σ_z, longitudinal impact parameter significance
- $\Delta p_{\mathrm{T}}/p_{\mathrm{T}}$, relative p_{T} error
- Number of layers
- Number of hits, different from the number of layers because each layer can have multiple hits

Although the selection reduces fake rate to $\sim 1\%$ for $p_{\mathrm{T}} \sim 10$ GeV, the fraction of correctly reconstructed particles (efficiency) drops by $\sim 20\%$. In order to mitigate this effect, a more sophisticated selection was developed.

The cut-based selection can be illustrated as a list of cuts:

variable		cut
$\chi^2/N_{d.o.f.}/N_{layers}$	$<$	0.15
N_{hits}	$>$	13
$\Delta p_{\mathrm{T}}/p_{\mathrm{T}}$	$<$	0.1

Despite these cut values, tracks with 12 hits, for example, are not always fake tracks; missing hits may occur because of dead areas in strip modules or gaps between layers. However, tracks with lower number of hits would require tighter cuts on other variables to obtain a low fake rate.

Another important observation about track selection can be made by looking at the η distribution of real/fake tracks on Fig. 3.7 (left). This plot looks very similar to the thickness of tracker material that is traversed by the particle (Fig. 3.7, right). As we can see, the endcaps of the CMS tracker have much more material than in the inner barrel, therefore the particle undergoes more deviations from the ideal helix trajectory there. As a result, the reconstruction is more difficult and the fake rate is higher.

It seems advantageous to use selection on multiple dependent variables at the same time. The analysis of the impact of multiple dependent variables on the

outcome is generally called a multivariate analysis (MVA) [119]. In the case of track selection it is used to separate true and fake tracks based on their properties and fit qualities.

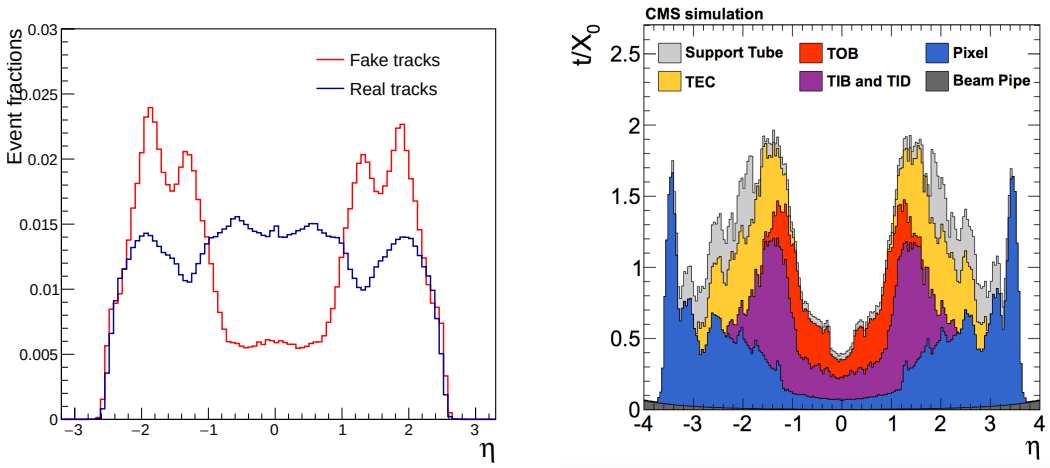

Figure 3.7: The fake rate is strongly dependent on the amount of tracker material the particle traverses. Left: pseudorapidity distribution of fake tracks and real tracks in PbPb collisions. Right: total thickness of the tracker material as a function of η [26].

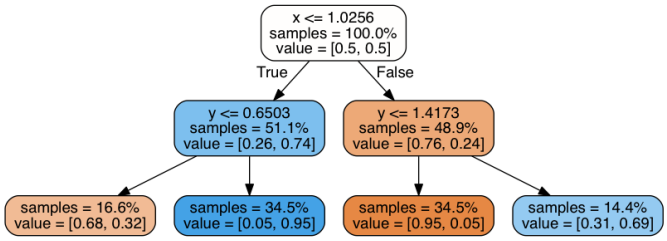

Figure 3.8: An example of a decision tree of depth 2.

The selection based on *decision trees* [120] is a development of the cut-based selections. In a decision tree, cuts are not independent, but organized in a hierarchical order, as shown on Fig. 3.8. At each level a single decision divides the sample in two parts and future decisions are made on the two subsamples separately. The separation is performed so that the proportions of each class in the subsample (denoted as "value" on the Fig. 3.8) are maximized. At the bottom level of the tree, the subsample is small enough to contain the majority of one class. The simple decision tree does not give an exceptional classification performance. Even better results can be achieved by growing a huge decision tree (as in algorithms ID3 [121], C4.5 [122]) or combining multiple simple decision trees together (Random Forest [123], AdaBoost [124], Gradient Boosting [125]). For more information about machine learning algorithms see Ref. [126].

As an example consider the data of two classes: background (+) and signal (o) generated on the two-dimensional (x, y) space above and below the separation boundary $y = x$, respectively (Fig. 3.9). Note that some noise is allowed in this simulation and some of the examples are located at the opposite side of the boundary. This implies that even knowing the true decision boundary $y = x$ does not allow to classify samples with 100% accuracy.

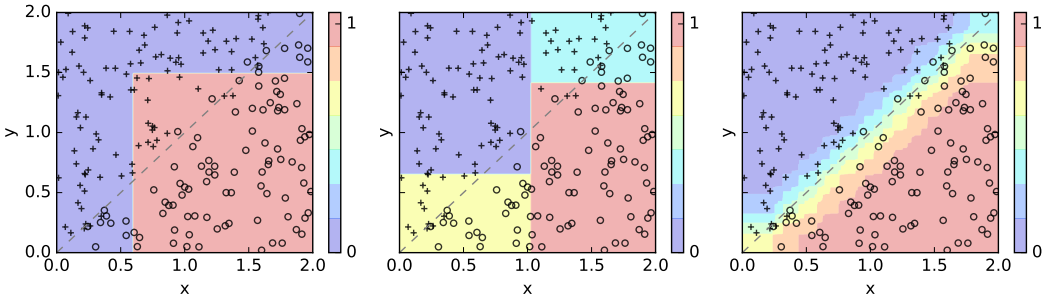

Figure 3.9: Decision boundaries of three algorithms: simple cut $x > 0.6, y < 1.5$, decision tree (from Fig. 3.8) and boosted decision trees with 5000 trees.

The simple cut of $x > 0.6, y < 1.5$ is shown as red background on Fig. 3.9 (left). Although the majority of the signal is captured by this cut, the efficiency (i.e. the fraction of the signal that is left after the cut) is only 84%, and the purity (i.e. the fraction of the signal in the selected by the cut sample) is 81%. The decision tree of depth 2 from Fig. 3.8 achieves a better performance (Fig. 3.9, middle). The color code represents the fraction of the signal in each subsample (denoted as "value" on Fig. 3.8). One can see that already in the two-branch decision tree this fraction takes values between 0 and 1, and assuming 0.5 as a decision boundary this algorithm achieves 87% efficiency and 86% purity.

Combining multiple trees together using the Boosted Decision Trees algorithm one can achieve an (almost) smooth decision boundary which will improve the classification accuracy as shown on Fig. 3.9 (right). In this example, 5000 decision trees of depth 2 are trained with the Gradient Boosting algorithm and the resulting value is the averaged classification score from all trees, giving 95% purity and efficiency. As a comparison, the separation by the true boundary $y = x$ has 96% purity and efficiency which is only marginally higher than the result achieved by using boosted decision trees.

This analysis uses Gradient Boosting decision trees with 500 iterations with decision trees of depth 4. The variables used for the classification are summarized on Fig. 3.10. In order to minimize the correlation between the physical properties of the reconstructed tracks and the classification error, different variable sets are used for different iterations: relative p_{T} error is used only in the low-p_{T} step, and impact parameter significance is not used for the detached step.

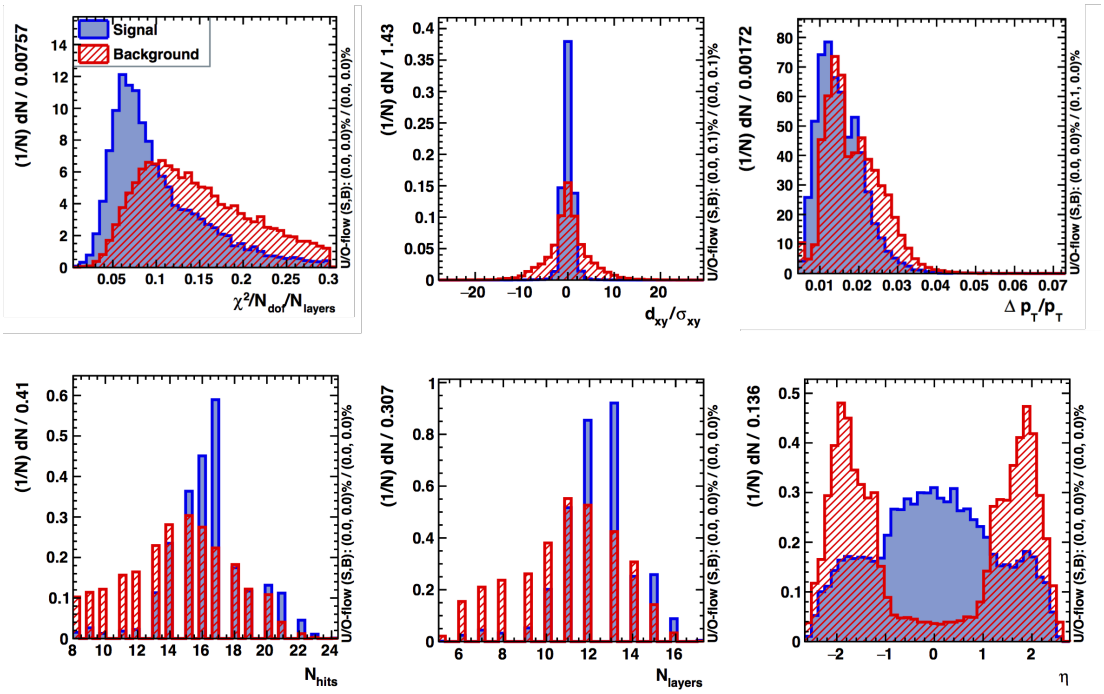

Figure 3.10: The list of variables used in the selection. Top row: χ^2/d.o.f/layer, transverse impact parameter significance, relative p_{T} error. Bottom row: Number of hits in the track, number of layers track traverses, pseudorapidity of the track. Signal corresponds to correctly reconstructed tracks, background corresponds to fake tracks. Not all the variables are used at each track iteration.

Figure 3.11 shows the efficiency and fake rate dependence on the track p_{T}. In general, the efficiency is improved by ∼10% while keeping about the same fake rate as for the cut-based selection.

It is interesting to see that the efficiencies of MVA and cut-based approach match in the endcap region (Fig. 3.12). The track reconstruction is generally more difficult in the endcaps due to the presence of large amount of material. Therefore the cut-based approach was tuned to match a reasonable fake rate in these areas. Although MVA did not improve the tracking efficiency in the endcaps (for the predefined threshold), it was able to improve the efficiency significantly in the

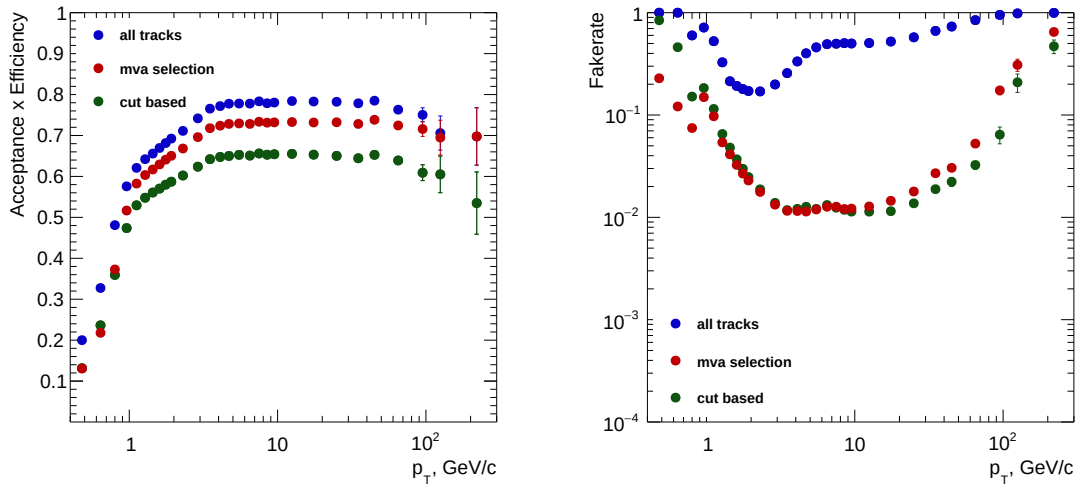

Figure 3.11: Efficiency (left) and fake rate (right) as a function of track transverse momentum in heavy ions collisions.

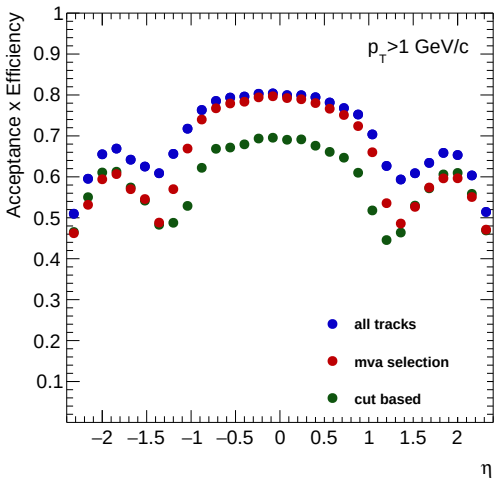

Figure 3.12: Efficiency as a function of track pseudorapidity in heavy ions collisions.

barrel region because track η is one of the selection variables.

3.2 Jet reconstruction

In the definition of jets as described in Sec. 1.2.6, such as anti-k$_T$ jets, one does not specify the objects the jets are made from. The basic approach is to cluster jets from energy in the calorimeter towers (calorimeter jets). In CMS, such jets suffer from the non-linear response of the calorimeters, as well as their relatively large energy resolution. A more advanced approach, called *Particle Flow*[127, 128], uses information from all parts of the detector significantly increasing the performance. In this section, the description of particle flow jets is presented followed by the study of their performance.

3.2.1 Particle Flow

In high energy collisions particles typically traverse multiple subdetector systems. For example, in CMS, they may interact with the tracker, electromagnetic and hadronic calorimeters and the muon chambers, as shown in Fig. 3.13. The information in each subdetector is grouped together to form objects such as tracks and calorimeter clusters. However, by using a particle flow algorithm to combine information from the subdetectors one may obtain more precise information about the particles kinematics.

A basic description of the CMS particle-flow algorithm, more thoroughly described in Refs [30, 129], is as follows. First, muon tracks from the muon chambers (*standalone* muon) are matched to the nearest track from the tracker (*tracker* muon) and the final fit is called *global* muon. If the momentum of the combined global muon p_{T} is compatible with tracker muon within 3σ then this global muon is called "particle flow muon". The corresponding track is removed from consideration and muon energy estimated from cosmic rays is subtracted from calorimeter clusters.

Electrons can be identified by the combination of tracks in the silicon tracker and one or more ECAL clusters. Because electrons lose their energy by bremsstrahlung in the tracker, their energy loss model is described by Bethe-Heitler model [130] which cannot be approximated by a single Gaussian, but only with a mixture of

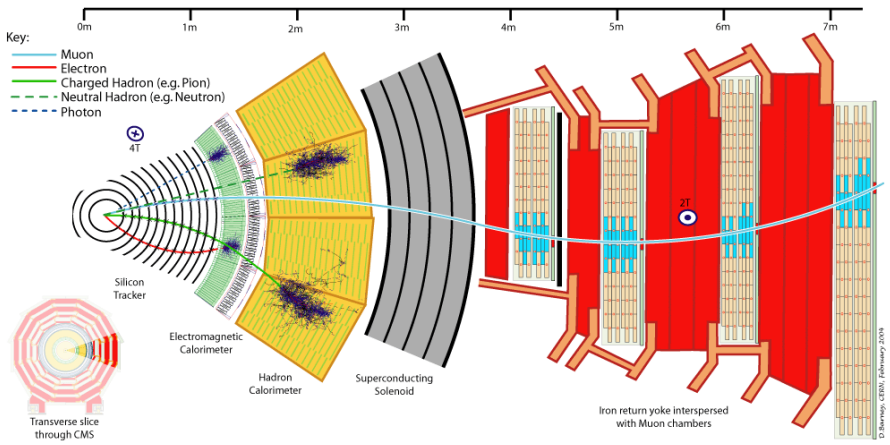

Figure 3.13: Different types of particles traversing the CMS detector [29].

them. Therefore, rather than the standard Kalman Filter, electron track candidates are fit with a so-called Gaussian-Sum Filter [131] and the final identification is performed with several variables from the tracks and ECAL clusters. If an electron is found, then "particle flow electron" is registered and its track and ECAL clusters are removed.

The remaining tracks that have not been identified as belonging to leptons and matched to ECAL and HCAL clusters are identified as "particle flow charged hadrons". The energy of charged particle, as measured by the tracker assuming the charged pion mass hypothesis, is subtracted from the calorimeters. The remainder of the energy from the ECAL and HCAL gives rise to "particle flow photons and neutral hadrons" respectively.

The usage of particle flow objects significantly improves the performance of jet reconstruction. On Fig. 3.14 (left) the jet response of Particle-Flow and Calorimeter jet is shown. The jet response and resolution are defined as a mean value and the standard deviation of ratio (Reco p_{T} − Gen p_{T})/Gen p_{T} respectively where Reco p_{T} is the reconstructed jet p_{T} in the detector and Gen p_{T} is the generated jet p_{T} in the simulation. The discrepancy between generated and reconstructed jet transverse momentum is decreased for particle flow jets especially at low-p_{T}. This is because the resolution of the tracker is much better than of the calorimeters at

low-p_{T}. For the high-p_{T} jets the opposite is true and the performance of particle flow and calorimeter jets is comparable in this region.

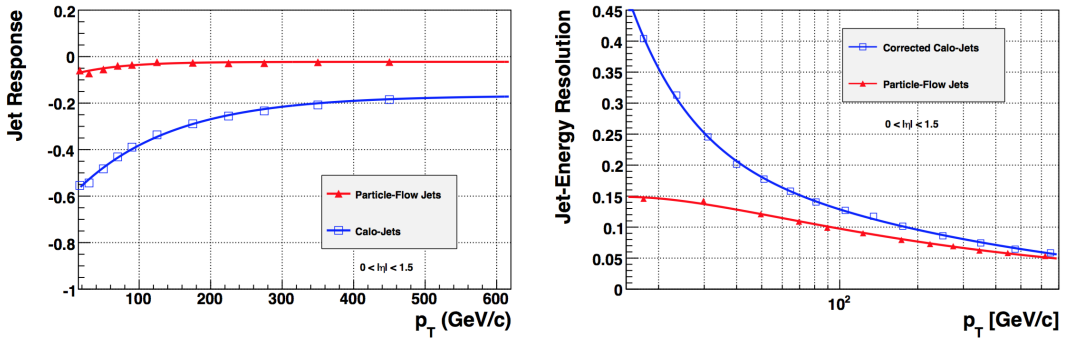

Figure 3.14: Jet response (left) and resolution (right) for Calorimeter jets and Particle Flow jets [30].

As it was mentioned in Sec. 1.2.3, gluon jets have larger multiplicity and softer constituents than quark jets. The nonlinearity of calorimeter response therefore results in a difference in response between quark and gluon jets. Figure 3.15 shows that this effect is also reduced with particle flow jet reconstruction [31].

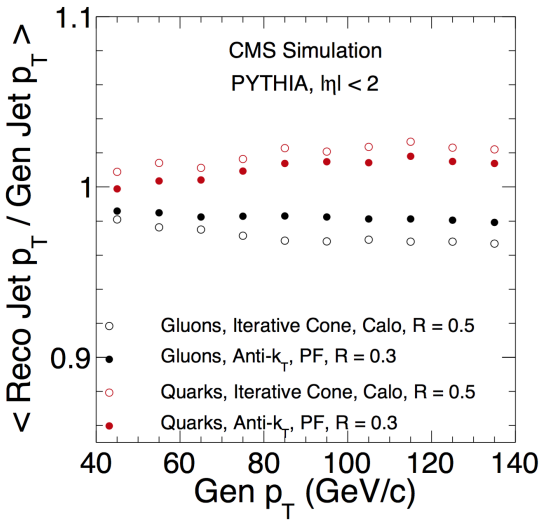

Figure 3.15: Jet response of quarks and gluons for calorimeter and particle flow jets [31].

In this analysis anti-k$_T$ jets constructed from particle flow object with a radius parameter of R=0.4 are used.

3.2.2 Underlying event subtraction

The jet reconstruction in heavy-ion collisions is particularly challenging because of the huge background from the underlying event (see Fig. 3.16 for comparison), which mostly consists of soft particles and should be removed from the jet definition.

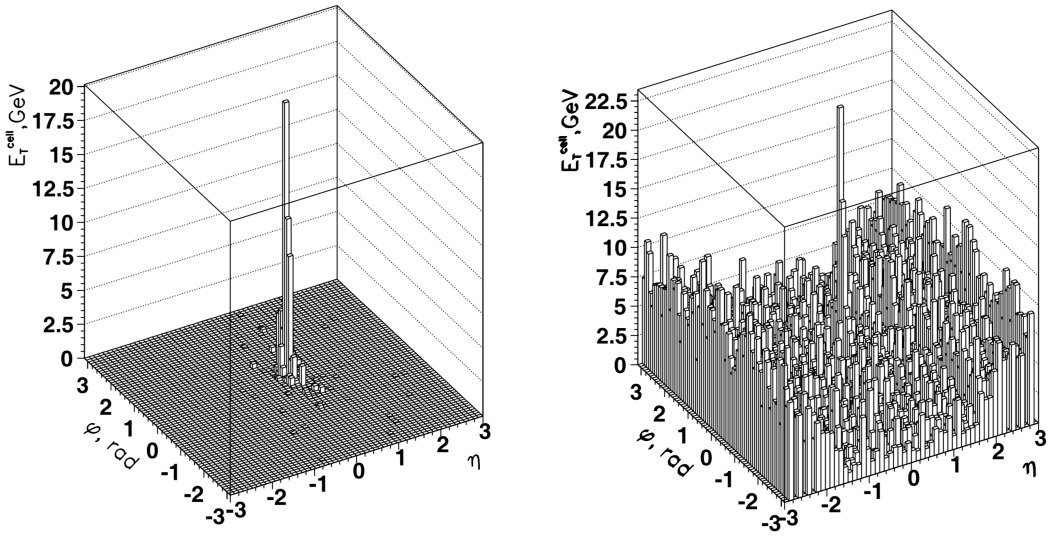

Figure 3.16: A 100 GeV jet without and with PbPb background [32].

There are several techniques to subtract the underlying event in heavy-ion collisions [132, 133]. This analysis makes use of an iterative "noise/pedestal subtraction" technique [32]. As one can see from Fig. 3.16, the underlying event density is uniform in ϕ and non-uniform in η. Therefore the background estimation is done in strips of η and proceeds as follows:

- calculate the mean value $\langle E \rangle$ and RMS σ in the each η strip and subtract $\langle E \rangle + \sigma$ from each cell. If the energy in the cell after the subtraction is negative, then it is set to zero.
- reconstruct jets using anti-k$_T$ algorithm
- calculate and subtract $\langle E \rangle + \sigma$ in each η strip excluding calorimeter cells outside the area covered by jets with $p_{\mathrm{T}} > 20$ GeV
- reconstruct jets again

The subtraction of $\langle E \rangle + \sigma$ (as opposite to subtracting only $\langle E \rangle$) is necessary to compensate the positive bias of setting negative cell energies to zero. The subtracted energy per η tower varies between 1 GeV/tower in central and 10 GeV/tower in forward rapidity regions (Fig. 3.17, left). The performance of the subtraction method is tested by comparing the reconstructed and generated jet energies in the sample with and without underlying event background (Fig. 3.17, right).

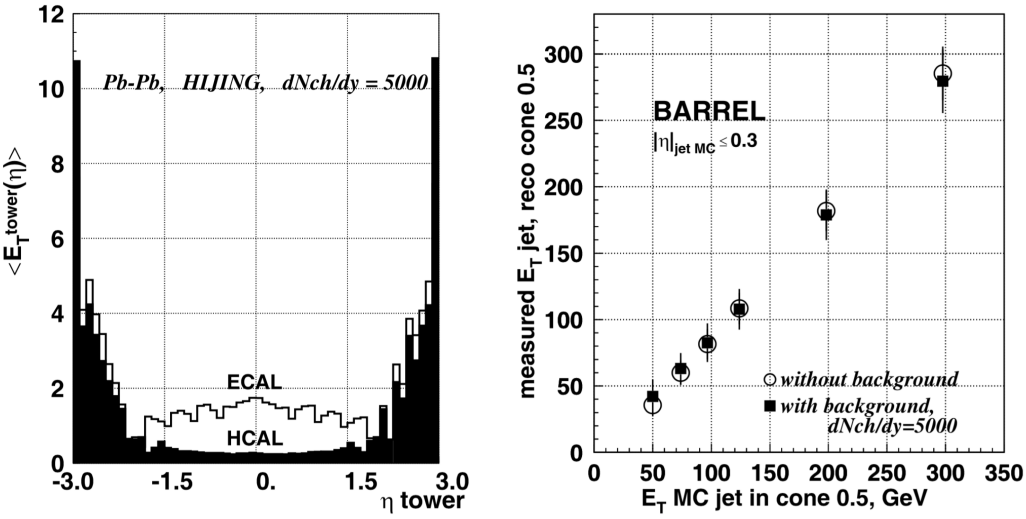

Figure 3.17: Average subtracted energy in η towers (left), correlation between generated and reconstructed jet energy in sample without background and with background (right) [32]

In the current analysis, however, this procedure failed in a particular case. While this algorithm performed well for the data of $\sqrt{s} = 2.76$ TeV, in the last $\sqrt{s} = 5$ TeV run the occupancy in the endcaps (where the granularity is the lowest) was so high that the all towers in a given η-ring can be excluded. As a result, all the jets in the ring are considered to be "good" jets, and the background is not subtracted. In order to fix this behavior, a new parameter was introduced: the maximum fraction of towers in a given η-ring allowed for exclusion. This forces algorithm to subtract at least some towers even if the full η-ring seems to be made of jets.

The underlying event subtraction is an essential part of jet reconstruction in heavy ion collisions, but it also induces the difference between jet energy scale in the pp and PbPb collisions, an effect which has to be corrected for.

3.2.3 Jet energy corrections

Detector effects introduce a difference between the generator-level and reconstructed jets. In order to mitigate these effects, the appropriate corrections to the jet energy must be applied. The corrections are constructed from the jet energy scale, i.e. the mean of the ratio of the reconstructed jet p_{T} to generated jet p_{T}, by scaling the reconstructed p_{T} so that the energy scale is unity.

This is done in CMS as follows:

- **L1(PU)** corrections. In pp collisions they correct an average energy offset due to pile-up and the underlying event. In PbPb collisions the UE subtraction is part of the jet reconstruction and L1 corrections are not applied.
- **L2L3**(η, p_{T}) corrections. The non-flatness of jet response in η and p_{T} is corrected from simulation.
- **residual L2L3** corrections for the data-simulation difference: dijet, photon-jet and Z-jet balance are used [134]. The reference object (photon or Z) is used to to establish the absolute energy scale while the balance of dijets is used for the relative energy scale as a function of pseudorapidity.

In PbPb collisions, L2L3 corrections derived from pp simulation are applied. In underlying event subtraction procedure in PbPb collisions (Sec. 3.2.2) introduces an additional bias which has to be corrected for.

The artifacts of the UE subtraction in PbPb collisions are: the over-subtraction of low-p_{T} jets (in the case, the jet is confused with background) and under-subtraction of high-p_{T} jets (in the case of too high occupancy in the detector).

The over-subtraction can be studied in peripheral events, where background levels are low. In this regime the non-closure is because background subtraction removes low-p_{T} jets considering they are background. Indeed as it may be seen in Fig. 3.18, this effect is biggest at $p_{\mathrm{T}} < 100$ GeV. It can be parametrized as

$$\left\langle \frac{p_T^{reco}}{p_T^{gen}} \right\rangle_{over} = 1 - c_1 e^{-c_2 p_T} \tag{3.1}$$

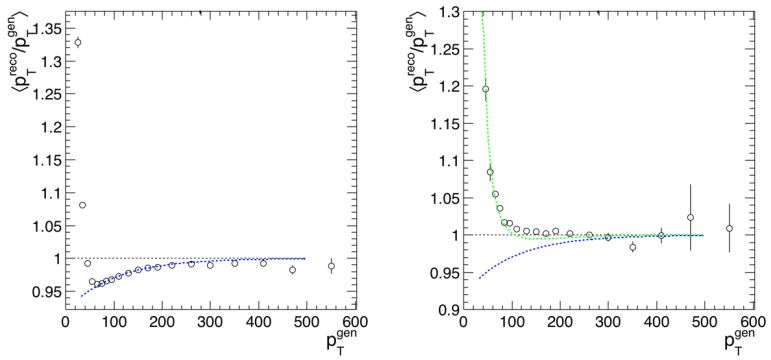

Figure 3.18: Jet energy scale in 70-100% (left) and in 0-5% (right) events without UE corrections.

The parameters c_1 and c_2 are determined from peripheral collisions and fixed because this effect is believed to be independent on the centrality. The under-subtraction of jets happens because of the limitation of the algorithm: when too many towers look like jets we restrict the maximum fraction of towers for exclusion and therefore some background is left in the jet energy. This will make reconstructed jet p_{T} higher than generated and happens in the most dense environment, i.e. most central collisions, as it can be seen from Fig. 3.18. This contribution is parametrized as

$$\left\langle \frac{p_T^{reco}}{p_T^{gen}} \right\rangle_{under} = \frac{c_3}{(p_T - 15GeV)^2} \tag{3.2}$$

and c_3 is a single parameter dependent on the collision centrality. After these corrections are applied, the reconstructed p_{T} is within 1% close to the generated jet p_{T} as can be seen in Fig. 3.19. The "safety zone" on the figure denotes the jets that enter the analysis ($p_{\mathrm{T}}^{reco} > 40$ GeV), below which we do not apply the corrections.

3.2.4 Jet energy resolution

While jet energy corrections correct the mean p_{T} of the reconstructed jet to that of the generated jet, random fluctuations are still present. The resolution is the deviation of the reconstructed jet p_{T} from the mean as a function of generated jet p_{T} and more exactly defined as $\sigma(p_T^{reco}/p_T^{gen})/\mu(p_T^{reco}/p_T^{gen})$. The effect of a non-zero resolution on the measurement can be described by adding a Gaussian noise.

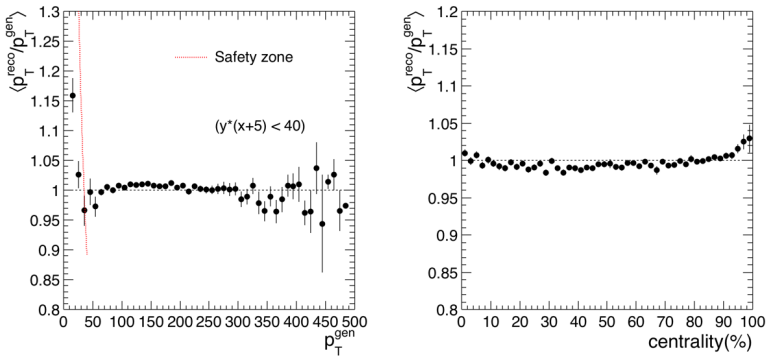

Figure 3.19: Jet energy scale after the UE corrections, as a function of p_{T} in 0-5% events and as a function of centrality.

For a quantity with an approximately flat spectrum, the resolution only blurs the spectrum reducing the sensitivity of the experiment. For quantities with a falling spectrum, however, (e.g., jet p_{T}) the resolution plays a crucial role. Given the same probability of acquiring a positive and negative Δp_{T} value, in a falling distribution many more jets will increase their p_{T} than decrease, which is effectively a one-side shift of the spectrum. Therefore the resolution plays an important role in the result interpretation.

In general, detector resolution can be described with three factors [135]:

- **stochastic factor**. The probabilistic character of the decay inside the detector leaves the Poissonian error on the number of the detector submodules and therefore on the final jet energy: $\sigma(p_T) \sim S\sqrt{p_T}$ This is the dominant uncertainty for calorimeters since the particle is supposed to fully decay and the total energy is derived from number of calorimeter cells involved

- **noise factor**. Every detector has intrinsic noise which contribute to the final jet energy: $\sigma(p_T) \sim N$ This term is very useful in describing the impact of random fluctuations of the underlying event to the jet resolution.

- **constant factor**. The finite size of the calorimeter leads to the shower leakage, which additionally increases the resolution. As a result, the constant factor C is present. At low p_{T} because of the multiple Coulomb scatterings on the tracker layers, the track undergoes the deviation from its direction almost independent on the track momentum. Therefore this is the dominant factor for the track momentum measurement at low p_{T}.

Although different factors are dominant in different detectors, all of them must be taken into account. Assuming them uncorrelated, three sources of uncertainly can be combined together as:

$$\frac{\sigma(p_T^{reco})}{\langle p_T^{reco} \rangle} = \sqrt{\frac{S^2}{p_T} + \frac{N^2}{p_T^2} + C^2} \tag{3.3}$$

The C and S terms are properties of the detector itself, and should therefore be centrality independent to first approximation. The N parameter incorporates the effect of the underlying event and should therefore be centrality dependent. Assuming $N = 0$ for pp and peripheral collisions one obtains a good fit for the C and S parameters. Then their values were fixed and the N parameter was fit as a function of centrality which shows linear behavior (Fig.. 3.20, left). The final fitting functions for different centralities are shown on the Fig. 3.20.

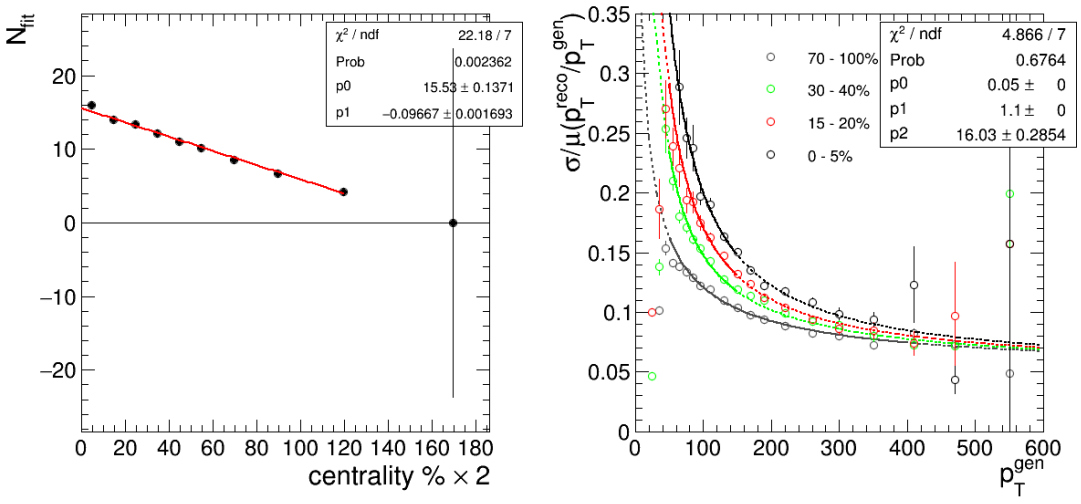

Figure 3.20: N terms in various centrality bins (left) and the final jet resolution in PbPb (right).

collision	C	S [GeV$^{1/2}$]	N [GeV]
pp	0.06	0.8	0
PbPb	0.06	1.0	16-0.05*%

Table 3.1: Resolution parameters, % sign stands for centrality percentile.

Resolution parameters for the jets used in this analysis are shown in Table 3.1. The small difference in C and S terms between pp and PbPb collisions is caused by the differences in reconstruction, while N term changes linearly with centrality from 0 in peripheral to 16 GeV in central collisions. This has a very simple

interpretation: adding additional noise of 16 GeV to each jet in pp data one can obtain the reference in central collisions for the phenomena under investigation. This procedure is called *smearing* and is used in this analysis as a comparison baseline. Although simulation is often used throughout the analysis, the final results feature pp smeared data as a reference.

3.3 Tagging of b-jets

One of the most important properties for the identification of b-hadrons is their relatively long lifetime. For example, the mean lifetime of the $B^{\pm}$ is 1.72±0.1 ps in its rest frame [55]. Given its mass of 5280 MeV, at a momentum of 100 GeV this corresponds to a Lorentz factor of $\gamma = 19$. Particles decay with the survival probability $P(t) = e^{-t/\gamma\tau}$, which translates into an average lifetime of $\langle t \rangle = \int_0^\infty tP(t)dt = \gamma\tau$ ~28.5 ps in the lab frame. With a speed $v = p/(\gamma m) \approx 0.998c$, on average the particle will fly 8.5mm before it decays, a displacement large enough to be detected with a silicon tracker.

A typical b-hadron decay chain is shown in Fig. 3.21. In this case, a first b-hadron decay, $B^+ \to \overline{D}^0 \mu^+ \nu_\mu$ is followed by the c-hadron decay $\overline{D}^0 \to K^+ \mu^- \overline{\nu}_\mu$. To reconstruct a displaced vertex in a silicon tracker, the decay should have at least two long-lived charged particles. In this case, it is actually the *tertiary* vertex corresponding to the c-hadron decay that is likely to be reconstructed. In the CMS terminology, however, all reconstructed vertices are referred to as secondary vertices, and we follow this convention.

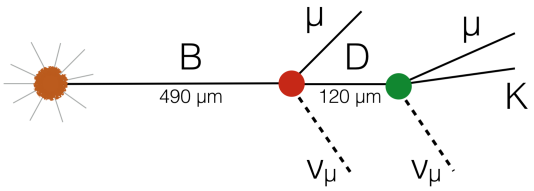

Figure 3.21: B-hadron decay into D-meson with subsequent decay.

Even in the case when the vertex is not reconstructed, the impact parameter of tracks has discriminative power. Figure 3.22 shows a 3D impact parameter significance (i.e. the value divided by the estimated error) in pp collisions for 3 types of jets: b-jets, c-jets and light jets. The significance is used to mitigate the effect of the track parameters resolution which is dependent on p_{T} and η. This variable has the same sign as the scalar product of vector pointing from the primary vertex to the point of closest approach of track and jet direction. For the tracks from subsequent decays along the jet axis, 3D IP will tend to have positive

values, while tracks from the primary vertex can have both positive and negative values. One can see from the figure that tracks with a large impact parameter are coming mostly from b-jets as expected from the large lifetime of b-hadrons.

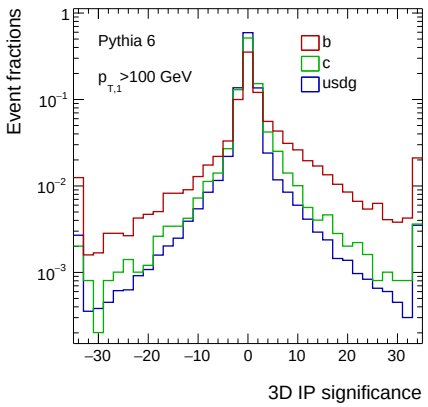

Figure 3.22: 3D Impact parameter significance of the tracks inside the jet for b, c and light jets in pp collisions.

The reconstruction of secondary vertices is performed using the Adaptive Vertex Reconstruction (AVR) algorithm [136] based on the adaptive vertex fitter[137]. Only the tracks with p_{T} above 1 GeV and transverse impact parameter smaller than 2mm inside a jet are considered by the vertex fit. In order to decrease the contribution of vertices not originating from a b-hadron decay, the following constraints are applied. The vertex is rejected if it shares more than 65% of tracks with the primary vertex. The 2d flight distance significance (value of distance between primary and secondary vertices in transverse plane divided by its uncertainty) should be larger than 3. The vertex belongs to a jet if the angular distance $\Delta R = \sqrt{\Delta\phi^2 + \Delta\eta^2} < 0.4$.

Figure 3.23 shows the number of the secondary vertices inside the jet for pp and PbPb collisions. The presence of a secondary vertex increases the chances of jet to be a b-tagged jet.

The properties of secondary vertices allow further discrimination. Figure 3.23 shows secondary vertex flight distance significance and secondary vertex mass for different jet flavors. The Simple Secondary Vertex (SSV) discriminator uses only the flight distance significance variable. There are two versions of this tagger: High

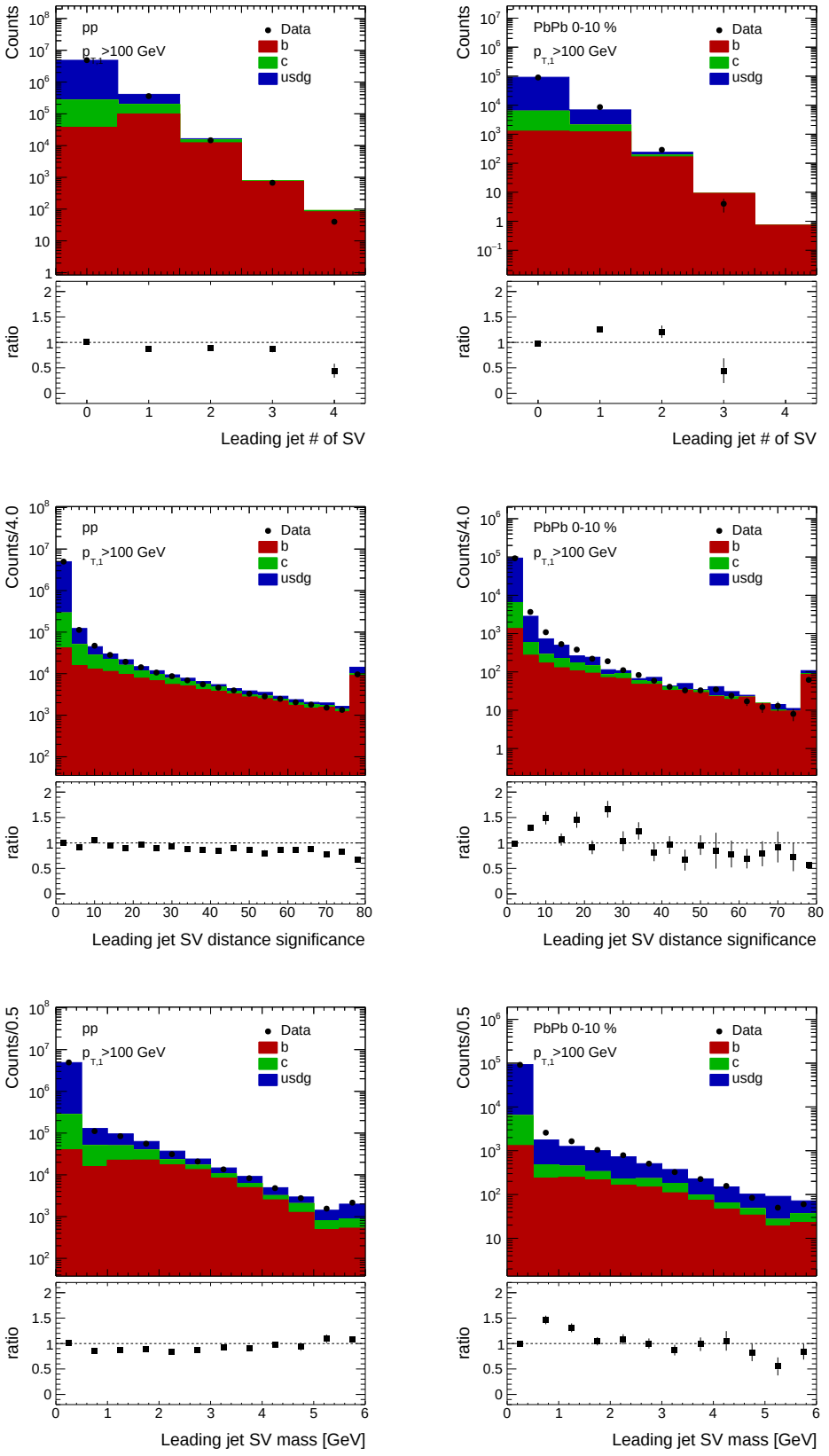

Figure 3.23: Properties of secondary vertices: Number of secondary vertices in the vicinity of jet axis, flight distance significance and secondary vertex mass for different jet types in pp and central PbPb collisions.

Efficiency (SSVHE) requires that secondary vertex contains at least two tracks, while High Purity (SSVHP) requires at least three associated tracks. The SSV discriminator was used in previous heavy ions results [86, 22].

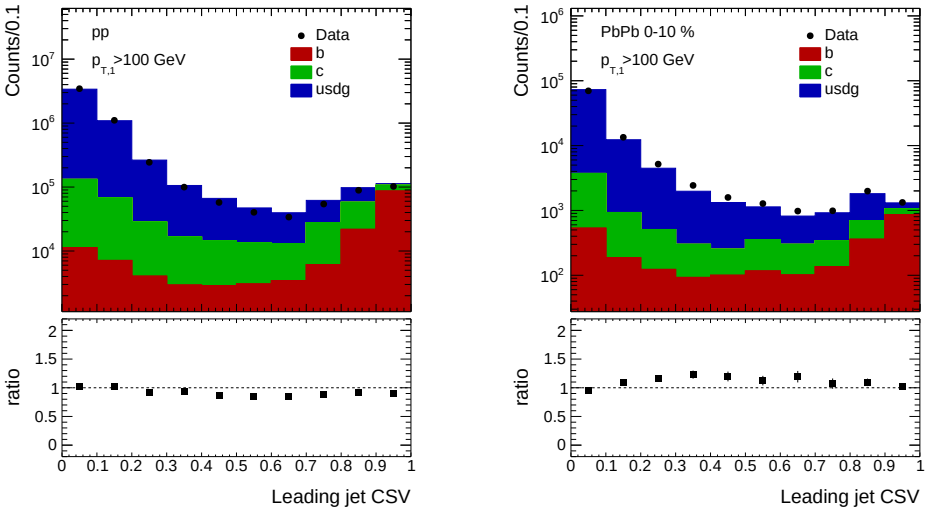

Figure 3.24: Combined secondary vertex discriminator distributions for different jet types in pp and central PbPb collisions.

In the case when the secondary vertex cannot be reconstructed but the jet has several tracks with large positive impact parameter significance, one can combine them in the *pseudo-vertex*. An example of such a vertex might be a 1-prong decay of B-meson at the secondary vertex and a 2-prong subsequent D-meson decay as shown on Fig. 3.21 with one of the tracks being misreconstructed. Because the vertex fit is not performed, the vertex flight distance significance is not used for this category, but other variables like vertex mass, track multiplicity, etc. make sense and provide additional separation between jet flavors.

In order to combine multiple variables, the total likelihood is defined as

$$\mathcal{L}^{b,c,q} = f^{b,c,q}(\alpha) \prod_i f_\alpha^{b,c,q}(x_i) \tag{3.4}$$

where α denotes vertex type (no vertex, pseudo-vertex, secondary vertex), b,c,q stand for b-jets, c-jets and light jets respectively and $f_\alpha^{b,c,q}(x_i)$ denote probability distributions of different variables for different vertex type corresponding to b, c or light jets.

The variables used are

- 2d vertex flight distance significance in the transverse plane
- vertex mass
- number of tracks at the vertex
- ratio of the energy carried by tracks at the vertex with respect to all tracks in the jet
- pseudorapidities of the tracks at the vertex with respect to the jet axis
- 2D impact parameter significance of the first track that raises the invariant mass above the charm threshold of 1.5 GeV/c^2 (tracks are ordered by decreasing IP significance and the mass of the system is recalculated after adding each track)
- number of tracks in the jet
- 3D IP significances for each track in the jet

In general, the good agreement between the simulation and data as well as the similarity of distributions of the input variables between pp and central PbPb collision (Fig. 3.22,3.23,3.24) demonstrate the robustness of the b-tagging discriminator under different conditions.

The distributions of c-jet properties are usually different from those of light jets hence c-jets are considered as a separate background. The a priori probabilities of c and light jets are set to $f_c = 0.25$ and $f_q = 0.75$ respectively. Three likelihoods are blended into the single variable called *Combined Secondary Vertex (CSV) discriminator* (see [138]) using likelihood ratios:

$$CSV = f_c \frac{\mathcal{L}^b}{\mathcal{L}^b + \mathcal{L}^c} + f_q \frac{\mathcal{L}^b}{\mathcal{L}^b + \mathcal{L}^q} \tag{3.5}$$

Figure 3.24(left) shows comparison of the combined vertex discriminator in pp and central PbPb collisions for different jet flavors. In order to tag a jet one has to

define the working point of the tagger, in the case of CSV it must be between 0 and 1. All the jets which have the discriminator value above this point are considered b-jets (*tagged*). It is clear that for any point there is a probability of a b-jet to have low discriminator value and of c- or light jet to have a large value. Therefore one has to define the efficiency and purity as a function of working point. The efficiency is the fraction of tagged b-jets (with discriminator above threshold) out of all b-jets in the event (with any discriminator value). The purity is the fraction of b-jets in the selected sample of jets with the discriminator above the threshold. Given these two values for each working point, one can compare taggers of different nature on the ROC-curve: the curve created by connecting purity-efficiency pairs for different working points. The examples of ROC-curves for different taggers are presented on Fig. 3.25.

The CSV discriminator is only a single example of the variety of taggers available. In the form described above it was used in the Run 1 of proton-proton collisions at CMS [33]. Other taggers also exist, for example Jet Probability (JP) tagger uses only information from tracks impact parameter inside the jet, SSV tagger was introduced above. Figure 3.25 (left) compares the performance of different taggers used in Run 1. One can see that combining different variables in CSV discriminator gives at least 10% of efficiency increase for equal misidentification probability with respect to the SSV tagger. Also SSV has a limit in the efficiency because in $\sim$30% of cases the secondary vertex cannot be reconstructed.

The secondary vertex is not the only sign of b-jet in the event. The Soft Muon and Soft Electron algorithms search for a muon or an electron within the jet cone. The more advanced discriminators, such as cMVAv2, use multi-variate techniques to combine different taggers into a single most discriminative variable. A comparison of CSV with other discriminators is shown on Fig. 3.25 (right) [34].

For the analysis described in the section 4.4, a tight working point of $CSV > 0.9$ has been chosen. For this study one has to tag two jets in the event: the leading and subleading jet. The performance of the discriminator for doubly-tagged b-jet events is shown in Fig. 3.26. The efficiency and purity of the b-tagging are shown for different selections of working point of the CSV discriminator value.

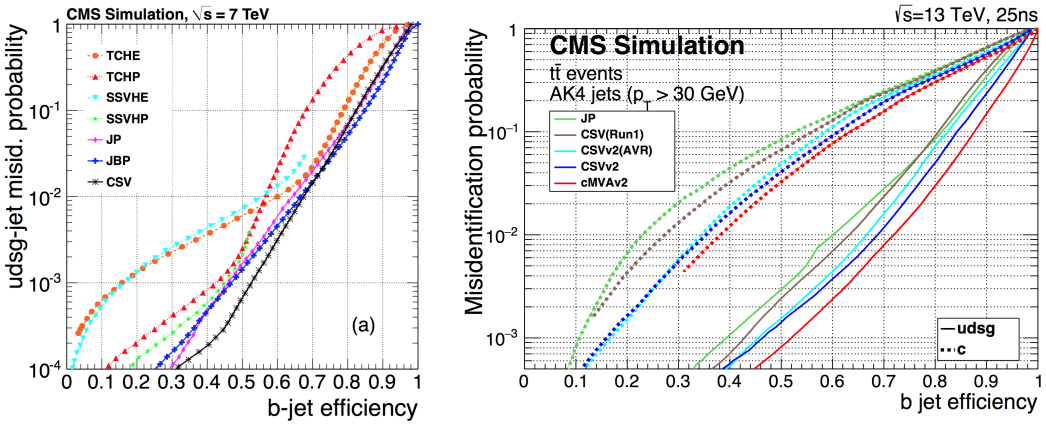

Figure 3.25: b-taggers used in CSM Run 1 (left) and Run 2 (right) [33, 34]

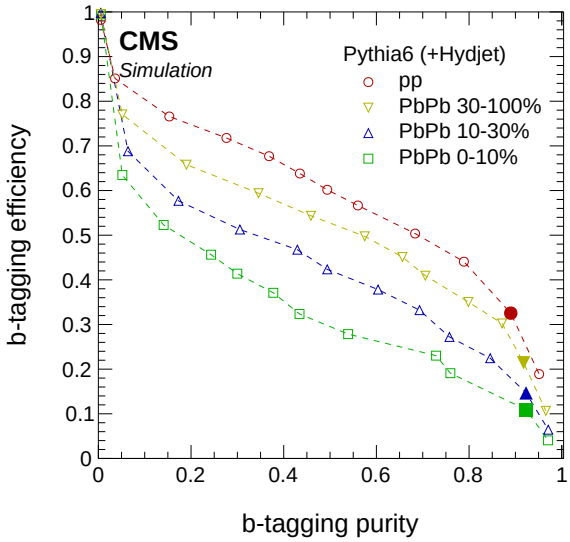

Figure 3.26: Performance of the b-tagging discriminator (ROC curve) for doubly-tagged b-jets in pp and PbPb collisions with different centrality. The filled markers represent the chosen working point (CSV $>$ 0.9).

In general, the large multiplicity of heavy-ion events results in the increase of combinatorial fake vertices and as a result in the degradation of the b-tagging performance. The working points are chosen so that the purity is around 90% for all types of collisions, but the efficiency drops from $\sim 35\%$ in pp collisions to $\sim 10\%$ in central PbPb collisions. However, the overall efficiency value does not have to be corrected for because this analysis uses only self-normalized quantities such as ratio of subleading to leading jet transverse momentum. On the other hand, the dependence of efficiency on variables that enter the analysis (such as centrality, p_{T} and η) is corrected for as will be discussed in Sec. 4.3.

Transverse momentum balance of b-jet pairs

4.1 Inclusive jet trigger

As was mentioned in Section 2.2.5, the data acquisition system is unable to record every event registered in the detector and a multilevel triggering system is employed to reduce the data volume. If the triggers are designed carefully, this does not worsen the quality of the measurement. The differential cross section of jets (and in general most physical observables) as a function of energy or momentum spans multiple orders of magnitude. Jets with high energy only appear in a small fraction of events, which are possible to record completely. On the other hand, low-energy jets are much more frequent, and one needs only a fraction of them to obtain a good statistical precision.

Various jet triggers were implemented that differ by predefined jet energy thresholds. Figure 4.1 shows the effect of "turn-on" of PbPb triggers of various thresholds at the L1 and HLT levels which are described in Section 2.2.5. If the jet p_{T} at the trigger level was equal to the final reconstructed value, then the trigger efficiency curve would be a step function.

The offline reconstruction uses the full information from the detector to construct particle flow objects and then to cluster jets from them. At the HLT level only the calorimeters are used to reconstruct jets, therefore the HLT efficiency has a turn-on effect with respect to the offline jets, as shown in Fig. 4.1, right. The L1 trigger has a coarse calorimeter resolution as well as simpler background subtraction algorithms [95] compared to HLT and offline, therefore its efficiency curve

rises even slower (Fig. 4.1, left). For example, at 50 GeV the L1 trigger with a 28 GeV threshold (denoted on the figure as L1 SingleJet 28) is fully efficient, while L1 trigger with 56 GeV threshold is very inefficient. HLT triggers take L1 triggers as input. For example, the HLT trigger with 80 GeV threshold runs only if the L1 trigger with 44 GeV threshold is fired. The thresholds of L1 triggers are therefore lower than that of the corresponding HLT triggers, such that the L1 trigger is fully efficient at the given HLT threshold. The total L1×HLT efficiency is shown on Fig. 4.1 (right).

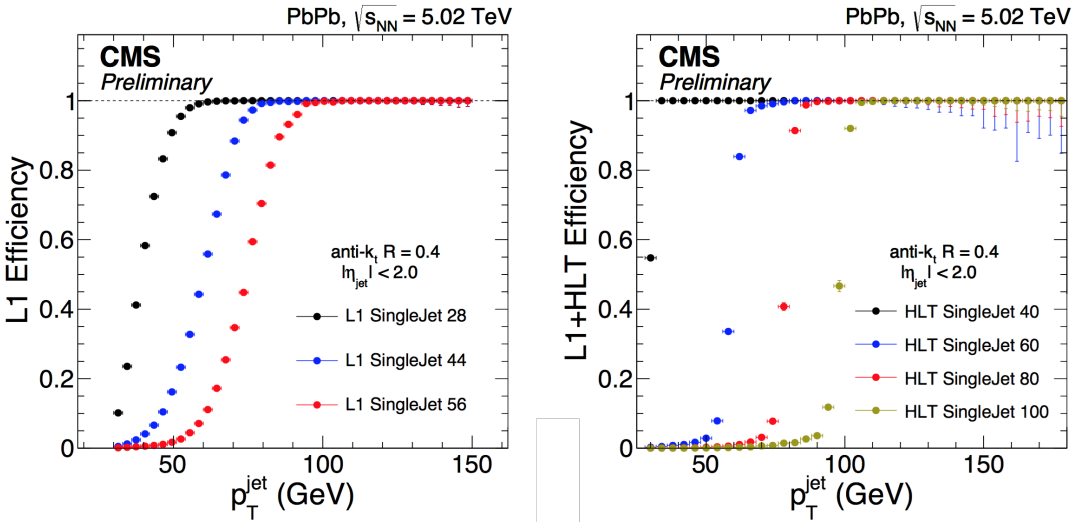

Figure 4.1: The efficiency of L1 triggers with 28, 44 and 56 GeV thresholds (left) and HLT triggers with 40, 60, 80 and 100 GeV thresholds (right) as a function of offline reconstructed jet p_{T} in PbPb collisions during the 2015 data taking period [35]

Although the frequency of low-energy and high-energy events differs by orders of magnitude, for the purpose of the analysis one needs an approximately equal amount of events for the full energy range. One then defines different trigger prescales: the probability to keep an event when a trigger fires. In this case the amount of low-p_{T} and high-p_{T} jets recorded is similar, but the total jet spectrum can be reconstructed by applying the inverse of the average prescale factor as an event-level weight. Prescale values typically change during the data taking, even within a single run. However, the "overlaps" of the triggers can be used to deduce the average prescale factors. For example, in the 2015 PbPb data taking, the trigger HLT trigger with 100 GeV threshold was not prescaled (neither at L1 nor HLT), i.e., every event which fired this trigger was recorded. If the 80 GeV trigger was not prescaled, then it would have fired on the same events too as it has a

lower threshold. The average prescale is therefore the fraction of events for which both triggers fired, i.e.,

$$\omega_{80} = \frac{\#\text{ of events with Jet80 AND Jet100}}{\#\text{ of events with Jet100}}, \tag{4.1}$$

and other prescales are defined similarly.

In total, during the full data taking there were 2.4 million events of Jet100 recorded. If there had been no prescale, Jet80 would have recorded 6.9 million events, and Jet60 would have recorded 39 million events which exceeds the available resource constraints. With average prescales of 2.7 and 11.6 respectively, the Jet80 trigger recorded 2.6 million events and Jet60 recorded 3.3 million events.

There are several techniques to unprescale triggers, i.e. to reconstruct the unbiased jet spectrum from the prescaled events. The simplest approach is applying to the event the inverse prescale weight corresponding to the highest threshold trigger that fired in the event. In the case of the 2015 PbPb data this corresponds to the following algorithm:

if Jet100 fired	AND	jet $p_{\mathrm{T}} > 100$	use $1/\omega_{100}$
if Jet80 fired	AND	jet $80 < p_{\mathrm{T}} < 100$	use $1/\omega_{80}$
if Jet60 fired	AND	jet $60 < p_{\mathrm{T}} < 80$	use $1/\omega_{60}$

where jet p_{T} corresponds the highest p_{T} jet reconstructed at HLT (the one used in the HLT decision). We note that this algorithm does not use all available events. For example, an event with an HLT jet of 90 GeV which does not fire the HLT Jet80 trigger (due to prescaling), but does fire the HLT Jet60 trigger, would be dropped from the analysis. While such events could be recovered with more complicated trigger combination rules, the impact of such events was very small, so this was not pursued.

After the proper trigger combination, the jet spectrum must be smooth across the full range. The p_{T} of the jet after the full reconstruction is slightly different from the trigger jet p_{T} because full reconstruction is not available at HLT. The merged spectrum of trigger and offline jet p_{T} and contributions from different triggers are shown on Fig. 4.2. The left panel shows the combined spectrum as a function of the online (HLT) jet p_{T} after the merging procedure has been applied. The right

panel shows the shows same events, but plotted as function of the offline jet p_{T}.

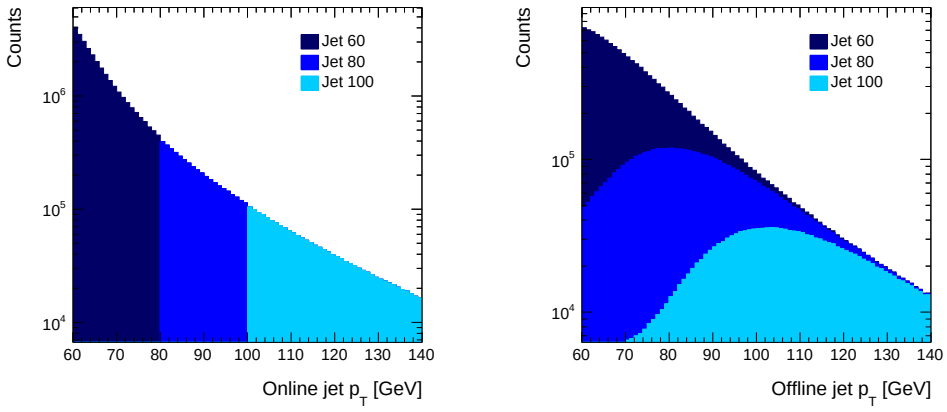

Figure 4.2: Merged jet spectrum as a function of online reconstructed (HLT) jet p_{T} (left) and offline reconstructed jet p_{T} (right) in PbPb collisions. Different colors correspond to the events added by the corresponding trigger.

4.2 b-jet trigger

The rate of b-jets is naturally reduced compared to inclusive jets, as the b-jet fraction is quite small, on the order of 3% as shown in Fig. 4.3. Given data volume and throughput constraints, it would therefore be advantageous to construct a trigger that specifically targets b-jets, provided this could be achieved with reasonably high efficiency and purity.

The b-jet triggers employed in this analysis are constructed as follows. If the calorimeter jet trigger of a certain threshold fires, then all jets above threshold are considered for b-tagging. Since b-tagging relies on the properties of tracks, a fast version of the track and vertex reconstruction was performed online, i.e. directly at the HLT during the data-taking process. Due to the timing constraints the full tracking was not performed, but only the tracks and secondary vertices nearby each jet above the energy threshold of the calorimeter jet trigger were reconstructed. Then the CSV discriminator is calculated for those jets to determine whether any b-jets are present in the event. The working point of CSV>0.7 was chosen which is looser than offline cut (CSV>0.9) in order to compensate for the difference between online and offline reconstructions. Figure 4.4 illustrates the hierarchy of

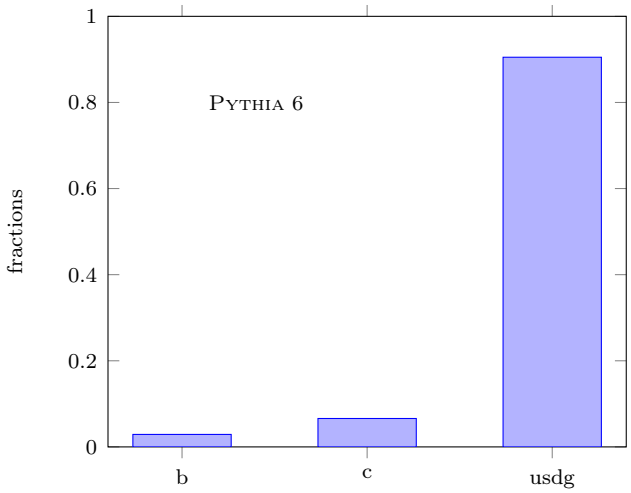

Figure 4.3: Frequency of parton flavors for jets with $p_{\mathrm{T}} > 100$ GeV in Pythia 6 QCD events at $\sqrt{s} = 5.02$ TeV.

inclusive jet and b-jet 80 GeV trigger.

The performance of the b-tagging at HLT was investigated in embedded PbPb samples with a hard scattering of $\hat{p}_{\mathrm{T}} > 50$ GeV. A signal enriched sample is obtained by requiring the presence of the b-quark within the acceptance. The fraction of events firing the b-jet trigger out of events firing the inclusive jet trigger of the same threshold are compared in this b-quark filtered sample with standard QCD events. Figure 4.5 shows this ratio for the 60 GeV threshold triggers, as a function of PbPb collision centrality. This ratio in the b-jet poor (QCD) and enriched (b-filtered) samples is a good proxy for the trigger efficiency and fake rate. One should keep in mind however that in QCD sample there is a $\sim 3\%$ fraction of jets originating from b-quark, therefore accept rate in QCD sample must not be zero even for the ideal trigger. On the other hand, b-quark filtered sample may have b-jets of low-p_{T}, which are below trigger jet p_{T} threshold and the trigger will not fire on such event. Also the event may not have exactly one b-jet: the b-jet can be outside of the acceptance as well as multiple b-jets might be present. The b-jet trigger delivers a 10 times rejection in a QCD sample while keeping the majority of events with b-jets. The performance in central collisions is worse because the high multiplicity of central collisions gives rise to fake combinatorial vertices which degrade the performance of b-tagging.

Two b-jet triggers were used during 2015 data taking period: with 80 GeV and

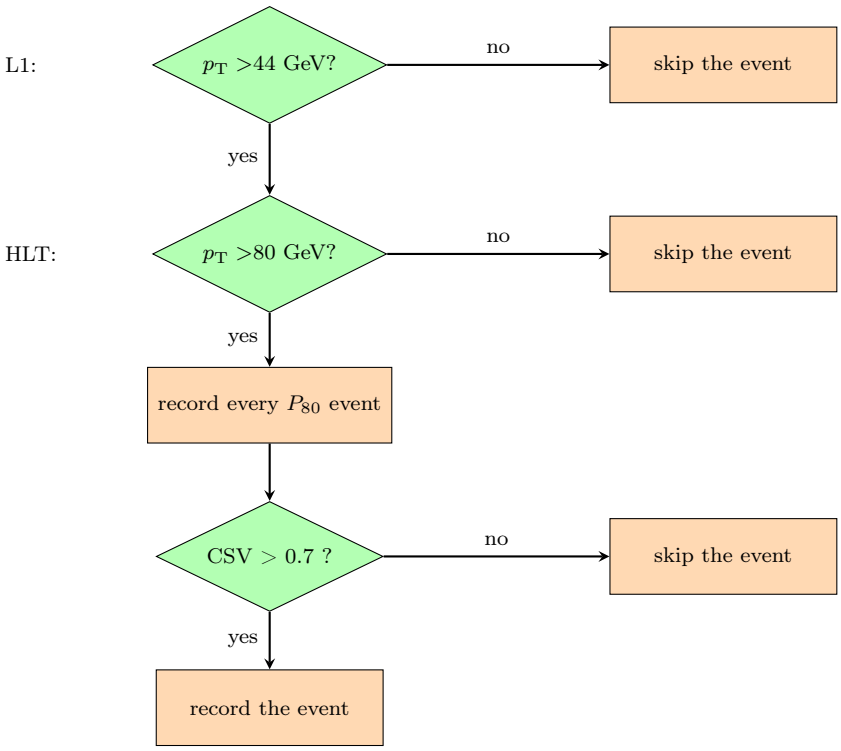

Figure 4.4: The trigger hierarchy for inclusive jet and b-jet 80 GeV triggers. P_{80} is equal to the instantaneous prescale of the inclusive jet 80 GeV trigger with average $\langle P_{80} \rangle = 2.7$.

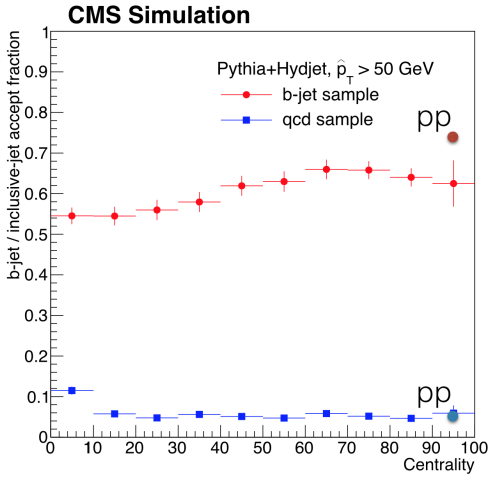

Figure 4.5: Accept rate of b-jet trigger with 60 GeV threshold in QCD and b-quark filtered sample as a function of collision centrality.

60 GeV thresholds. As it was mentioned above, the 80 GeV inclusive jet trigger had an average prescale 2.7. Because the rate of b-jet trigger is a factor of 10 lower than for the inclusive jet trigger, b-jet trigger with 80 GeV threshold was run unprescaled and b-jet 60 GeV trigger had a prescale of only 1.6. The merged spectrum of b-jet triggers is shown on Fig. 4.6.

After taking into account the efficiency of online tagging, the b-jet trigger allowed

us to record more than twice the number of events than the inclusive jet trigger.

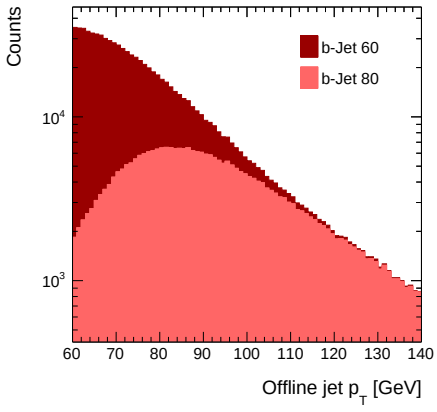

Figure 4.6: Merged b-jet spectrum as a function of offline reconstructed jet p_{T} (right). Different colors correspond to the events added by the corresponding trigger.

During the pp reference run, we were able to run the inclusive jet 80 GeV trigger unprescaled. As a consequence, the dedicated b-jet trigger was not used in this analysis. Table 4.1 summarizes inclusive jet and b-jet trigger prescales and total number of events recorded.

trigger name	average prescale	# of events
PbPb Jet100	1	2.4M
PbPb Jet80	2.7	2.6M
PbPb Jet60	11.6	3.3M
PbPb bJet80	1	544K
PbPb bJet60	1.6	2M
pp Jet80	1	16M
pp Jet60	6.2	9M

Table 4.1: Summary table of inclusive jet and b-jet triggers used in 2015 data taking.

The b-jet trigger fires if any jet in the event above specified threshold is tagged. As a consequence it may fire on the subleading jet. The subleading jet threshold is above 40 GeV in this analysis, but neither 60 nor 80 GeV trigger are fully efficient at 40 GeV. This means that events with high-p_{T} subleading jets will enter the analysis, while events with low-p_{T} will not, which introduces a bias in the measurement. Triggering on the leading jet, on the other hand, is safe as long as the lowest jet trigger is fully efficient at leading jet p_{T} cut (100 GeV) which is the case. The contribution of events where the trigger did not fire on the leading jet

(but fired on other jet in the event) can be removed by matching the triggered jet with offline reconstructed leading jet. Figure 4.7 shows the azimuthal and polar correlations between the offline leading b-tagged jet and the closest trigger jet. In most cases they are close to each other in $\Delta\phi \times \Delta\eta$ space. In rare cases however, they are opposite in $\Delta\phi$ which indicates triggering on the subleading jet. In order to get rid of those events, an elliptic matching criterion in $\Delta R = \sqrt{\Delta\phi^2 + \Delta\eta^2}$ (represented as a line on Fig. 4.7, right) is applied which removes less than 2% of the data.

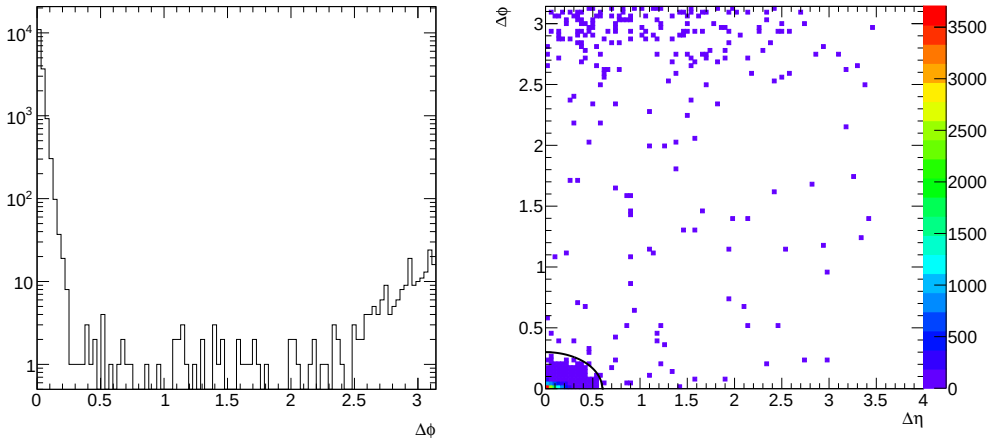

Figure 4.7: $\Delta\phi$ (left) and ΔR between offline b-tagged jets and the closest HLT jet. The selection applied as a matching criteria is shown as a line.

Due to differences in the online and offline tracking the trigger is not fully efficient with respect to the offline tagging. As is the case with the offline tagging efficiency, the analysis is not sensitive to the absolute efficiency, but the relative efficiency still needs to be flattened as a function of centrality and leading jet p_{T} (because it enters the measured quantity) and η (because parton energy loss may depend on pseudorapidity). Since the b-jet trigger is built on top of the inclusive jet trigger, the b-jet trigger efficiency is evaluated using events that pass the offline selection and that fire the inclusive jet trigger. The fraction of these events that also fire the corresponding b-jet trigger is the online tagging efficiency. The online tagging efficiency is shown in Fig 4.8 as a function of centrality, η and p_{T}. The centrality dependence is fit with an error function, the η dependence is fit with a fourth-order polynomial and the p_{T} dependence is fit with a third-order polynomial. Figure 4.8 shows the b-jet trigger efficiency before (lines) and after (symbols) correction.

After correcting each variable, corrections of two other variables are also applied to show their independence. We remind that this procedure was needed only for PbPb collisions, since for pp collisions there was no dedicated b-jet trigger and the data from inclusive jet trigger has been used.

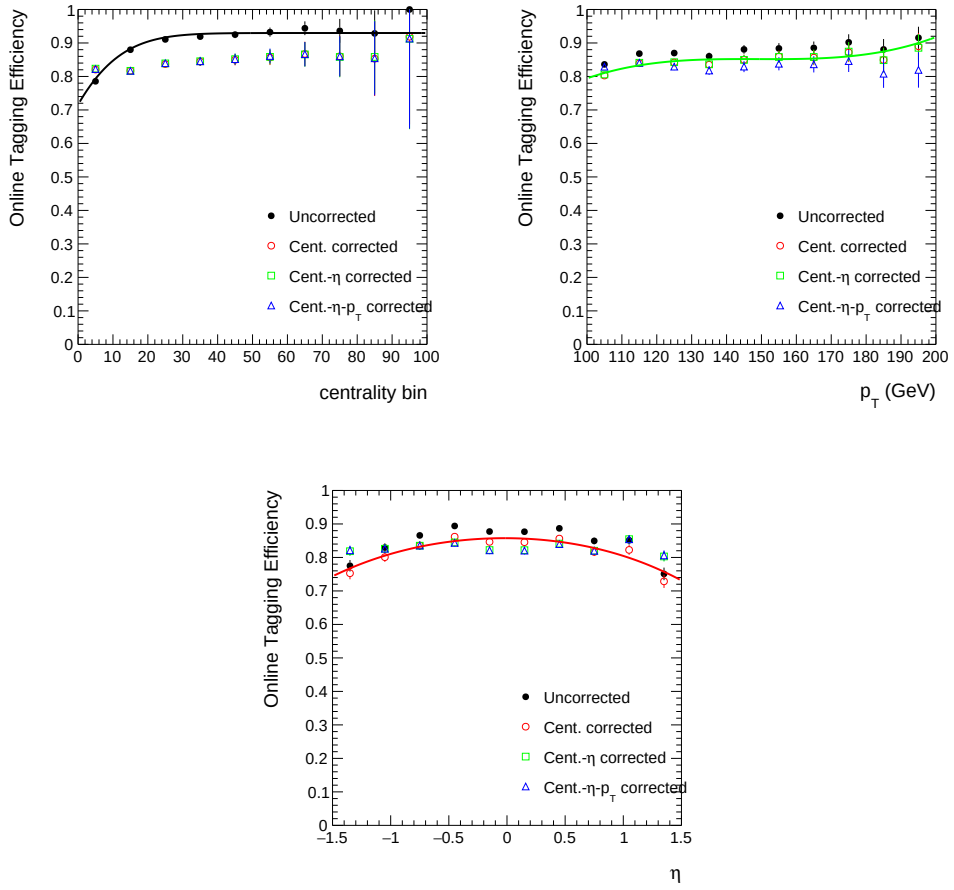

Figure 4.8: Online tagging efficiency of leading b jets as a function of centrality, p_{T} and η for PbPb collisions (closed points). The lines show fits to the tagging efficiency, and the open points show the efficiency after each level of correction is a applied as indicated in the legend.

4.3 Tagging efficiency corrections

This analysis considers self-normalized yields such that no correction is necessary for the absolute b-tagging efficiency. However, we still do need to consider the dependence of the b-tagging efficiency on quantities that influence the measured dijet asymmetry. The dependence of the efficiency on p_{T} is clearly important, as it enters directly into the asymmetry. It is also important to consider the

dependences on centrality and pseudorapidity, as quenching effects should depend on these variables. The corrections are evaluated from b-jet pairs that pass the jet kinematic selections on p_{T} and $\Delta\phi$. To make better use of the Monte Carlo statistics, the tagging efficiencies of the two jets are assumed to be independent. In other words, the leading jet tagging efficiency is evaluated without requiring that the partner jet is tagged, and vice-versa.

The pp tagging efficiency from PYTHIA6 is shown in Fig. 4.9 for p_{T} and η of the leading and subleading jet. The leading jet efficiency is fit first. The p_{T} dependence shows a rather sharp drop at around 150 GeV. This is the consequence of the p_{T} dependent calibrations used for the CSV discriminator. To fit this behavior, a piece-wise function is used, composed of a first-order polynomial below 150 GeV, and a second-order polynomial above. The η dependence is fit with a fourth-order polynomial, where the coefficient of the odd-powered terms are fixed to zero. A third-order polynomial is used for the partner jet p_{T}, while the η dependence is fit with the same functional form as for the leading jet. The tagging efficiency is also shown after application of the efficiency corrections. The corrections are normalized such that the average correction is one, although the absolute scale of the corrections does not affect our (self-normalized) measurements. As a result, the corrected curves carry the average *dijet* (i.e., double) tagging efficiency, while the uncorrected curves correspond to that of single jets. The corrected points have been fit with to a constant to illustrate the degree of closure of the corrections.

In PbPb collisions, the centrality dependence of the tagging efficiency must also be fit, which is done with a third-order polynomial. The correction is applied before the p_{T} and η dependences are evaluated for both the leading and subleading jet. Although there is a sizable centrality dependence over the full range, it should be noted that we bin rather finely in centrality, such that this correction is only necessary to flatten the centrality dependence within each bin. Figure 4.10 shows the fits to the tagging efficiency in the 0-10% centrality bin. The plots for other centrality bins look similar.

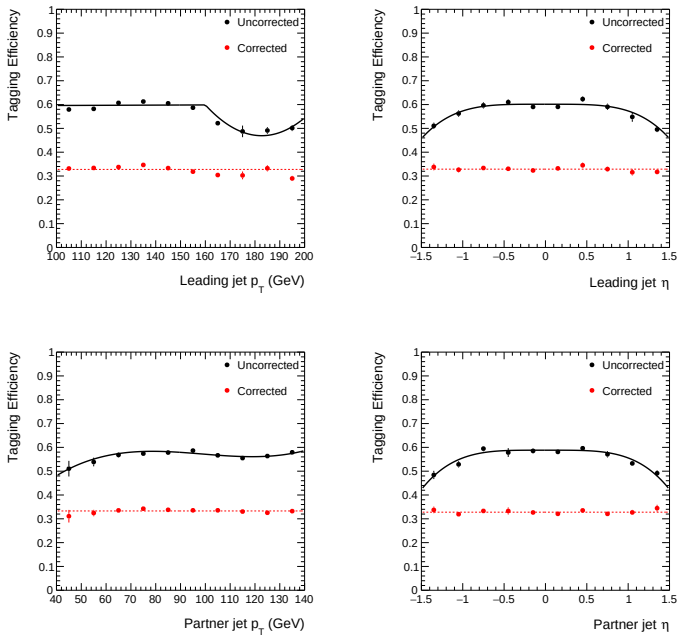

Figure 4.9: Tagging efficiency of b jets as a function of leading and subleading jet p_{T} and η for pp collisions (black points). The black lines are fits to the tagging efficiency, which are then applied for the red points. The red lines show fits to a constant to illustrate the closure of the fits.

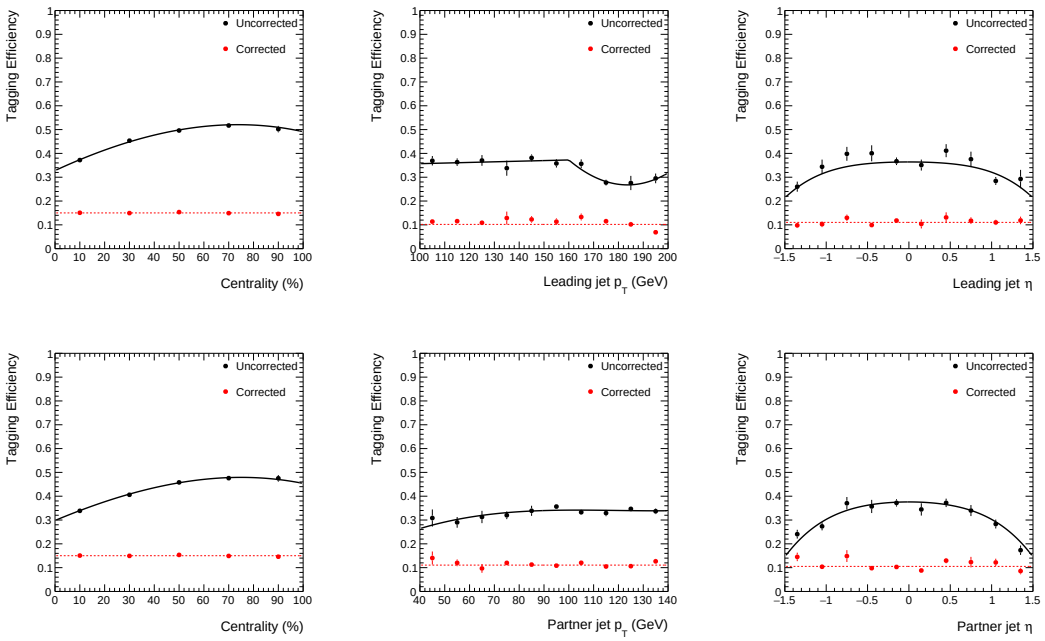

Figure 4.10: Tagging efficiency of b jets as a function of leading and subleading jet centrality, p_{T} and η for 0-10% PbPb collisions (black points). The black lines are fits to the tagging efficiency, which are then applied for the red points. The red lines show fits to a constant to illustrate the closure of the fits.

4.4 Correlation between leading and subleading jets

Before the study of quenching of b-jets in PbPb collisions, one has to establish a baseline with the study of inclusive dijets, which are dominated by lighter quarks and gluons. As it is shown on Fig. 4.3, only $\sim 3\%$ of jets with momentum above 100 GeV are b-jets. For such a study, we follow the approach in previously performed analyses of dijets in CMS [71, 20]. In the inclusive dijet, only about a quarter of pairs originate from quarks on both sides (Fig. 4.11), therefore the direct comparison of inclusive and b-dijet results can highlight the difference of quark and gluon energy loss mechanisms.

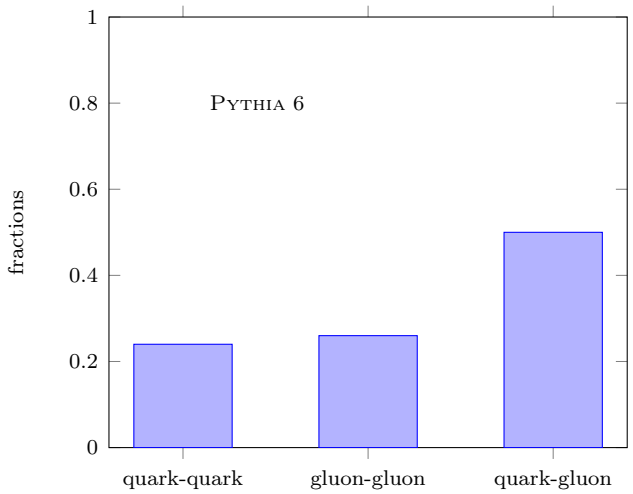

Figure 4.11: Quark-gluon combinations in dijets for the kinematic selection of this analysis in Pythia 6 QCD events at $\sqrt{s} = 5.02$ TeV.

Compared to PbPb, pp collisions have a very small underlying event and provide a clean environment for dijet studies. Each event can be characterized by the set of jets within a given acceptance region. In this analysis all the jets have to be within $|\eta| < 1.5$. We call the highest-p_{T} jet of the event inside η selection as the *leading jet*, and the second high one the *subleading jet*. Throughout this analysis a leading and subleading jet selection of 100 and 40 GeV is applied, respectively.

Exploiting the correlation between the leading and subleading jet, we are trying to learn about parton energy loss in the medium. Since the spectrum of leading jets is steeply falling, as shown in Fig. 4.12 (left), a selection based on the p_{T} of the leading jet returns a sample which is dominated by collisions in which the

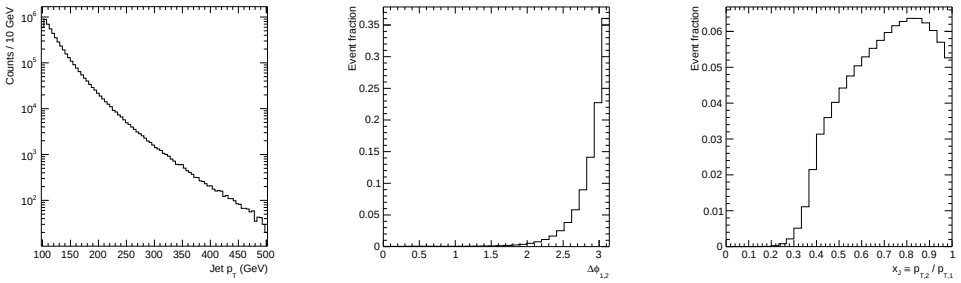

Figure 4.12: Example distributions of leading jet p_{T} (left), $\Delta\phi_{1,2}$ (middle), and x_{J} (right).

leading jet has lost less energy compared to an average jet energy loss. This can be understood as follows: for the given two jets of the same p_{T} one may have bigger energy loss than another and $\Delta p_{T,1} > \Delta p_{T,2}$. Then the original transverse momentum $p_{T,1} > p_{T,2}$ but because the spectrum is falling very fast, the jet with higher transverse momentum is less frequent than jet with lower transverse momentum. Therefore the selection of final jet p_{T} returns jets that have lost less energy.

The azimuthal opening angle between the leading and subleading jets $\Delta\phi$ is displayed on Fig. 4.12 (middle). We can see that dijets in proton-proton collisions are back-to-back in $\Delta\phi$: most of the signal is concentrated in the region $\Delta\phi > 2/3\pi$.

To quantify the modification in the jet energy, we use the dijet momentum ratio i.e. ratio of transverse momentum of the subleading jet to the leading jet of the event, $x_{\mathrm{J}} = p_{\mathrm{T},2} / p_{\mathrm{T},1}$. As seen in Fig. 4.12 (right), the distribution of this variable is far from a delta function even in pp collisions. The main reasons for this are:

- the higher order effects in QCD that can give rise to hard jets such as a hard gluon emission,
- and also to softer radiation and the effects from the underlying event that decorrelate momenta of the two jets.
- The measured distributions are in terms of reconstructed p_{T}, which has detector resolution effects that smears the momenta and hence broadens the x_{J} distribution.

These factors should be taken into account when inferring about the medium

effects from the comparison of PbPb collisions to the pp reference.

4.5 Combinatorial background in PbPb collisions

PbPb collisions have a huge underlying event. As a result there is a (centrality-dependent) probability that the leading and subleading jet will not be from the same hard scattering. These subleading jets, which we refer to as *combinatorial background jets* can be "real" jets, meaning that they are mostly comprised of particles from a single nucleon-nucleon scattering but different than the one that produced the leading jet. In other cases, the content of these jets may correspond to the fluctuations of the underlying event. In this analysis, however, there is no need to distinguish between these mechanisms. We define the *signal subleading jet* as a subleading jet that comes from the same hard scattering as a leading jet.

The problem with combinatorial background is depicted on the Fig. 4.13(left): if the background jet happens to have higher p_{T} than the signal subleading jet, it will be chosen instead. In this case, we no longer measure the correlation between leading and subleading jets in the same hard scattering, but between jets from different hard scatterings.

From the Fig. 4.12 (middle) one can see that in the case of pp collisions (where there is no PbPb underlying event) the contribution of jet pairs coming from the same hard-scattering with $\Delta\phi < \pi/3$ is negligible. Figure 4.13 (right) shows how often subleading jet is in the near-side region for different centrality bins of PbPb collisions in data and simulation. In peripheral collisions the subleading jet is almost never in the near-side $\Delta\phi < \pi/3$ region whereas in central collisions it happens in 13% of cases in simulations and 17% in the data. This happens because the level of the background is multiple times higher in central than in peripheral PbPb collisions, and it vanishes in pp.

The $\Delta\phi$ distribution in PbPb collisions is shown on the Fig. 4.14. The shaded region corresponds to the background subleading jets. It is clear that background distribution is flat in $\Delta\phi$ i.e. the background subleading jet is uncorrelated to the leading jet hence it is called the combinatorial background.

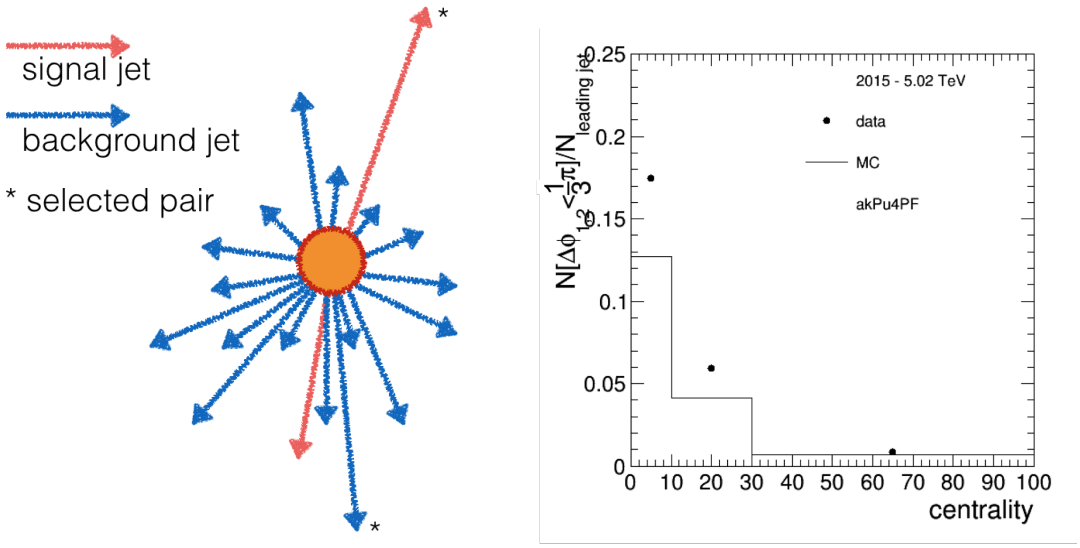

Figure 4.13: The illustration to the problem of the combinatorial background in PbPb collisions (left); The fraction of dijet pairs with $\Delta\phi < \pi/3$, used as an estimate of the rate of combinatorial pairs, for Pb-Pb data and simulation, in the three centrality bins used in this analysis (right)

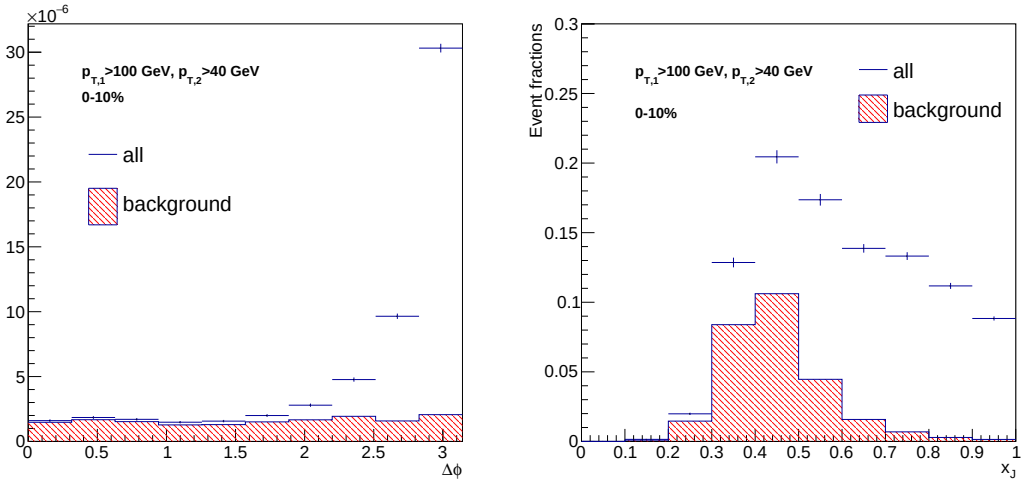

Figure 4.14: The right hand plot does not include the $\Delta\phi$ cut, to show how all the background dijets look like.

The background contributes to the imbalanced (small) x_J, biasing the result. As a first measure to reduce the background impact one can consider $\Delta\phi > \pi/3$ cut which contains almost all the signal and reduces backgrounds by a factor of 3. However, the fact that combinatorial background jets are uncorrelated to the leading jet can be used to perform a combinatorial background subtraction. This method was used in the previous studies of dijets [20] and is employed in this analysis as well. In this approach the x_J distribution of the background is obtained from the near-side region ($\Delta\phi < \pi/3$) pairs and subtracted from the x_J

distribution on the away-side ($\Delta\phi > \pi/3$).

After the subtraction of the combinatorial background contribution, the remaining correlated pairs suffer a bias, which can be significant when the combinatorial background is large. The illustration on the Fig. 4.13 (left) helps again to clarify this problem. Events with a subleading jet from the combinatorial background are subtracted, but at the same time the true pairs do not appear in the x_J distribution. The rate of this effect depends on the maximum p_T of the combinatorial background jet. This implies that for the same acceptance and kinematic cuts, different set of jet pairs appear in the analysis depending on the centrality. We refer to the signal jet pairs that are affected by the combinatorial background as *eclipsed*.

The performance of the background subtraction method in the 10% most central events in embedded simulation is shown in Fig. 4.15. Here only the not eclipsed pairs are considered, since the combinatorial background subtraction can only account for this part.

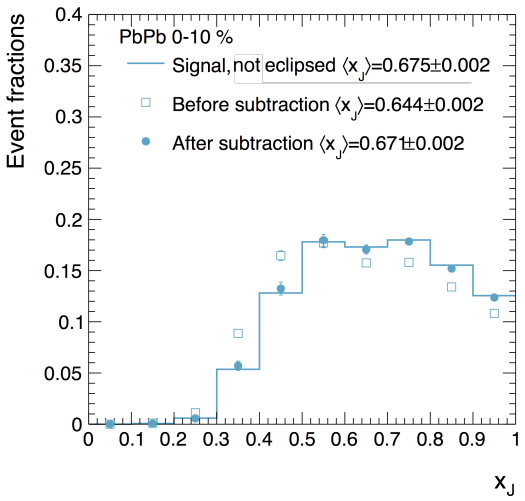

Figure 4.15: The closure of the background subtraction method in 0-10% PbPb events in inclusive jets. Distributions are self-normalized. Only the not eclipsed part of the signal is recovered here.

After subtracting the combinatorial background, the effect of missing jet pairs can be considered as an inefficiency effect for the subleading jets. Higher p_T subleading jets will tend to stand out above the combinatorial background, whereas lower p_T ones are more likely to be eclipsed. Hence, the observed x_J distribution will be

biased towards symmetric pairs. We can obtain this efficiency curve from MC directly, which is shown in Fig. 4.16 (left, points).

It is also possible to estimate the subleading jet efficiency by a data-driven method. The efficiency curve depends solely on a single distribution: the leading jet of the underlying event. The probability of the signal jet of $p_T = x$ to be eclipsed is equal to the probability of the underlying event to produce a jet of x and above. In other words, the subleading jet efficiency is equal to the cumulative distribution function of the leading jet from the underlying event.

$$\epsilon(p_{\mathrm{T}}) \equiv 1 - \frac{1}{N}\int_{p_{\mathrm{T}}}^{\infty} \frac{dN}{dp_{\mathrm{T}}^{\mathrm{max}}} dp_{\mathrm{T}}^{\mathrm{max}} \tag{4.2}$$

This distribution can be estimated from the near-side $\Delta\phi < \pi/3$ distribution of jets where the signal is negligible.

Figure 4.16 shows the efficiency curves obtained from the near-side jet spectra for different centralities. These curves are fit with Gompertz functions, $y = ae^{-bx^{-c}}$, and the fits are used in the analysis as inverse weights for each subleading jet. Figure 4.17 shows the effect of applying eclipse correction on signal jets only.

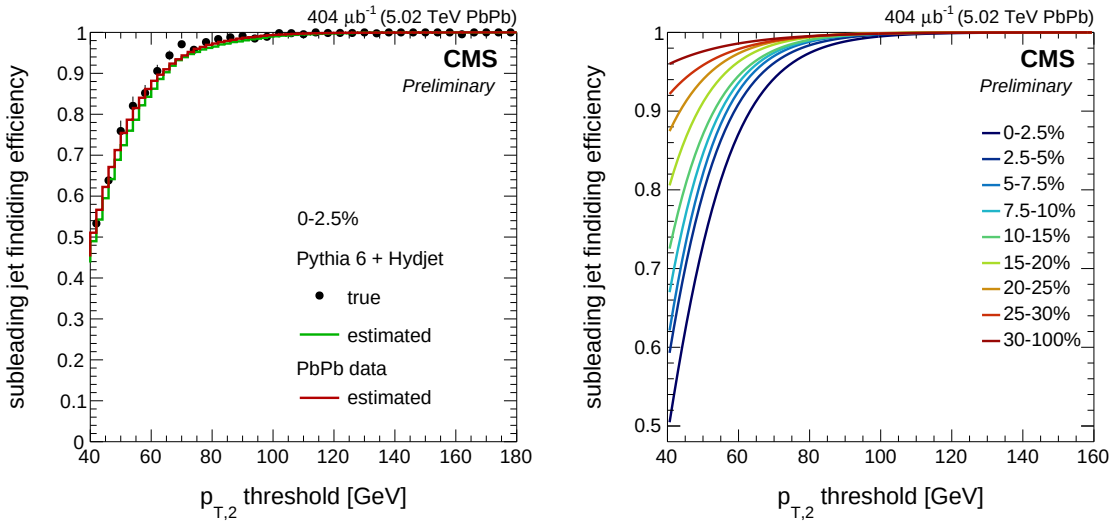

Figure 4.16: Signal subleading jet finding efficiency: true and estimated in simulation and estimated in data for the most central bin (left); efficiency for different centrality bins in data (right)

Although the combinatorial background subtraction was discussed first, the correc-

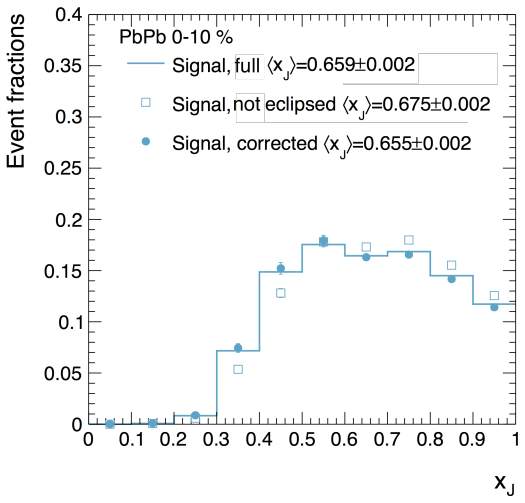

Figure 4.17: Closure test for the eclipse correction for 0-10% centrality for inclusive dijets.

tion weights are actually applied to all jets (including background) in the analysis. The subleading jets on the near-side and away-side are weighted before the combinatorial background subtraction. This enlarges the statistical uncertainties due to the subtraction, however, with the statistics available this effect is tolerable.

The total closure of background subtraction and eclipse correction is presented on Fig. 4.18. The non-closure is explained by the contamination of the near-side background jets with the signal jets.

The discussion above was focused on the inefficiency of the subleading jet only. It may happen that multiple hard scatterings occur in the same PbPb collision. In this case only the hard scattering which produced the highest-p_{T} jet in the event is identified and one can consider this as a bias. However for the kinematic cut of the leading jet (100 GeV) this effect is extremely rare and doesn't make an impact on the measurement. Figure 4.19 shows the effect of the leading jet inefficiency on the leading jet p_{T} distribution and transverse momentum imbalance. Only less than 1% of leading jets are lost and the maximum inefficiency reaches 2.5% for jets at 100 GeV. The mean imbalance $\langle x_{\mathrm{J}} \rangle$ has a mild dependence on the leading jet p_{T} and in this case the effect is less that 0.001 which is much smaller than the systematic uncertainty of this measurement.

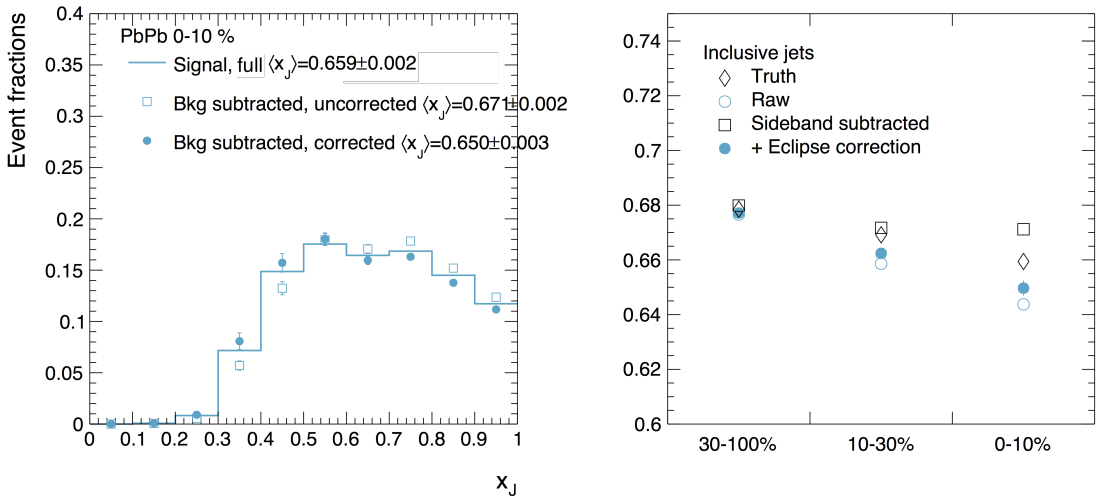

Figure 4.18: Final closure test for the combinatorial background subtraction + eclipse correction. Left: Closure in 0-10% centrality for the x_{J} distribution. Right: Closure of mean x_{J} for all centrality bins.

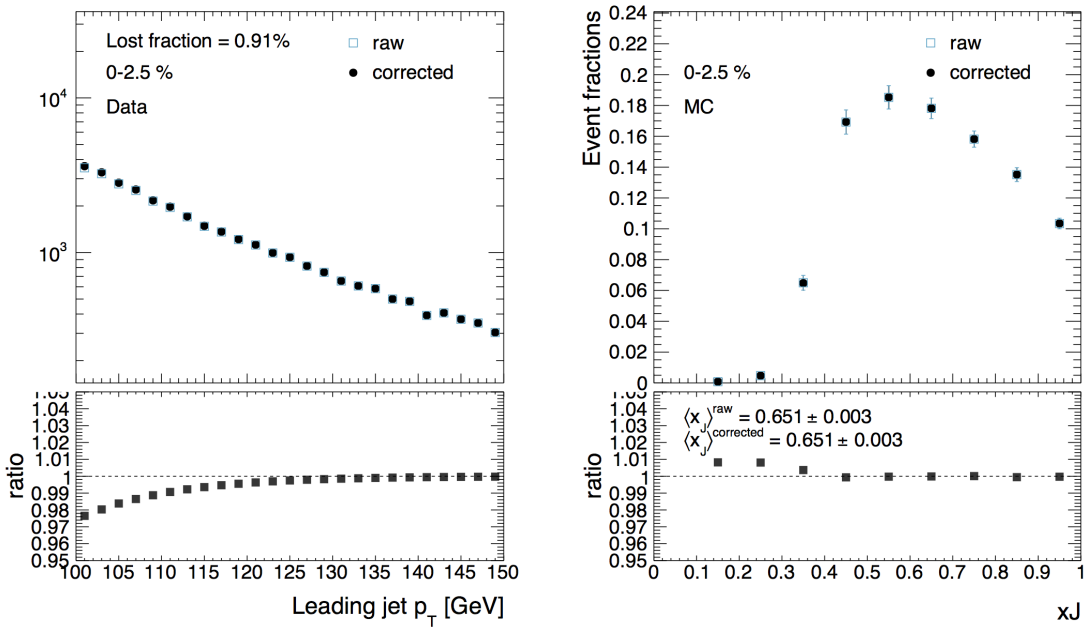

Figure 4.19: Effect of the leading jet eclipsing on the transverse momentum distribution (left) and on the imbalance (right)

4.6 Corrections in the b-dijet analysis

The b-dijet analysis is similar to the inclusive dijet analysis and therefore it relies on the similar procedure of the combinatorial background contamination removal. Note however that in the inclusive dijet analysis when the combinatorial subleading jet is found instead of the true subleading jet the event is kept and the combinatorial jet is taken instead. Later this pair is removed by combinatorial subtraction and the efficiency is corrected with eclipse correction. In the b-dijet analysis, the combinatorial background mostly consists of light jets, therefore this event is discarded by the b-tagger. The combinatorial jet may be still a mistagged jet from the underlying event and the subtraction procedure is needed. But this explains why the background levels are lower in the b-dijet analysis (compare the near-side $\Delta\phi$ band on Fig. 4.31).

In both cases the procedure of correction for the subleading jet inefficiency is the same and the function on Fig. 4.16 derived only once. The final closure test for eclipse correction in b-jet case is shown on Fig. 4.20.

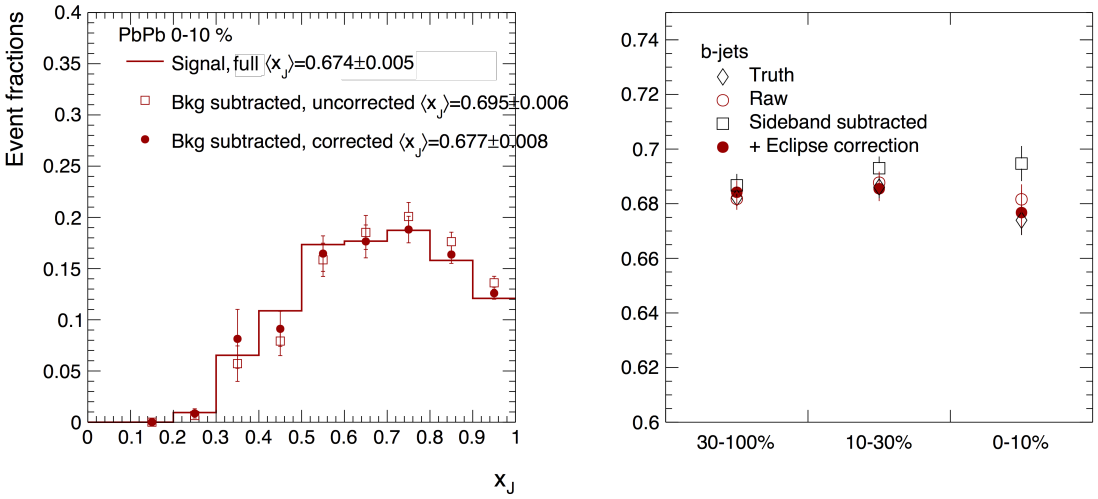

Figure 4.20: Final closure test for the combinatorial background subtraction + eclipse correction in b-jet analysis. Left: Closure in 0-10% centrality for the x_J distribution. Right: Closure of mean x_J for all centrality bins.

The tagging efficiency is specific to the b-dijet analysis and has to be corrected for. The closure of the tagging efficiency corrections is shown in Fig. 4.21. The

tagging inefficiency has a relatively modest effect on the measured mean x_J values, which is generally brought into better agreement after corrections are applied.

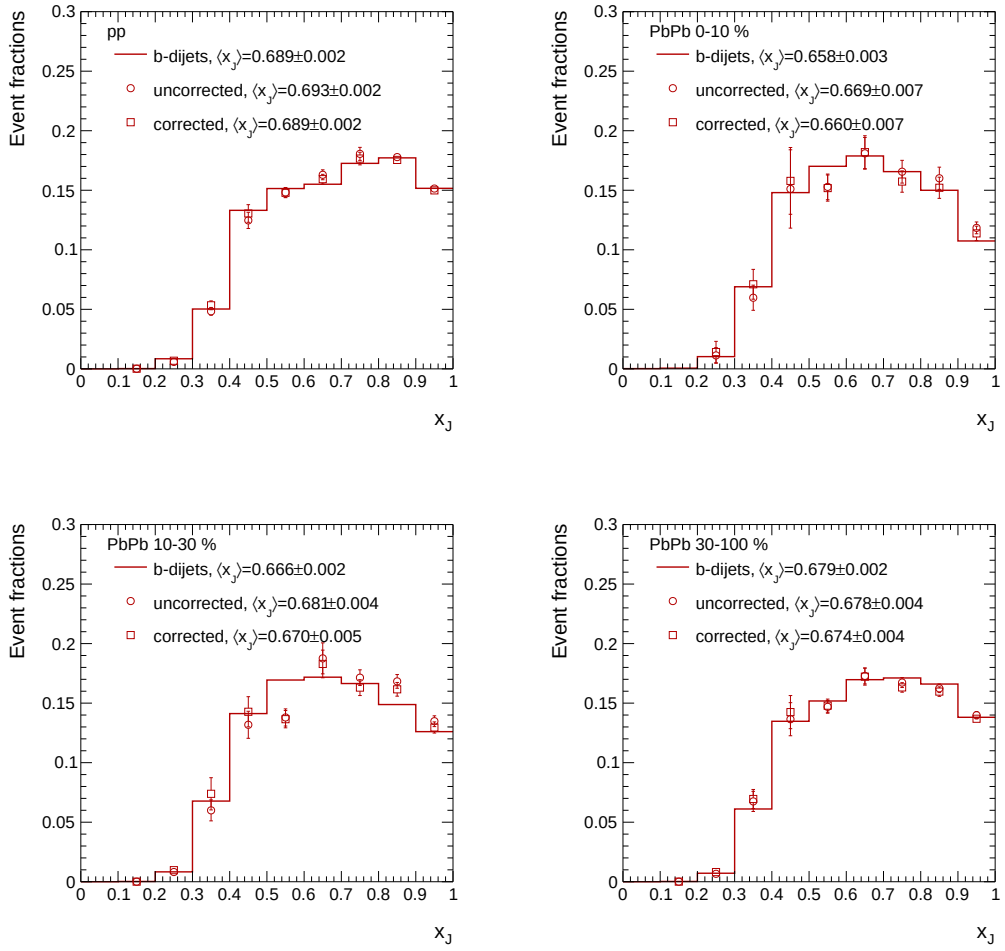

Figure 4.21: Comparison between x_J distributions before tagging, after tagging, and after the efficiency corrections have been applied.

4.7 Systematic errors

4.7.1 Combinatorial jet pairs

The combinatorial subtraction technique relies on the following assumptions: near-side and away-side background distributions are the same and there is no signal on the near-side. The systematic error arises because these two assumptions hold only approximately and they cause the non-closure on the MC tests (Fig. 4.18,4.20).

Combinatorial background subtraction. It was found in the simulation that the combinatorial background distribution is not exactly flat in $\Delta\phi$: the away-side region is ∼20% higher than near-side (Fig. 4.22). We believe that this is the side effect of the simulation: there is a small but non-zero probability that the signal jet is labeled as a background jet. But because the signal is peaked at the away-side $\Delta\phi$, this causes the non-flatness of the background jets distributions.

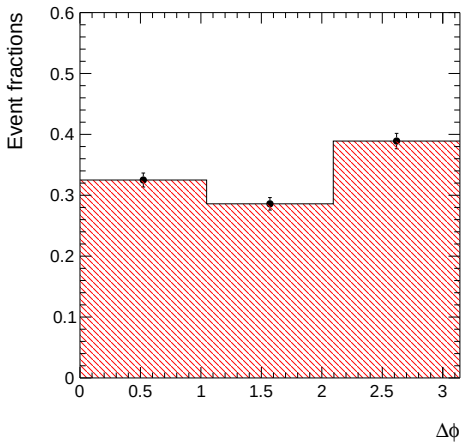

Figure 4.22: The azimuthal opening angle $\Delta\phi$ for background combinatorial jets in central PbPb collisions. Away-side background is $\sim$ 20% higher than near-side.

The systematic uncertainty on the combinatorial background subtraction is evaluated by varying the contribution of the sideband region. For inclusive dijets the size of the sideband is varied by 30%, which is sufficient to cover non-closure of the procedure in simulation. It should be noted though, that this effect is an artifact of the simulation procedure and shouldn't happen in the data, therefore the systematic error is conservative.

For b-dijets, the b-tagging requirement changes the number of jet pairs in the sideband region: the background levels are much lower and much less centrality dependent than for inclusive dijets. Besides, the signal mislabeling is not a problem anymore i.e. the background distribution is flat. However, simulations show that the dominant contribution in the nearside region is from signal jets from gluon splitting. The subtraction is still performed in order to get rid of the background, but the subtraction induces centrality-independent bias. We therefore use the entire effect of the sideband subtraction in pp data to estimate the systematic

uncertainty on the subtraction procedure in PbPb data.

Eclipse correction. The correction for the subleading jet finding inefficiency is calculated only once (from the inclusive dijet $\Delta\phi$ distribution) and applied to both inclusive and b-dijet analyses. But the procedure is not perfect due to several reasons: a small but nonzero contribution of signal jets in the nearside region ($\Delta\phi < \pi/3$), the finite centrality binning used for efficiency determination and the imperfect description of the fit function employed. The systematic uncertainty associated with these corrections is evaluated from the non-closure in embedded simulation and it is applied to both analyses.

4.7.2 Jet reconstruction

Jet energy scale The several factors affecting the energy scale can be combined into two components: correlated and uncorrelated. Among the correlated are: the overall scale uncertainty in pp [139], the difference between data and simulation, modification of jet fragmentation from quenching [140, 141, 85, 142]. The correlated component is applied to both the leading jet (by 6%) and subleading jets (by 8%) simultaneously, and has a minor impact on the x_J results since the majority of the effect cancels in the ratio. The uncorrelated jet energy scale uncertainty comes from the underlying event subtraction. In order to evaluate this effect, the possible energy scale variation is applied to the subleading jet only. Figure 4.23 shows the impact of a 2% shift of energy scale on the measured x_J distributions. For both data and MC, this results in an 0.012 shift in $\langle x_J \rangle$, which is the dominant part of the energy-scale uncertainty in the final results.

Jet energy resolution The resolution uncertainty in pp is determined by varying the smearing parameters that describe the jet resolution in formula (3.3). To determine the uncertainty in pp, C (± 0.02) and S (± 0.2) are varied and particle-level jets are smeared by the corresponding amount. This variation also contains the difference of the C and S terms between pp and PbPb (Fig. 4.24 left). For PbPb, in addition to the uncertainty in pp, the N term is varied (± 2 GeV), which covers the difference in underlying event between data and MC, and the variation of the resolution within the wide centrality bins (Fig. 4.24 right). Although the

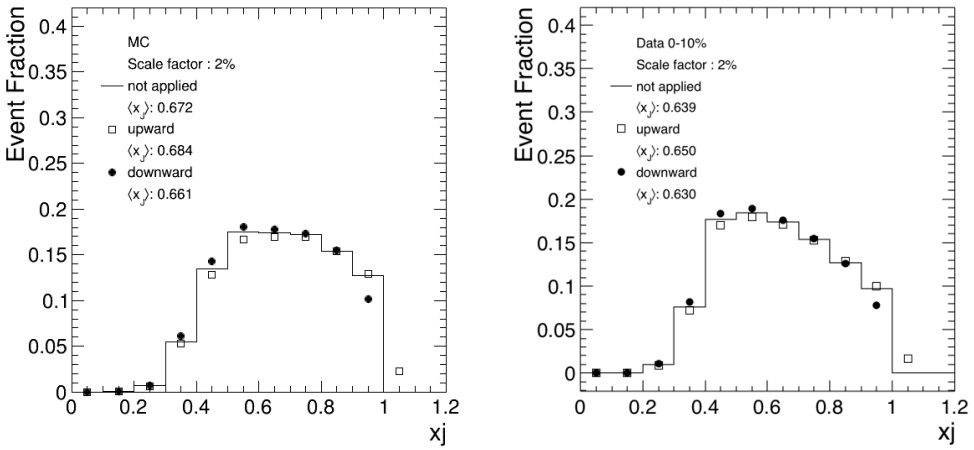

Figure 4.23: The effect of a 2% energy scale shift (upward and downward) on subleading jet only, for inclusive dijets in MC and data.

results are not unfolded for the resolution effects, the uncertainty is fully included in the data points in order to correctly evaluate any theoretical models that fold in the resolution effects for comparison.

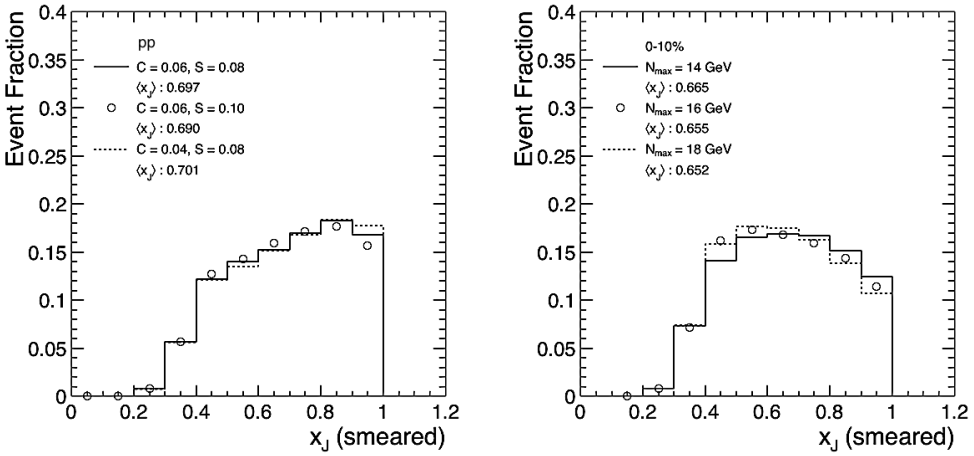

Figure 4.24: The effect of smearing jet resolution in pp (left) and PbPb (right).

4.7.3 b-tagging

The sources of systematics described in Sections 4.7.1 and 4.7.2 are applicable to both inclusive and b-dijet measurements, while b-tagging is applied to the latter only.

Tagging efficiency. The tagging efficiency has a fairly flat dependence in p_{T} such that it has only a mild effect on the observed $\langle x_{\mathrm{J}} \rangle$ as it was shown on closure

tests (Fig. 4.21). After the correction, the good agreement between the true and corrected $\langle x_J \rangle$ is observed. The size of the corrections are varied by 50% as a conservative estimate of the systematic uncertainty.

Signal mistagging. Although a relatively tight working point of CSV tagger is used, there remains a contamination of jet pairs for which one of the jets (or both) is not associated to a b-quark. If this mistagged jet is from combinatorial background, it is subtracted. But otherwise it may come from the hard scattering which is a signal mistagging in this case. Figure 4.25 shows the flavor composition of tagged pairs in pp and Pb-Pb (combinatorial jets are not shown), divided into several exclusive categories: BB is a correctly tagged pair of b-dijets, BX (XB) represents the pairing of a leading (partner) b-quark jet with a jet of any other flavor including charm, XX represents the pairing of any two non-b-jets, except for c-quark pairs, which are shown separately. The dominant background arises when one of the two jets is a real b jet, but the other is mistagged. This mistagging occurs for the leading and partner jet in roughly equal measure. The next largest background consists of c-quark jet pairs.

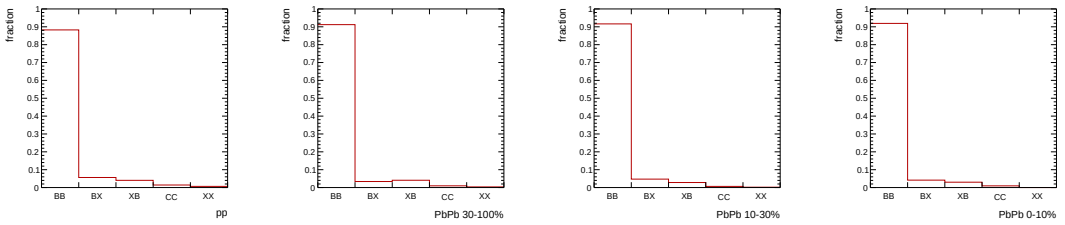

Figure 4.25: The flavors of tagged jets in simulation for pp and PbPb for the three centrality bins.

To estimate the effect of mistagged pairs in data, we inverted the CSV tagger, using a selection CSV < 0.5 to reject b jets. For the leading jet, we simply repeat the analysis with this inverted selection. For the subleading jet, we weight the pair according to the probability of mistagging as a function of the jet p_T (Fig. 4.26) in order to reproduce the correct imbalance of the mistagged pair.

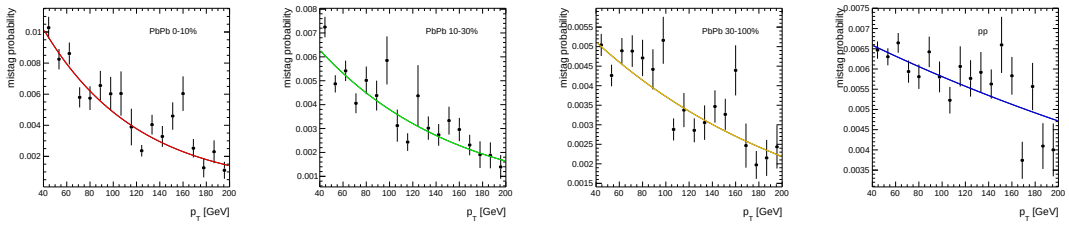

Figure 4.26: Mistagging probability as a function of p_{T} for different centralities.

4.7.4 Systematics summary

The absolute systematic uncertainties on $\langle x_{\mathrm{J}} \rangle$ for the inclusive dijet and b-dijet measurements are summarized in Tables 4.2 and 4.3, respectively.

Source	pp	30-100%	10-30%	0-10%
Combinatorial subtraction	-	0.001	0.006	0.014
Subleading jet finding	-	0.002	0.004	0.004
Jet energy scale	0.001	0.006	0.010	0.013
Jet resolution	0.007	0.008	0.010	0.012
total	0.007	0.010	0.016	0.023

Table 4.2: Absolute systematic uncertainties on $\langle x_{\mathrm{J}} \rangle$ for inclusive dijets.

Source	pp	30-100%	10-30%	0-10%
Combinatorial subtraction	-	0.008	0.008	0.008
Subleading jet finding	-	0.002	0.004	0.004
Jet energy scale	0.001	0.006	0.010	0.013
Jet resolution	0.007	0.008	0.010	0.012
Tagging efficiency	0.002	0.003	0.003	0.009
Signal mistagging	0.002	0.004	0.006	0.006
total	0.008	0.014	0.018	0.023

Table 4.3: Absolute systematic uncertainties on $\langle x_{\mathrm{J}} \rangle$ for b-dijets.

4.7.5 Systematic error on the distribution

To evaluate the systematic uncertainties on the x_{J} distributions themselves, as opposed to their mean values, we need to take into account that these are self-normalized distributions. This implies an anti-correlation: if the yield at small x_{J} is reduced, the yield at large x_{J} must increase in order to preserve the normalization. To evaluate the systematic error band in a way that is consistent

with the total uncertainty on the mean x_J value, we use the following procedure. The histogram is divided into two parts, one to the left and one to the right of the bin boundary closest to the true mean value. Then the values to the left are multiplied by some factor, while the values to the right are multiplied by another factor preserving the integral of the distribution. The factor is such that the mean value of the new distribution matches the mean value of the original distribution minus (plus) the systematic error. The same variation is applied to the other side of systematic error. In this way both variations preserve the unitarity of x_J distribution as well as the anti-correlation of the bin values. Both variations are illustrated on Fig. 4.27. The total span between two variation is taken as a systematic uncertainty for each bin.

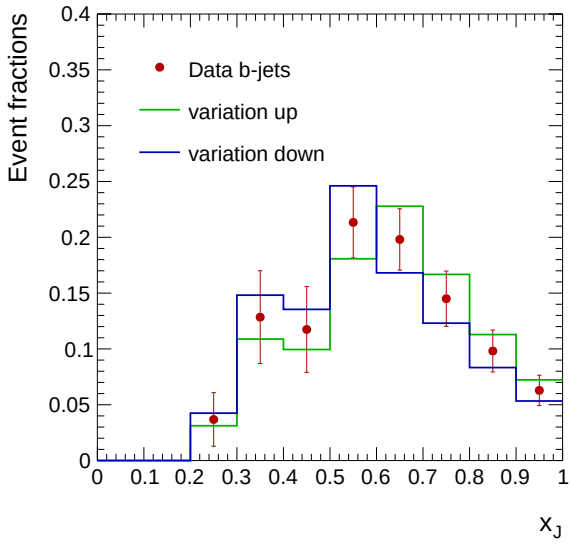

Figure 4.27: Variations of x_J distribution to match systematic error on the mean value

4.8 Results

The p_T balance of inclusive and b dijets is presented, as quantified by x_J, the ratio of the subleading to leading jet p_T. Results are presented for a leading and subleading jet p_T of more than 100 and 40 GeV, respectively, selected from jets in $|\eta| < 1.5$.

4.8.1 $\Delta\phi$

First, the azimuthal opening angle between the leading and subleading jets $\Delta\phi$ is presented for pp (Fig. 4.28), peripheral (Fig. 4.29), mid-central (Fig. 4.30) and central (Fig. 4.31) PbPb collisions. We can see that the level of the background in inclusive jet measurement is increased significantly which is not true for b-dijet measurement.

The $\Delta\phi$ distributions are fit with $c+a\cdot\exp(x/\sigma)$ function and the width parameter σ is quoted in tables 4.4,4.5. As it was the case in the previous dijet measurements [20], no significant broadening (increase of the width) of the dijet angular correlations is observed in all centrality bins.

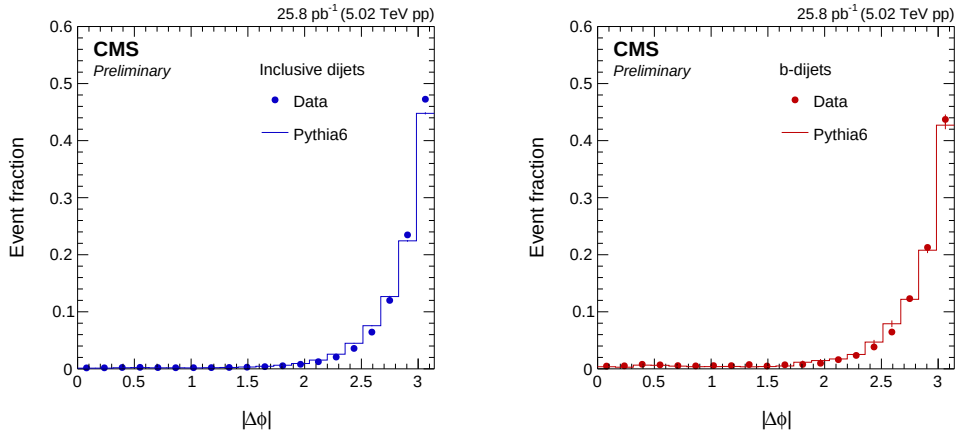

Figure 4.28: $\Delta\phi$ distributions for inclusive (left) dijets and b-dijets (right) in pp collisions.

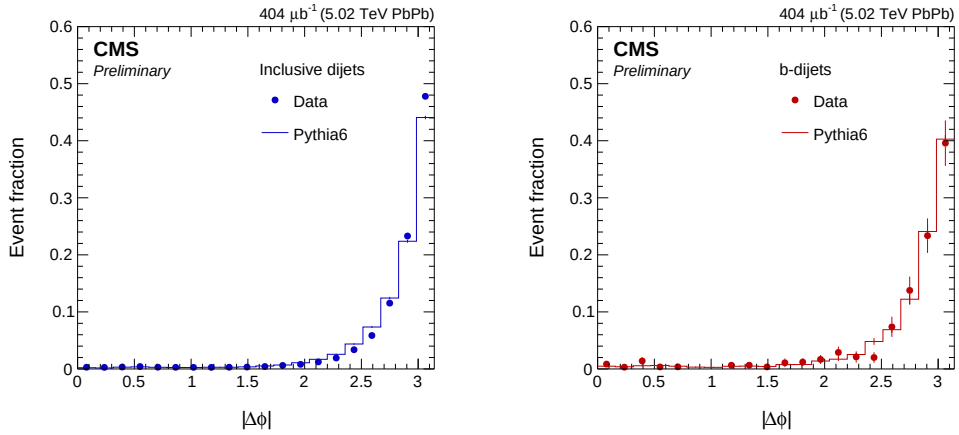

Figure 4.29: $\Delta\phi$ distributions for inclusive (left) dijets and b-dijets (right) in peripheral (30-100%) PbPb collisions.

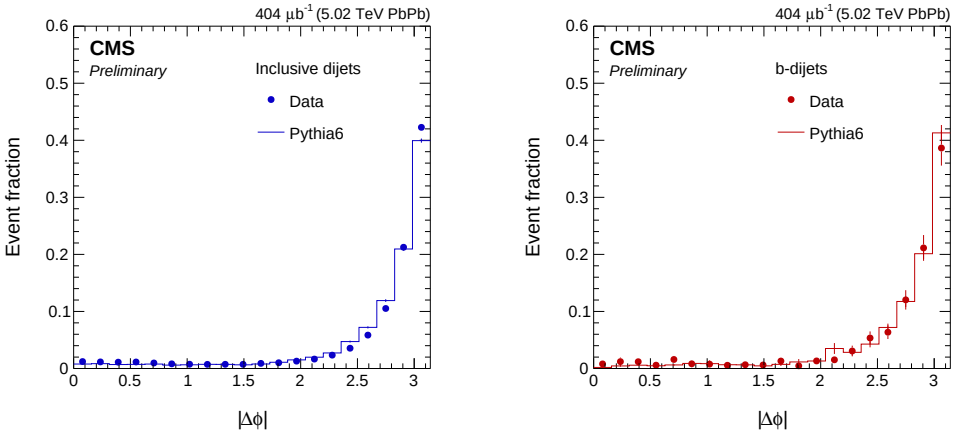

Figure 4.30: $\Delta\phi$ distributions for inclusive (left) dijets and b-dijets (right) in mid-central (10-30%) PbPb collisions.

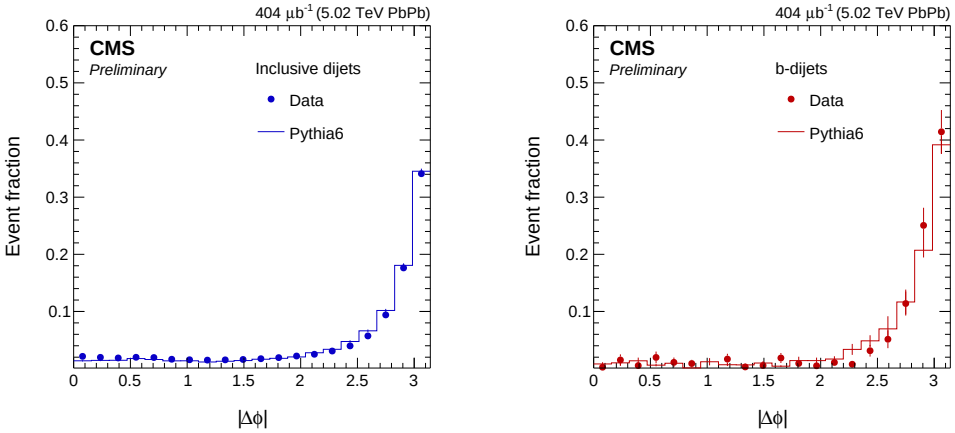

Figure 4.31: $\Delta\phi$ distributions for inclusive (left) dijets and b-dijets (right) in central (0-10%) PbPb collisions.

	Pythia 6	Data
pp	0.267±0.001	0.239±0.001
30-100%	0.267±0.002	0.227±0.001
10-30%	0.265±0.003	0.225±0.001
0-10%	0.260±0.004	0.227±0.001

Table 4.4: $\Delta\phi$ widths for inclusive jets.

	Pythia 6	Data
pp	0.260±0.005	0.242±0.004
30-100%	0.268±0.007	0.250±0.021
10-30%	0.270±0.011	0.259±0.019
0-10%	0.289±0.016	0.215±0.016

Table 4.5: $\Delta\phi$ widths for b-jets.

4.8.2 x_J

The x_J distributions for inclusive dijets and b-dijets are shown for pp collisions in Fig. 4.32. The data are compared with simulations performed with PYTHIA 6. Figures 4.33, 4.34 and 4.35 show the x_J distributions for PbPb collisions with centrality selections of 30-100%, 10-30% and 0-10%, respectively. Here the data are compared to the reference obtained from pp data by smearing the p_T of each jet according to a parametrization of the resolution for the given centrality class.

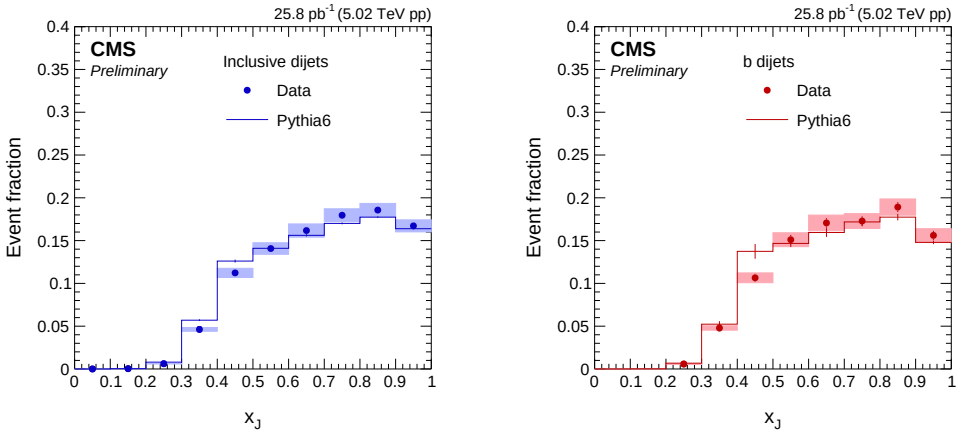

Figure 4.32: Distribution of x_J in pp collisions for inclusive dijets (left) and b-dijets (right). Systematic uncertainties are shown as shaded boxes, while statistical uncertainties are shown as vertical lines.

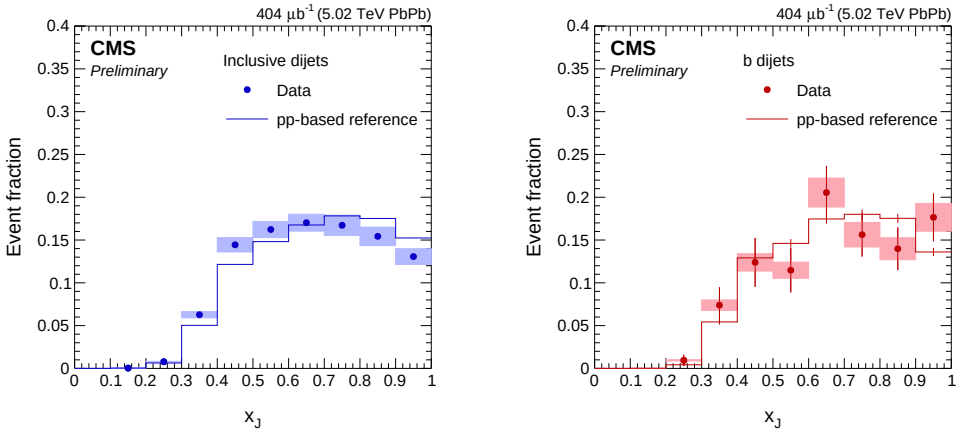

Figure 4.33: Distribution of x_J in peripheral (30-100%) PbPb collisions for inclusive dijets (left) and b-dijets (right). Systematic uncertainties are shown as shaded boxes, while statistical uncertainties are shown as vertical lines.

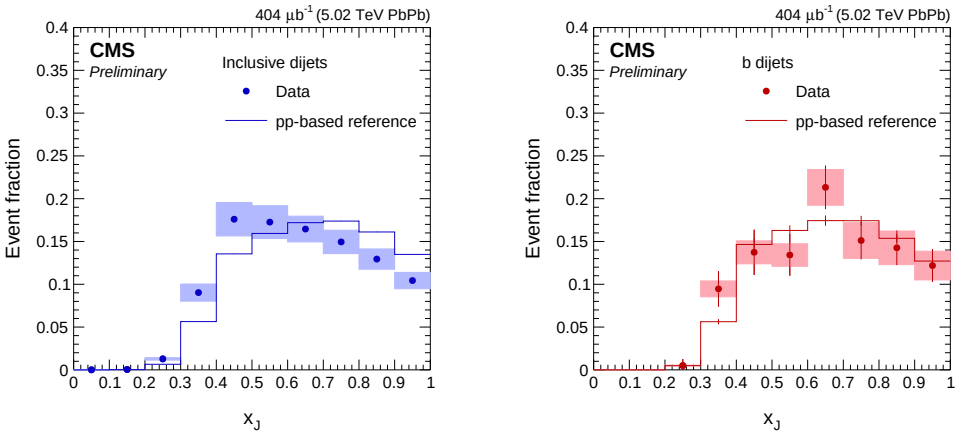

Figure 4.34: Distribution of x_J in mid-central (10-30%) PbPb collisions for inclusive dijets (left) and b-dijets (right). Systematic uncertainties are shown as shaded boxes, while statistical uncertainties are shown as verticial lines.

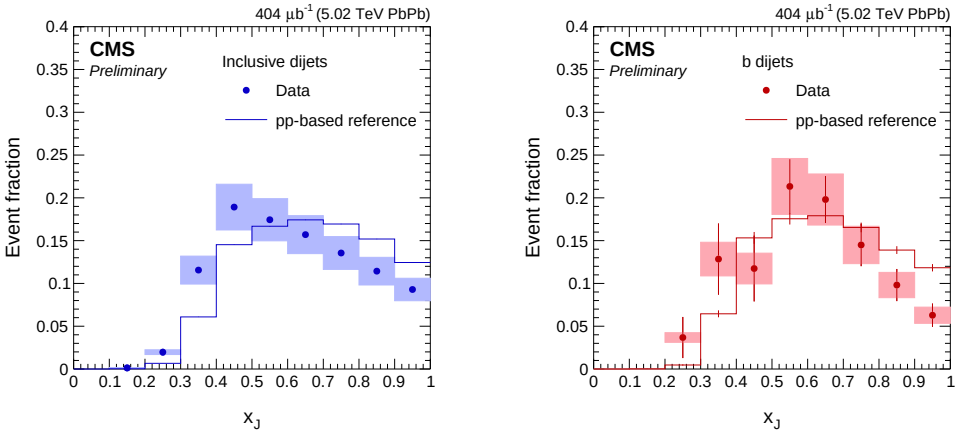

Figure 4.35: Distribution of x_J in central (0-10%) PbPb collisions for inclusive dijets (left) and b-dijets (right).

The ratio of dijet to single jet events, R_J, is presented on Fig. 4.36. This quantity describes how often a leading jet has a pair in the acceptance and kinematic selections.The subleading jet may be outside of the acceptance region $|\eta| < 1.5$, which explains the low value of R_J in pp collisions. However in PbPb collisions, the quenching decreases the energy of the jet and some of the subleading jets appear below p_{T} threshold of 40 GeV. This is the reason why simulation is different from the data in central PbPb collisions.

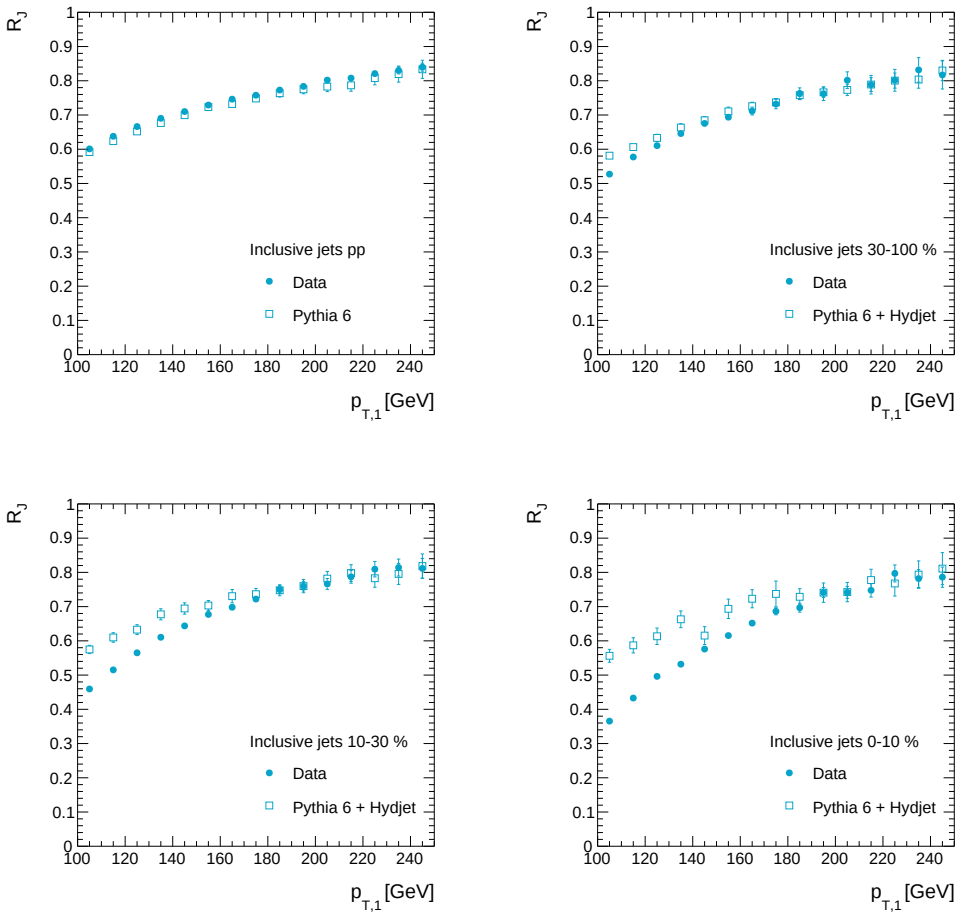

Figure 4.36: Dijet to leading jet events ratio for pp and PbPb collisions.

4.8.3 Summary plots

Figure 4.37 shows the mean x_J values. The data are plotted as a function of the number of participants estimated from a Monte Carlo Glauber model [8, 143]. The number of participants is weighted by the number of collisions to account for the hard scattering bias within each bin.

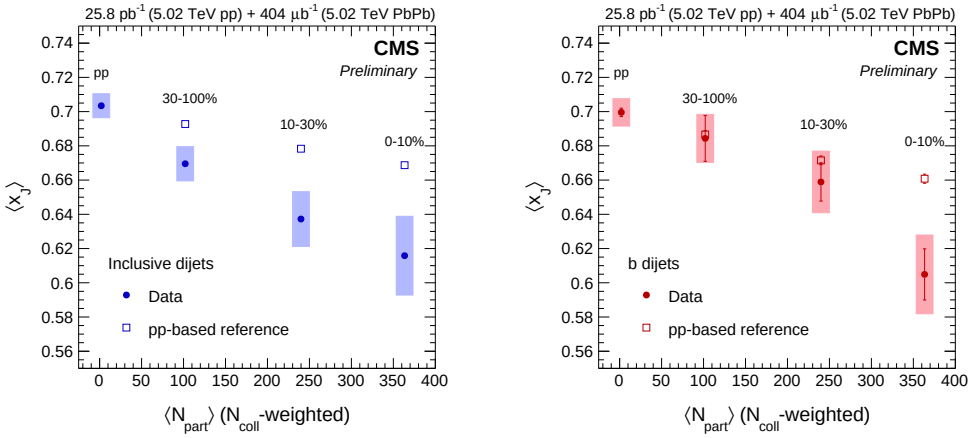

Figure 4.37: Mean x_J for inclusive (left) dijets and b-dijets (right) in pp collisions and for different centrality selections of PbPb collisions. Systematic uncertainties are shown as shaded boxes, while statistical uncertainties are shown as vertical lines.

Figure 4.38 shows the ratio of b-dijet to inclusive jet mean x_J, and Fig. 4.39 shows the difference and ratio of PbPb to pp results for both analyses.

Both the inclusive dijet and b-dijet data show a tendency towards increasing imbalance with increasing centrality. While the reference also becomes more imbalanced due to resolution effects, the magnitude of the effect is much smaller. The effect is understood to be due to jet quenching, as observed in previous inclusive dijet results [71, 20]. Within the current uncertainties no significant difference is observed between the quenching of inclusive and b-dijets. Whereas the inclusive dijets contain a mix of quark and gluon jets, the b dijets mostly originate from primary b quarks. The measurement places constraints on the possible mass and flavor dependence of quenching for the kinematic regime currently probed.

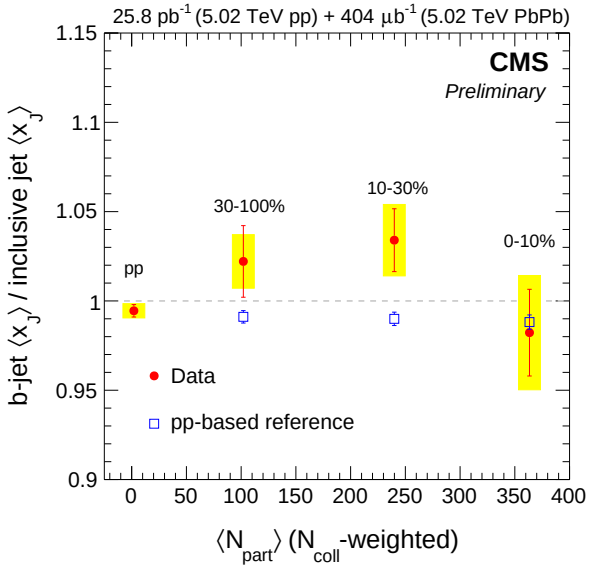

Figure 4.38: Ratio of b-dijet to inclusive mean x_{J} as a function of the collision centrality.

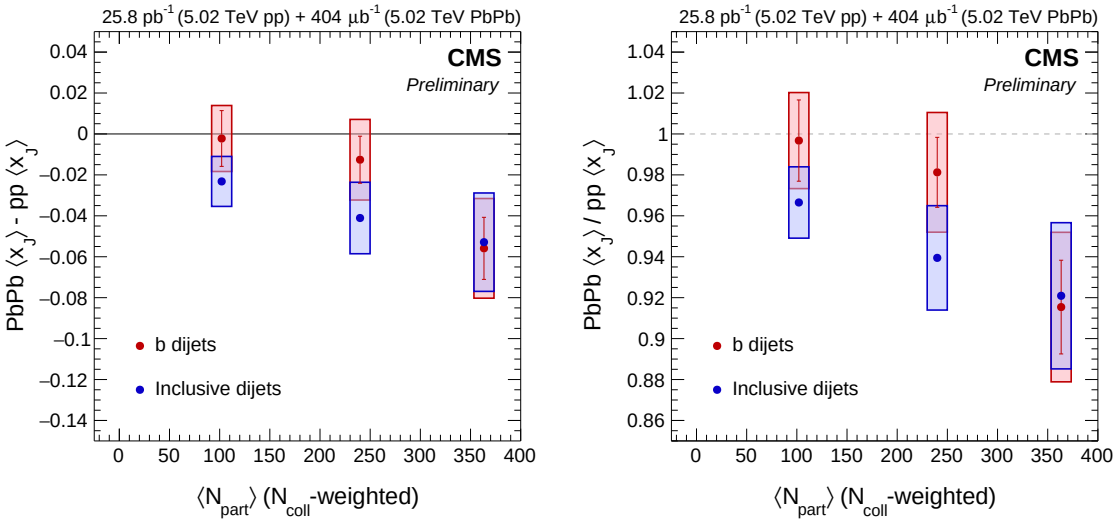

Figure 4.39: Difference (left) and ratio (right) of PbPb and pp results for inclusive and b-dijet analyses.

Discussion

5.1 Assessment of the parton energy loss

The results presented in the previous chapter show unambiguously that both inclusive and b-jets are indeed quenched. But in order to quantify the amount of energy loss and highlight the (possible) difference between them one has to rely on an energy loss model. In this chapter, the jet transverse momentum loss Δp_{T} is often denoted as "energy loss" for the brevity.

The discussion below is based on the model described in Ref. [36]. The energy loss of a quark jet is modeled by subtracting a predefined value from the jet ($p'_{\mathrm{T}} = p_{\mathrm{T}} - \Delta p_{\mathrm{T}}$) parametrized as follows:

$$\Delta p_{\mathrm{T}q,g} = s_{q,g}\left(\frac{p_{\mathrm{T}}}{p_{\mathrm{T},0}}\right)^{\alpha} \tag{5.1}$$

The parameter s_q is the energy loss of a quark jet at the momentum $p_{\mathrm{T},0}$. It depends on the centrality and is found to be linearly dependent on N_{part} from the fitting of the jet nuclear modification factor. The important part of the model is a difference in energy loss of jets originating from quarks and from gluons: $s_g = c_F s_q$. As it was discussed in Sec. 1.2.3, the gluon emission off a gluon is different from the gluon emission off a quark, hence one can expect the difference in their energy loss scenarios. The parameter c_F was found to be $c_F = 1.8$ and this value is used throughout the study described in this section.

As described in [36], "clearly lacking in the model is the implementation of fluctuations of the jet quenching and its path-length dependence. Thus parameters used

in the model should be viewed as effective parameters. The direct interpretation of values of α or s is not immediately possible." Nevertheless, the simplicity of the model allows to describe the variety of observables with a few effective quantities providing the intuition about the energy loss process in the medium.

We will use this model to describe the transverse momentum imbalance of inclusive jets, in particular we are interested whether one can obtain x_{J} distribution of central PbPb collisions (Fig. 4.35, left) starting with x_{J} in pp collisions (Fig. 4.32, left) and applying the energy loss following the model. Given a reconstructed pair of dijets in Pythia, the energy loss is calculated according to Eq. 5.1 with parameter s for the leading jet and with parameter $s' = s + r$ for the subleading jet (the rationale for such parametrization is explained below). If the jet originates from the gluon, the quenching is increased by factor $c_F = 1.8$.

The imbalance of quenched Pythia can be compared to PbPb results only after the smearing procedure described in Sec. 3.2.4, hence the random fluctuation is added to both dijets by sampling the Gaussian distribution with the width corresponding to the N parameter of jet resolution. The C and S parameters must not be applied because the starting jets are reconstructed jets in pp (with the corresponding resolution effects included). The last step is to determine whether leading jet p_{T} is still above the subleading jet p_{T} and switch the order otherwise. After the simulation, one obtains the x_{J} distribution which should be compared to PbPb data. This is achieved by calculating the χ^2 value:

$$\chi^2 = \sum_{i=3}^{n_b} \frac{(E_i - O_i)^2}{E_i} = N \times \sum_{i=3}^{n_b} \frac{(p_i^{mc} - p_i^{data})^2}{p_i^{mc}}, \tag{5.2}$$

where $n_b = 10$ is the number of bins in the distribution, the summation starts from 3rd bin because first two bins contain too few entries, $E_i = N p_i^{mc}$ is expected number of events, $O_i = N p_i^{data}$ is observed number of events, $N \sim 80000$ is the number of events in the data distribution. The probability to have imbalance in the range $x_{\mathrm{J}} \in [\frac{i-1}{n_b}, \frac{i}{n_b}]$ (in other words, the value of x_{J} in i-th bin) is denoted as p_i^{mc} for the simulation and p_i^{data} for the data.

Given 8 bins and 2 unknown parameters (s and r), such a quantity should obey

χ^2 distribution with $8 - 1 - 2 = 5$ degrees of freedom. When only 1 parameter is fitted, the distribution has 6 degrees of freedom.

The first attempt to fit the x_J distribution with independent energy loss on the leading and subleading jet is shown on Fig. 5.1. The axes correspond to the energy s and $s + r$ subtracted from the jet at 100 GeV and the color represents the value of the χ^2. One can clearly see the linear correlation of the two parameters. In fact, at any leading jet energy loss value, the minimum corresponds to the subleading jet energy loss shifted by some constant value, which justifies the subleading jet energy loss parametrization as $s + r$, where r will be the additional energy lost by the subleading jet. In the following discussion, the minimization plots will be plotted as the leading jet energy loss s versus the subleading jet addition r.

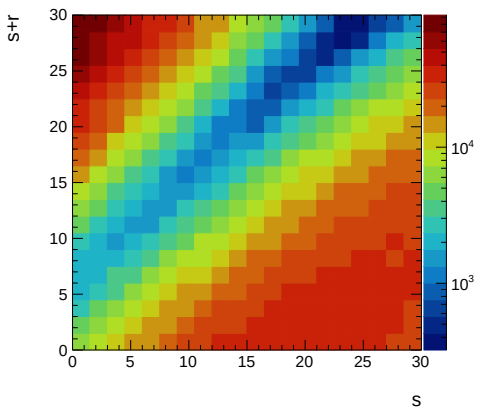

Figure 5.1: The fitting of the energy loss parameters according to the model [36]. Axes correspond to the leading vs subleading energy loss values at 100 GeV, color represents the χ^2 of the fit.

The only free parameter in the model is the additional quenching of the subleading jet r. The result of the fitting procedure is shown on Fig. 5.2. Although, the two-dimensional map is shown, the s parameter is confined within narrow region $7.9-8.1$ GeV, i.e. is effectively fixed. The minimum corresponds to $r = 7$ GeV, but the shape of the predicted distribution differs from the data significantly, which results in a large χ^2 value. It does not necessarily mean that the hypothesis that the model describes the data is rejected by the fit (with $\chi^2 = 1370$ and 6 degrees of freedom, the p-value is ridiculously small). Although the statistical errors on x_J are negligible, the sizable systematic error, pp data-Pythia discrepancy, as well as the simplicity of the model do not rule out the possibility that the current result

is in fact optimal. However, it is interesting to push the model to its limits and see if one can describe the imbalance in PbPb even better.

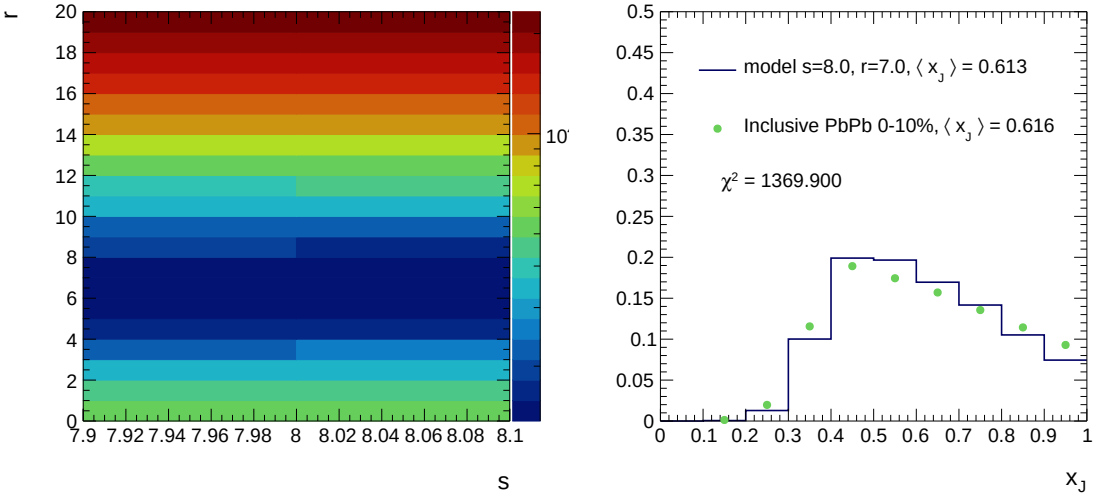

Figure 5.2: The fitting of the energy loss parameters at fixed $s = 8$ GeV. The best fit is for $r = 7$ GeV.

In order to do that, both the s and r parameters were left free and a 2-dimensional search of the minimum is performed. The χ^2 values are shown on Fig. 5.3 (left). One can consider the result of the previous fitting on Fig. 5.2 as a particular case of a search around $s = 8$ GeV. When the s parameter is free, the minimum "slides down" on the χ^2 plane to the point $s = 42.5$ GeV, $r = 1$ GeV. The resulting fit is shown on Fig. 5.3 (middle). In this case, the imbalance is perfectly described with a reasonable χ^2 value.

On the other hand, such choice of the parameters results in the severe suppression of the nuclear modification factor which is a consequence of the steeply falling jet p_{T} spectrum. Figure 5.3 (right) shows the R_{AA} calculated for the leading jet which is of the order of 0.1 and rises mildly with p_{T}. This value is significantly lower than measured in data [82, 19] which is equal approximately to 0.5. It is interesting to perform a minimization procedure which produces optimal parameters satisfying both measured x_{J} distributions and a reasonable R_{AA} value. Since the R_{AA} values are not measured in this analysis, it is assumed to equal to 0.5 with the Gaussian error $\epsilon = 0.01$. This parameter is taken to be small enough to provide a reasonable "attraction" of the fit to the nominal value of 0.5. Then, given the value of $R_{AA} = R$

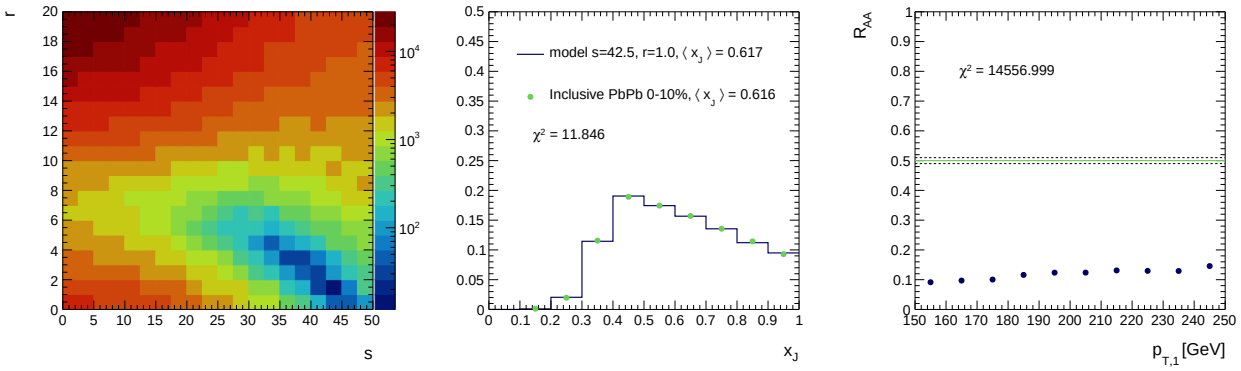

Figure 5.3: The fitting of the energy loss parameters s and r. Optimal parameter values are $s = 42.5$ GeV, $r = 1$ GeV. Map of χ^2 values for different s and r (left), x_{J} (center) R_{AA} (right) distributions corresponding to the optimal fit.

obtained from the simulation procedure described above, the quantity

$$\chi^2 = \sum_{i=0}^{n_b} \left(\frac{R_i - 0.5}{\epsilon} \right)^2 \tag{5.3}$$

obeys the χ^2 distribution with 7 degrees of freedom. As the sum of χ^2-distributed variables is also a χ^2-distributed variable with degrees of freedom summed, one can minimize the sum

$$\chi^2_{tot} = \chi^2_{x_{\mathrm{J}}} + \chi^2_{R_{AA}} \tag{5.4}$$

to obtain parameters that satisfy both distributions the best. The minimization is depicted on Fig. 5.4. The top row of Fig. 5.4 shows the scan through s, r values for x_{J} distribution only ($\chi^2_{x_{\mathrm{J}}}$), for R_{AA} only ($\chi^2_{R_{AA}}$) and their sum (χ^2_{tot}). The common minimum is clearly evident and the result of the minimization is shown on the bottom row: fit for x_{J} and R_{AA} distributions. The optimal parameter in the double fitting approach are $s = 12.5$ GeV, $r = 6$ GeV.

It seems suspicious that the optimal values for single x_{J} fitting (Fig. 5.3) and combined fitting are very different. In this way, for example, the fitting result is very dependent on the ad-hoc parameter ϵ and the two minimization are "pulling the blanket" in the total sum. Besides the s parameter which quantifies the energy loss at 100 GeV, the α parameter is also very important for this fitting. For $\alpha = 1$, the energy loss is fractional $\Delta p_{\mathrm{T}} \sim p_{\mathrm{T}}$ and the $R_{AA} = \frac{p'_{\mathrm{T}}}{p_{\mathrm{T}}}$ value is almost constant (it slowly decreases with a growing fraction of quark jets with p_{T}), but $x_{\mathrm{J}} = \frac{p'_{\mathrm{T},2}}{p'_{\mathrm{T},1}}$

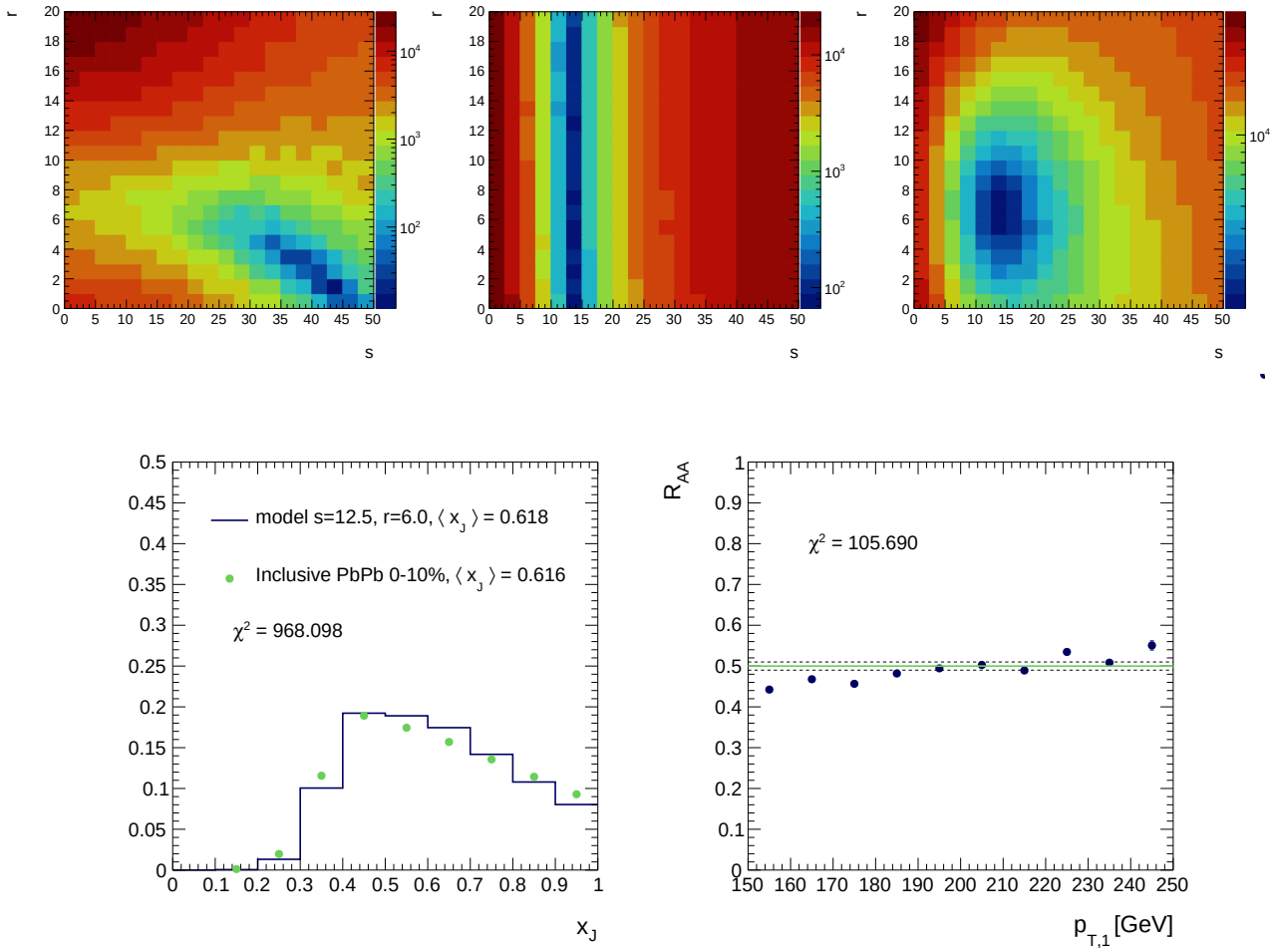

Figure 5.4: The simultaneous fitting of the energy loss parameters s and r. Optimal parameter values are $s = 12.5$ GeV, $r = 6$ GeV. Top row: χ^2 maps of fitting x_{J} (left), R_{AA} (center) and total (right). Bottom row: x_{J} (center) R_{AA} (right) distributions corresponding to the optimal fit.

distribution is unchanged with a fractional energy loss. In fact, the fraction shift was ruled out in Ref. [36] from R_{AA} fits only. The other side, $\alpha = 0$ describes the constant energy loss $\Delta p_{\mathrm{T}} = \mathrm{const}$, and results in the rise of R_{AA}. The α parameter in Ref. [36] was selected to be 0.52, which approximately corresponds to $\Delta p_{\mathrm{T}} \sim \sqrt{p_{\mathrm{T}}}$, but it is not very well constrained by the fitting as shown on Fig. 5.5.

It is clear that x_{J} distribution is very sensitive to α and it is interesting to find the minimum varying all three parameters s, r and α. This is done on fig. 5.6. The top row shows R_{AA} minimization, the middle row corresponds to x_{J} fits, while the bottom row is the total minimization. The value of the α parameter is varied

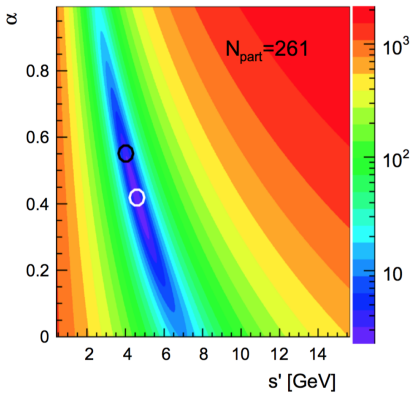

Figure 5.5: The fitting of the α and s' parameter with R_{AA} distribution from [36]. One can see that α is not very well constrained by the fit. The white circle represents the minimum value of the fit, while the black value corresponds to $\alpha = 0.55$ chosen to simplify the model.

from left to right taking the following values: 0.52,0.4,0.3,0.2,0.1 and 0. One can see that with decreasing α, the minimum of x_{J} fitting moves from the large s to reasonable range around $s = 25$ GeV. The global minimum is achieved with $\alpha = 0$ and is not very far from the minimum achieved by x_{J} fitting only.

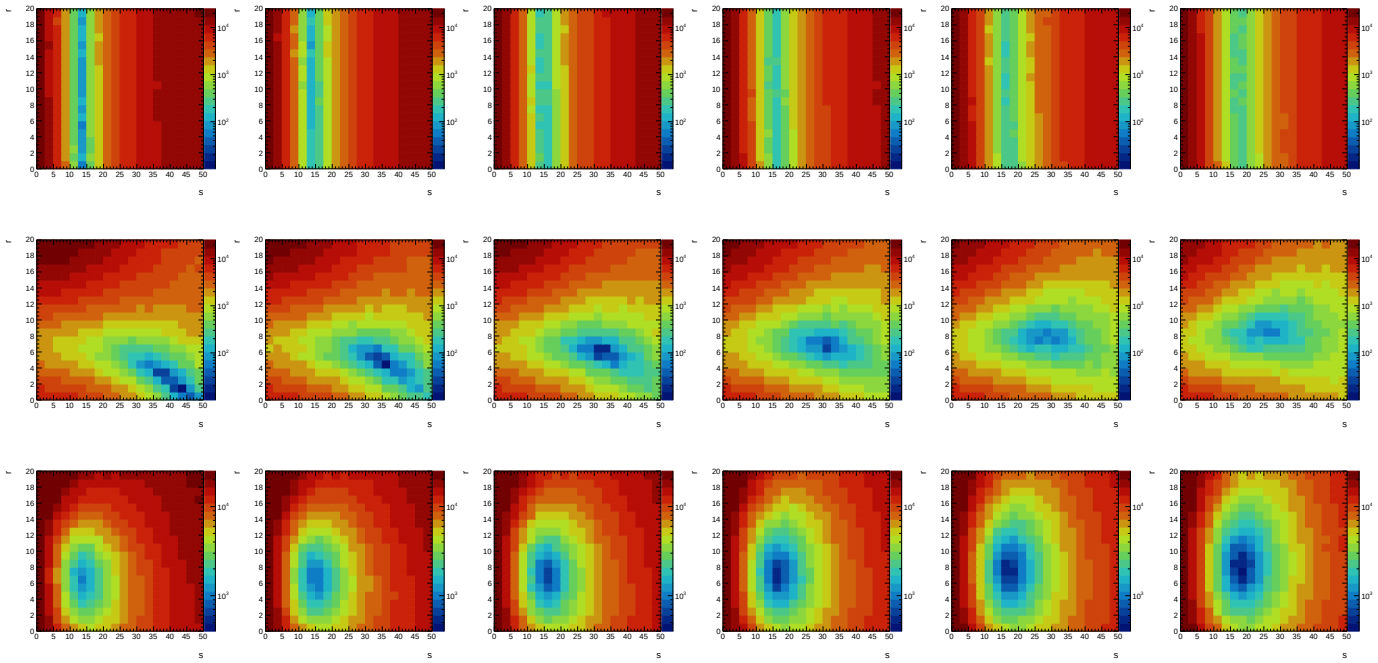

Figure 5.6: The simultaneous fitting of the energy loss parameters s and r at different values of α. From left to right: $\alpha = 0.52, 0.4, 0.3, 0.2, 0.1, 0.0$. Top row: χ^2 maps of fitting R_{AA}, middle row: x_{J}, bottom row: total. The global minimum is achieved at $\alpha = 0$.

The final fit with $\alpha = 0$ is depicted on Fig. 5.7, which has reasonable χ^2 values for both the x_{J} and R_{AA} distributions. This means that the measured x_{J} distribution suggests constant energy loss $\Delta p_{\mathrm{T}} = \mathrm{const}$. The nuclear modification factor rises

slowly with p_{T} but is still within the systematic uncertainties of measured data values (Fig. 1.19). The final values of the model after fitting both x_{J} and R_{AA} are: $s = 18$ GeV, $r = 7$ GeV, $\alpha = 0$.

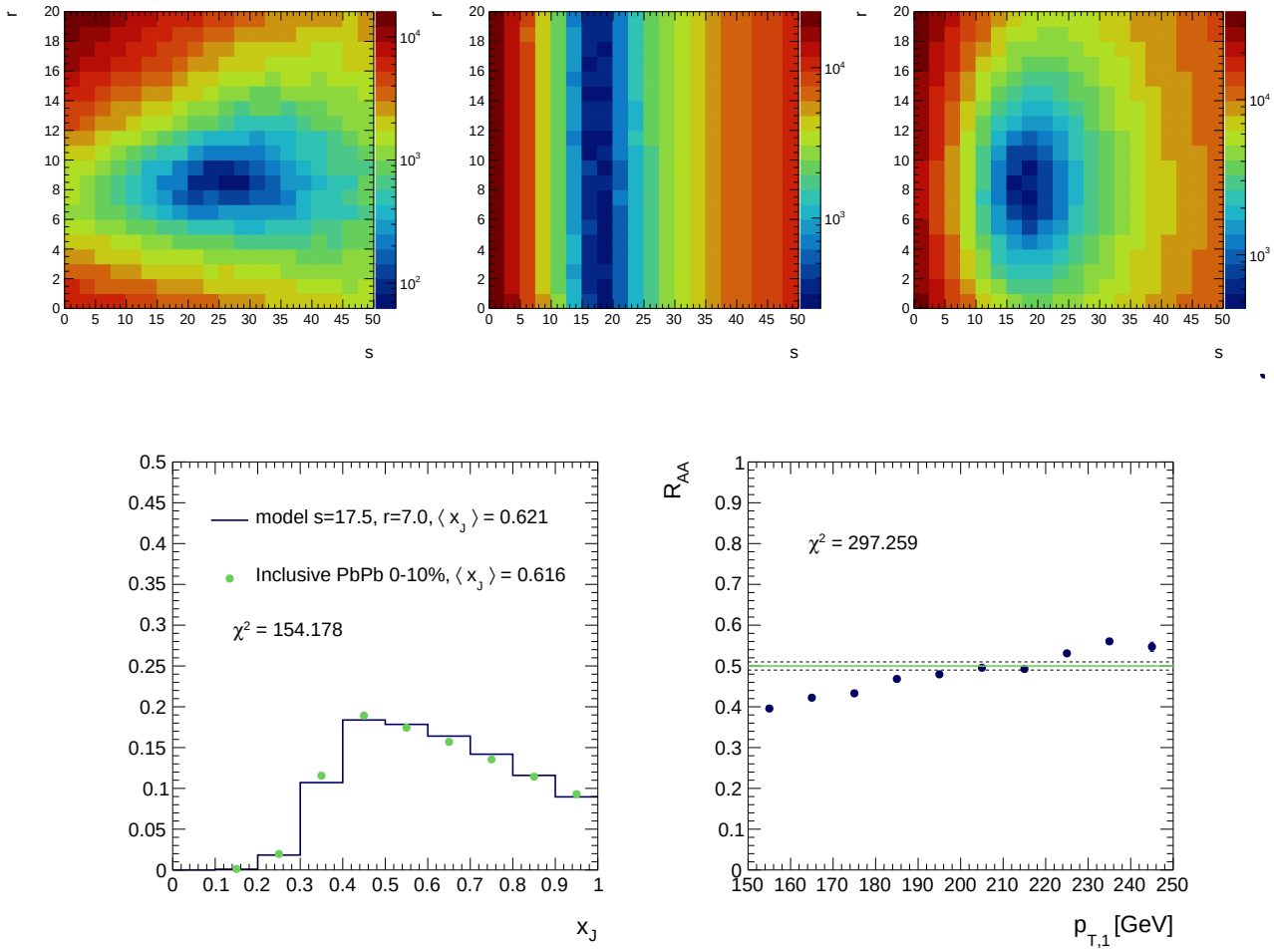

Figure 5.7: The simultaneous fitting of the energy loss parameters s and r at $\alpha = 0$. Optimal parameter values are $s = 17.5$ GeV, $r = 7$ GeV.

Once the model parameters are fixed, one can alternate the underlying assumptions to obtain insights about the physical process. One of the important assumptions was the different energy loss of quarks and gluons which lose $C_F = 1.8$ times more energy than quarks. Figure 5.8 shows the x_{J} fitting, assuming a different energy loss of quarks and gluons (same as before) and when quarks and gluons lose the same amount of energy. In the latter case, the model is clearly unable to localize the optimal parameters s and r as well as it does for the former case. Moreover, the χ^2 value of the optimal fit is much worse. This suggests that the

assumption of the different energy loss for quarks and gluons is correct.

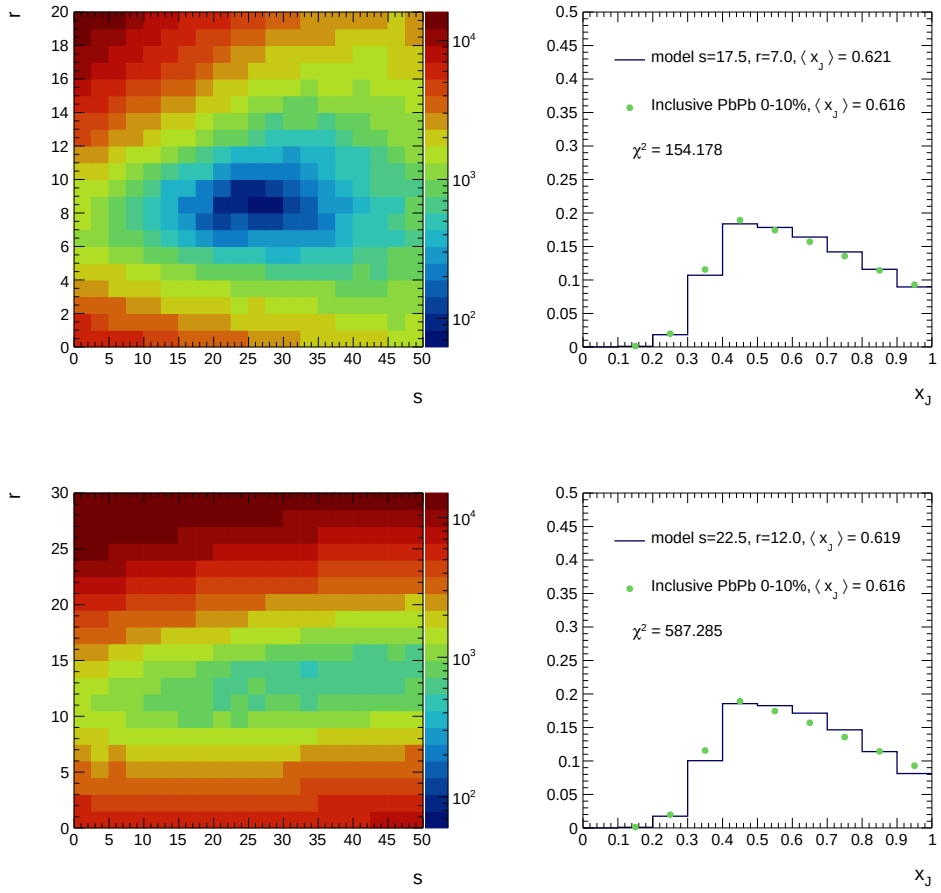

Figure 5.8: Checking the assumption of different quark and gluon energy loss. χ^2 maps of fitting x_J distribution (left) and x_J fit for optimal parameter values. Top row: $C_F = 1.8$ corresponding to different energy loss of quarks and gluons, bottom row: $C_F = 1$ which corresponds to the energy loss independent of parton type.

The model can be used to assess the energy loss parameters of b-jets from the b-jet momentum imbalance distributions. As opposed to the inclusive jet x_J, the b-jet x_J has much lower statistics hence it is not worth fitting the distributions to obtain model parameters. One can still check whether they lose energy as quarks or as gluons. Two such fits are performed and the result is shown on Fig. 5.9. The hypothesis of quark energy loss corresponds to the fit with $\chi^2 = 16.4$ and p-value $p = 0.023$, which corresponds to 2σ excess. The gluon energy loss hypothesis results in a fit with $\chi^2 = 9.3$ and $p = 0.23$ which is less than 1σ deviation. The result seems paradoxical as b-jets seem to lose energy as gluons rather than quarks. However, given the fact, that average energy loss is the same for b-jets and inclusive jets, as it was shown on Fig. 4.39, b-jets have to lose more energy on

average than light quarks since inclusive jets are mainly composed of light quarks and gluons. On the other hand, the statistical and systematical errors do not allow to rule out either of the hypotheses yet, and it is for the future analysis to answer definitively whether b-jets are quenched like light jets or not.

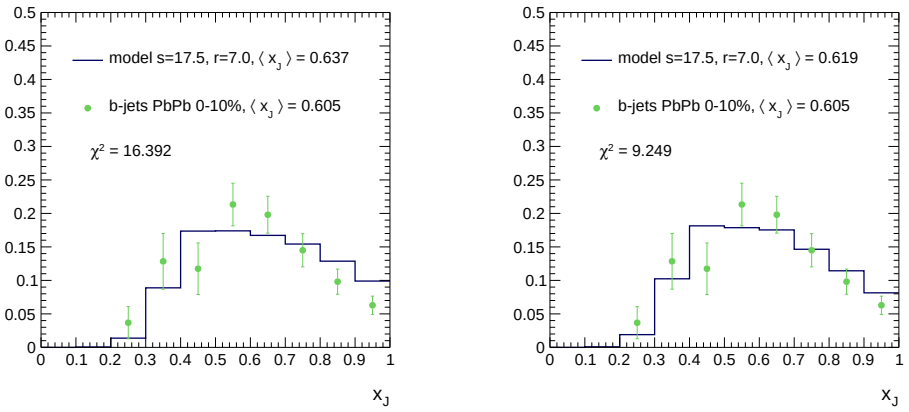

Figure 5.9: Checking whether b-jets lose energy as quarks (left) or as gluons (right).

The discussion above was based on the effective model, which may not properly describe the real energy loss. However, there are several consequences that should be correct, despite the simplicity of the model:

- the energy loss of the subleading jet is larger than the energy loss of the leading jet by a roughly constant amount,
- fitting both x_{J} and R_{AA} distributions simultaneously suggests constant energy loss $\Delta p_{\mathrm{T}} = \mathrm{const}$,
- gluons are more quenched than quarks,
- b-jets seem to lose more energy than light quark jets.

Even though the conclusions are paradoxical, it is interesting that this model can differentiate energy loss scenarios. The most important conclusion from this exercise is that the transverse momentum imbalance x_{J} and the nuclear modification factor R_{AA} are complementary sources of information about jet quenching. In order to obtain a stronger message about b-jet energy loss one needs to improve the analysis in order to collect more data.

5.2 Future improvements

The analysis described in Chapter 4 describes the measurement of b-jet imbalance for the first time. However, it does not utilize the full potential of the data provided by the LHC. There are several improvements that still can be made to reinforce the resulting message.

Upgrading the tagger. The current CSV tagger, based on the simple likelihood combinations as described in Sec. 3.3, is not the best tool available at the moment for the tagging of b-jets. The upgraded version CSVv2 based on multivariate combination of discriminating distributions performs better than the current tagger in pp collisions. The performance of the upgraded tagger was checked in PbPb collisions and it turned out to be even worse than the likelihood-based version. This suggests that the multivariate tagger must be properly retrained as the underlying distributions are different in pp and PbPb reconstructions. According to studies in pp, this procedure is expected to increase the efficiency by 10% at a given purity.

Selecting a looser working point. In this analysis, the working point of CSV = 0.9 was chosen to ensure the pure sample of b-dijets. However, the systematic error associated to the mistagged pair of jets is very small according to Tab. 4.3. It means that one can relax the b-tagging selection to increase the number of events selected without a significant impact on the systematic error. The variation of the CSV working point was performed in the range of values between 0 and 1 and the mean x_{J} as a function of working point is shown on Fig. 5.10. Each point on the plot corresponds to the different b-tagging selection and required re-derivation of efficiency corrections. The result is not significantly dependent on the working point value in the reasonable variation in the 0.7-0.95 range. As a result, one can loosen slightly the working point, e.g. to the value of 0.8. According to the ROC-curve in fig. 3.26, this can add up to 50% in statistics.

Improvement of jet energy scale systematics. As presented in Tab. 4.2 and 4.3, the largest systematic error associated to this measurement comes from the uncertainty of the jet energy scale. This is mainly a consequence of the im-

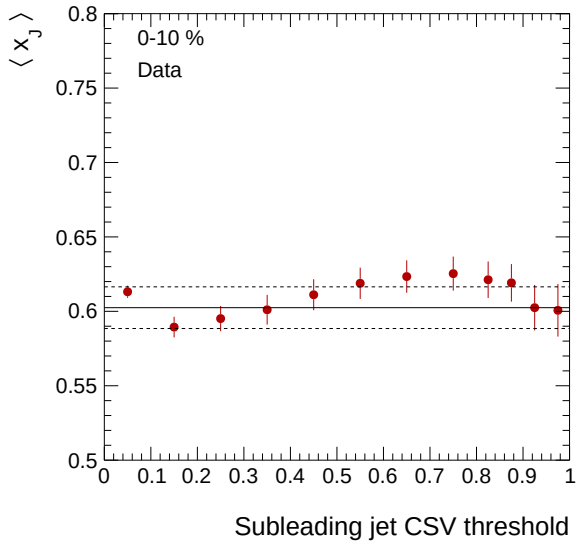

Figure 5.10: Mean x_J values for different CSV working point selection. Dashed lines correspond to the systematic uncertainty associated to b-tagging.

perfect underlying subtraction mechanism employed. More advanced techniques, such as constituent subtraction method [133], are going to be validated soon to improve the reconstruction of jets.

Extending the pseudorapidity range. The CMS detector allows to measure b-jets with R=0.4 in the $|\eta| < 2$ range, but the presented analysis only uses jets in the $|\eta| < 1.5$ range. This restriction was necessary because the increased granularity of the CMS calorimeters in the endcaps results in the different jet energy scale as in the barrel region. A more detailed analysis of the η-dependence of the jet energy scale will help to expand the pseudorapidity region and increase the number of dijets by around 20%.

In total, the improvements described above allow to increase the statistics by a factor of two and to reduce the systematic uncertainties. The measurement of b-dijet momentum imbalance will be repeated in 2018 run of heavy ions at LHC and by that time the CMS detector will be ungraded. A substantial upgrade which affects significantly the b-jet reconstruction performance is the inclusion of a 4th pixel layer in the tracker [37]. In the upgraded detector, the innermost layer will be located closer to the beamline than in the current detector. This has an immediate consequence of the improved transverse and longitudinal impact parameter

resolution and vertex resolution which are crucial for b-tagging. Additionally, the upgrade will affect the total efficiency and fake rate of the tracking, as the seeding step of the tracking is mostly based on pixels. Moreover, the 4th layer will significantly decrease the combinatorial combinations possible with 3 pixels only, which results in the improved dependence of the tracking performance on the pile-up (Fig. 5.11). The PbPb event can be considered as a pile-up pp event with all tracks originating from the same vertex, hence one expects that the pixel upgrade will mitigate the difference between pp and PbPb reconstruction. As a consequence, this will improve the jet response since jets are made from particle flow objects which rely on tracks. Altogether, upgrading pixel detector will result in a 30% increase of b-tagging efficiency (Fig. 5.12) at current purity rates and will significantly boost the statistical precision of the future b-jet analyses.

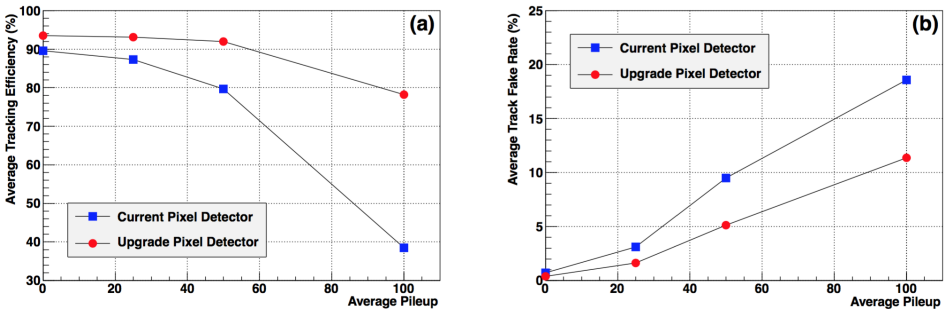

Figure 5.11: Efficiency (left) and fake rate (right) as a function of the average pileup for the current pixel detector (blue squares) and for the upgraded pixel detector (red dots) [37]

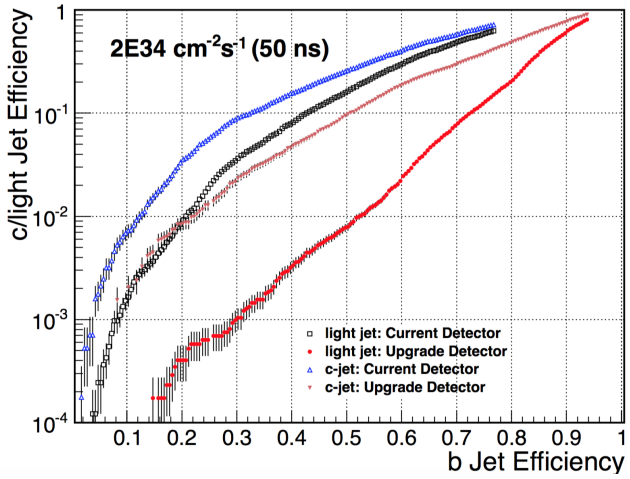

Figure 5.12: Performance of the Combined Secondary Vertex b-tagging algorithm for jets with $p_T >$ 30 GeV in pp events with an average pileup of 100 [37].

The imbalance of dijet transverse momentum complements the nuclear modification factor measurement. Together they can constrain energy loss scenarios and

reveal underlying parton energy loss differences. In this chapter, the properties of energy loss were examined using the simple energy loss model. As a consequence it was established that energy loss is independent on the transverse momentum and confirmed the assumption of different energy loss between quarks and gluons. Surprisingly, the model seems to prefer the hypothesis that b-jets loose energy as gluons rather than quarks. Such a conclusion was also made by the authors of the model from the b-jet R_{AA} fits in the Ref. [144]. We remind that in the spectra measurement the vast proportion of b-jets originate from gluons (via the gluon splitting mechanism). On contrary, b-dijet imbalance consist mostly of primary b-jet pairs. So far, the statistical precision does not allow the model to provide the definitive conclusion about the b-jet energy loss. The number of improvements in the analysis and the detector upgrade will significantly boost the precision of the measurement in the close future. Summarizing, the next PbPb run will provide spectacular measurements of inclusive and b-jet quenching and clarify the underlying parton energy loss mechanism.

Summary

The measurement of the transverse momentum imbalance of b-jets and inclusive (non-identified) jets in pp and PbPb collisions at $\sqrt{s_{NN}} = 5.02$ TeV has been performed for the first time. In order to do that, data from the LHC corresponding to integrated luminosity of 404 μb^{-1} for PbPb collisions and 25.8 pb^{-1} for pp collisions has been recorded by CMS and analyzed. This measurement raises challenges to object reconstruction which were overcome during the long shutdown period between run 1 and run 2 of LHC. Additionally, the dedicated b-jet trigger has been developed to record all events with leading b-tagged jet.

The quenching is observed via the increasing imbalance of dijets with increasing collisions centrality. The energy loss of b-jets is observed to be compatible with the one of inclusive jets for the kinematic selection applied in this analysis: transverse momentum above 100 GeV for the leading jet and 40 GeV for the subleading jet. The current measurement of b-jets is superior to the previous results since the requirement of back-to-back b-jets selects mostly primary b-jets from the flavor creation mechanism, as it was verified by flavor process reweighting studies. Since b-jet pairs originate from b-quarks while inclusive jet originate mostly from the mix of light quarks and gluons, this measurement constraints the difference between quark and gluon energy loss mechanisms.

The future work will aim to improve this measurement by refining the b-jet identification procedure, while additional studies of the jet energy scale in CMS detector should decrease the systematic errors. Finally, the next period of PbPb collisions of LHC will provide sufficient statistics to highlight possible dependence of jet quenching on the parton flavor.

Bibliography

[1] S. Bethke, "Experimental tests of asymptotic freedom", *Prog. Part. Nucl. Phys.* **58** (2007) 351–386, arXiv:hep-ex/0606035.

[2] **BMW** Collaboration, S. Durr *et al.*, "Ab-Initio Determination of Light Hadron Masses", *Science* **322** (2008) 1224–1227, arXiv:0906.3599.

[3] N. Cardoso and P. Bicudo, "Lattice QCD computation of the SU(3) String Tension critical curve", *Phys. Rev.* **D85** (2012) 077501, arXiv:1111.1317.

[4] M. Cardoso, N. Cardoso, and P. Bicudo, "Lattice QCD computation of the colour fields for the static hybrid quark-gluon-antiquark system, and microscopic study of the Casimir scaling", *Phys. Rev.* **D81** (2010) 034504, arXiv:0912.3181.

[5] **Wuppertal-Budapest** Collaboration, S. Borsanyi, Z. Fodor, *et al.*, "Is there still any T_c mystery in lattice QCD? Results with physical masses in the continuum limit III", *JHEP* **09** (2010) 073, arXiv:1005.3508.

[6] F. Karsch, E. Laermann, and A. Peikert, "The Pressure in two flavor, (2+1)-flavor and three flavor QCD", *Phys. Lett.* **B478** (2000) 447–455, arXiv:hep-lat/0002003.

[7] H. Satz, "The Thermodynamics of Quarks and Gluons", *Lect. Notes Phys.* **785** (2010) 1–21, arXiv:0803.1611.

[8] M. L. Miller, K. Reygers, S. J. Sanders, and P. Steinberg, "Glauber modeling in high energy nuclear collisions", *Ann. Rev. Nucl. Part. Sci.* **57** (2007) 205–243, arXiv:nucl-ex/0701025.

[9] **CMS** Collaboration, "Dependence on pseudorapidity and centrality of charged hadron production in PbPb collisions at a nucleon-nucleon centre-of-mass energy of 2.76 TeV", *JHEP* **08** (2011) 141, arXiv:1107.4800.

[10] G.-Y. Qin, J. Ruppert, C. Gale, S. Jeon, G. D. Moore, and M. G. Mustafa, "Radiative and collisional jet energy loss in the quark-gluon plasma at RHIC", *Phys. Rev. Lett.* **100** (2008) 072301, arXiv:0710.0605.

[11] **STAR** Collaboration, J. Adams *et al.*, "Evidence from d + Au measurements for final state suppression of high p_{T} hadrons in Au+Au collisions at RHIC", *Phys. Rev. Lett.* **91** (2003) 072304, arXiv:nucl-ex/0306024.

[12] **PHENIX** Collaboration, S. S. Adler *et al.*, "Suppressed π^0 production at large transverse momentum in central AuAu collisions at $\sqrt{s_{NN}} = 200$ GeV", *Phys. Rev. Lett.* **91** (2003) 072301, arXiv:nucl-ex/0304022.

[13] **CMS Collaboration** Collaboration, S. Chatrchyan *et al.*, "Study of z boson production in pbpb collisions at $\sqrt{s_{NN}} = 2.76$ TeV", *Phys. Rev. Lett.* **106** May (2011) 212301.

[14] **CMS** Collaboration, S. Chatrchyan *et al.*, "Study of W boson production in PbPb and pp collisions at $\sqrt{s_{NN}} = 2.76$ TeV", *Phys. Lett.* **B715** (2012) 66–87, arXiv:1205.6334.

[15] **CMS Collaboration** Collaboration, S. Chatrchyan *et al.*, "Measurement of isolated photon production in pp and PbPb collisions at $\sqrt{s_{NN}} = 2.76$ TeV", *Phys. Lett. B* **710** Jan (2012) 256–277. 33 p.

[16] **CMS Collaboration** Collaboration, S. Chatrchyan *et al.*, "Study of high-p_T charged particle suppression in PbPb compared to pp collisions at $\sqrt{s_{NN}}$=2.76 TeV", *Eur. Phys. J. C* **72** Feb (2012) 1945. 33 p.

[17] **CMS Collaboration** Collaboration, "J/psi results from CMS in PbPb collisions, with 150mub-1 data", Tech. Rep. CMS-PAS-HIN-12-014, CERN, Geneva, 2012.

[18] M. Cacciari, G. P. Salam, and G. Soyez, "The anti-k$_T$ jet clustering algorithm", *Journal of High Energy Physics* **2008** (2008), no. 04, 063.

[19] **CMS** Collaboration, "Nuclear modification factor of high transverse momentum jets in PbPb collisions at $\sqrt{s_{\mathrm{NN}}} = 2.76$ TeV", Tech. Rep. CMS-PAS-HIN-12-004, 2012.

[20] **CMS** Collaboration, "Jet momentum dependence of jet quenching in PbPb collisions at $\sqrt{s_{NN}} = 2.76$ TeV", *Phys. Lett. B* **712** (2012) 176, arXiv:1202.5022.

[21] **ALICE** Collaboration, C. Jena, "Measurement of D-meson production in pp, p-Pb, and Pb-Pb collisions at the LHC with the ALICE detector", *J. Phys. Conf. Ser.* **535** (2014) 012027, arXiv:1407.7897.

[22] **CMS** Collaboration, "Evidence of b-Jet Quenching in PbPb Collisions at $\sqrt{s_{NN}} = 2.76$ TeV", *Phys. Rev. Lett.* **113** (2014) 132301, arXiv:1312.4198.

[23] F. Marcastel, "CERN's Accelerator Complex. La chaine des accelerateurs du CERN", Oct 2013, https://cds.cern.ch/record/1621583.

[24] "Cms luminosity results". twiki.cern.ch/twiki/bin/view/CMSPublic/LumiPublicResults.

[25] T. Sakuma and T. McCauley, "Detector and Event Visualization with SketchUp at the CMS Experiment", *J. Phys. Conf. Ser.* **513** (2014) 022032, arXiv:1311.4942.

[26] **CMS** Collaboration, "Description and performance of track and primary-vertex reconstruction with the CMS tracker", *J. Instrum.* **9** May (2014) P10009. 80 p.

[27] **CMS** Collaboration, G. L. Bayatian *et al.*, "CMS physics: Technical design report", Tech. Rep. CMS-TDR-008-1, 2006.

[28] **CMS** Collaboration, "Measurement of cross section and nuclear modification factor of B meson using fully reconstructed $B^+ \to J/\psi + K^+$

decay channel with CMS 2015 pp and PbPb collision data", Tech. Rep. CMS-HIN-16-011, CERN, Geneva, 2010.

[29] **CMS** Collaboration, S. R. Davis, "Interactive Slice of the CMS detector". `https://cds.cern.ch/record/2205172`, Aug 2016.

[30] **CMS** Collaboration, "Particle-flow event reconstruction in CMS and performance for jets, taus, and MET", CMS Physics Analysis Summary CMS-PAS-PFT-09-001, CERN, 2009.

[31] **CMS** Collaboration, M. Nguyen, "Jet Reconstruction with Particle Flow in Heavy-Ion Collisions with CMS", *J. Phys.* **G38** (2011) 124151, `arXiv:1107.0179`.

[32] O. Kodolova, I. Vardanian, A. Nikitenko, and A. Oulianov, "The performance of the jet identification and reconstruction in heavy ions collisions with CMS detector", *Eur. Phys. J. C* **50** (2007) 117.

[33] **CMS** Collaboration, "Identification of b-quark jets with the CMS experiment", *JINST* **8** (2013) P04013, `arXiv:1211.4462`.

[34] **CMS** Collaboration, "Identification of b quark jets at the CMS Experiment in the LHC Run 2", CMS Physics Analysis Summary CMS-PAS-BTV-15-001, CERN, 2016.

[35] **CMS** Collaboration, "Measurement of the charged particle nuclear modification factor in PbPb collisions at $\sqrt{s_{\mathrm{NN}}} = 5.02$ TeV", Tech. Rep. CMS-PAS-HIN-15-015, CERN, Geneva, 2016.

[36] M. Spousta and B. Cole, "Interpreting single jet measurements in Pb + Pb collisions at the LHC", *Eur. Phys. J.* **C76** (2016), no. 2, 50, `arXiv:1504.05169`.

[37] A. Dominguez, D. Abbaneo, *et al.*, "CMS Technical Design Report for the Pixel Detector Upgrade", Tech. Rep. CERN-LHCC-2012-016. CMS-TDR-11, Sep 2012.

[38] E. Rutherford, "The scattering of alpha and beta particles by matter and the structure of the atom", *Phil. Mag.* **21** (1911) 669–688.

[39] E. Rutherford, "Collision of α particles with light atoms; 4, an anomalous effect in nitrogen", *Philos. Mag.* **37** (1919) 581.

[40] J. Chadwick, "Possible Existence of a Neutron", *Nature* **129** (1932) 312.

[41] C. D. Anderson, "The Apparent Existence of Easily Deflectable Positives", *Science* **76** (1932) 238–239.

[42] E. Noether, "Invariante Variationsprobleme", *Nachr. Akad. Wiss. Göttingen, II*, 1918, no. 2, 235–257.

[43] T. Aoyama, M. Hayakawa, T. Kinoshita, and M. Nio, "Tenth-Order QED Contribution to the Electron g-2 and an Improved Value of the Fine Structure Constant", *Phys. Rev. Lett.* **109** (2012) 111807, `arXiv:1205.5368`.

[44] H. A. Bethe, "The Electromagnetic shift of energy levels", *Phys. Rev.* **72** (1947) 339–341.

[45] A. Zee, "Quantum Field Theory in a Nutshell", Princeton Univ. Press, Princeton, NJ, 2003.

[46] K. G. Wilson and J. B. Kogut, "The Renormalization group and the epsilon expansion", *Phys. Rept.* **12** (1974) 75–200.

[47] B. Delamotte, "A hint of renormalization", *Am. J. Phys.* **72** Dec (2002) 170–184. 10 p, Comments: 17 pages, pedagogical article.

[48] S. Banerjee and S. N. Ganguli, "Estimation of the QED coupling constant α at $\sqrt{s} = \mathrm{M}_Z$", *Z. Phys. C* **57** Sep (1992) 229–232. 8 p.

[49] M. E. Peskin and D. V. Schroeder, "An Introduction to Quantum Field Theory; 1995 ed.", Westview, Boulder, CO, 1995.

[50] M. Gell-Mann, "A schematic model of baryons and mesons", *Physics Letters* **8** (1964), no. 3, 214 – 215.

[51] G. Zweig, "An SU_3 model for strong interaction symmetry and its breaking; Version 2", Feb 1964.

[52] H. Yukawa, "On the interaction of elementary particles. I.", *Proc. Phys. Math. Soc. Jpn.* **17** (1935) 48–57.

[53] A. Zee, "Group theory in a nutshell for physicists", Princeton University Press, Princeton, NJ, 2016.

[54] A. Jaffe and E. Witten, "Quantum yang-mills theory". `http://www.claymath.org/sites/default/files/yangmills.pdf`.

[55] **Particle Data Group** Collaboration, K. A. Olive *et al.*, "Review of Particle Physics", *Chin. Phys.* **C38** (2014) 090001.

[56] P. Dirac, "The lagrangian in quantum mechanics", *Physikalische Zeitschrift der Sowjetunion* **3** (1933) 64–72.

[57] R. P. Feynman, "Space-time approach to non-relativistic quantum mechanics", *Rev. Mod. Phys.* **20** Apr (1948) 367–387.

[58] W. K. Hastings, "Monte carlo sampling methods using markov chains and their applications", *Biometrika* **57** (1970), no. 1, 97–109, `http://biomet.oxfordjournals.org/cgi/reprint/57/1/97.pdf`.

[59] K. G. Wilson, "Confinement of quarks", *Phys. Rev. D* **10** Oct (1974) 2445–2459.

[60] C. Gattringer and C. B. Lang, "Quantum chromodynamics on the lattice", *Lect. Notes Phys.* **788** (2010) 1–343.

[61] E. V. Shuryak, "Quark-Gluon Plasma and Hadronic Production of Leptons, Photons and Psions", *Phys. Lett.* **B78** (1978) 150, [Yad. Fiz.28,796(1978)].

[62] J. D. Bjorken, "Highly relativistic nucleus-nucleus collisions: The central rapidity region", *Phys. Rev. D* **27** Jan (1983) 140–151.

[63] **PHENIX** Collaboration, K. Adcox, S. Adler, *et al.*, "Formation of dense partonic matter in relativistic nucleus nucleus collisions at rhic:

Experimental evaluation by the phenix collaboration", *Nuclear Physics A* **757** (2005), no. 1, 184 – 283.

[64] **CMS** Collaboration, S. Chatrchyan *et al.*, "Measurement of the pseudorapidity and centrality dependence of the transverse energy density in PbPb collisions at $\sqrt{s_{NN}} = 2.76$ TeV", *Phys. Rev. Lett.* **109** (2012) 152303, arXiv:1205.2488.

[65] R. Glauber, "Lectures in theoretical physics", 1:315 ed.WEBrittin, LGDunham New York: Interscience, 1959.

[66] W. X. Nian and M. Gyulassy, "HIJING: a Monte Carlo model for multiple jet production in pp, pA, and AA collisions", *Phys. Rev. D* **44** Jul (1991) 3501–3516. 56 p.

[67] D. G. d'Enterria, "Hard scattering cross-sections at LHC in the Glauber approach: From pp to pA and AA collisions", arXiv:nucl-ex/0302016.

[68] D. d'Enterria, "Jet quenching", *Landolt-Bornstein* **23** (2010) 471, arXiv:0902.2011.

[69] S. Peigne and A. V. Smilga, "Energy losses in a hot plasma revisited", *Phys. Usp.* **52** (2009) 659–685, arXiv:0810.5702.

[70] Y. L. Dokshitzer and D. E. Kharzeev, "Heavy quark colorimetry of QCD matter", *Phys. Lett.* **B519** (2001) 199–206, arXiv:hep-ph/0106202.

[71] **CMS** Collaboration, "Observation and studies of jet quenching in PbPb collisions at nucleon-nucleon center-of-mass energy $\sqrt{s_{\mathrm{NN}}} = 2.76$ TeV", *Phys. Rev. C* **84** (2011) 024906, arXiv:1102.1957.

[72] **CMS Collaboration** Collaboration, S. Chatrchyan *et al.*, "Measurement of jet fragmentation in PbPb and pp collisions at $\sqrt{s_{NN}} = 2.76$ TeV", *Phys. Rev. C* **90** Jun (2014) 024908. 33 p, Replaced with published version. Added journal reference and DOI.

[73] R. D. Field, "The Sources of b quarks at the Tevatron and their correlations", *Phys. Rev.* **D65** (2002) 094006, arXiv:hep-ph/0201112.

[74] J. D. Bjorken, "Energy Loss of Energetic Partons in Quark - Gluon Plasma: Possible Extinction of High p_{T} Jets in Hadron - Hadron Collisions", 1982.

[75] G. Hanson, G. S. Abrams, *et al.*, "Evidence for jet structure in hadron production by e^+e^- annihilation", *Phys. Rev. Lett.* **35** Dec (1975) 1609–1612.

[76] G. Altarelli and G. Parisi, "Asymptotic Freedom in Parton Language", *Nucl. Phys.* **B126** (1977) 298–318.

[77] G. P. Salam and G. Soyez, "A practical Seedless Infrared-Safe Cone jet algorithm", *JHEP*, 2007 0705, 086.

[78] M. Cacciari and G. P. S. et al., "Fastjet 2.4.1 user manual".

[79] S. D. Ellis and D. E. Soper, "Successive combination jet algorithm for hadron collisions", *Phys. Rev.* **D48** (1993) 3160–3166, arXiv:hep-ph/9305266.

[80] Y. L. Dokshitzer, G. D. Leder, S. Moretti, and B. R. Webber, "Better jet clustering algorithms", *JHEP* **08** (1997) 001, arXiv:hep-ph/9707323.

[81] **ALICE** Collaboration, R. Reed, "Full Jet Reconstruction in 2.76 TeV pp and Pb-Pb collisions in the ALICE experiment", *J. Phys. Conf. Ser.* **446** (2013) 012006, arXiv:1304.5945.

[82] **ATLAS** Collaboration, G. Aad *et al.*, "Measurements of the Nuclear Modification Factor for Jets in Pb+Pb Collisions at $\sqrt{s_{\mathrm{NN}}} = 2.76$ TeV with the ATLAS Detector", *Phys. Rev. Lett.* **114** (2015), no. 7, 072302, arXiv:1411.2357.

[83] **ATLAS** Collaboration, G. Aad, B. Abbott, *et al.*, "Observation of a centrality-dependent dijet asymmetry in lead-lead collisions at $\sqrt{s_{\mathrm{NN}}} = 2.76$ TeV with the atlas detector at the lhc", *Phys. Rev. Lett.* **105** Dec (2010) 252303.

[84] J. G. Milhano and K. C. Zapp, "Origins of the di-jet asymmetry in heavy ion collisions", *Eur. Phys. J.* **C76** (2016), no. 5, 288, arXiv:1512.08107.

[85] **CMS** Collaboration, "Measurement of transverse momentum relative to dijet systems in PbPb and pp collisions at $\sqrt{s_{NN}} = 2.76$ TeV", *JHEP* **01** (2016) 006, arXiv:1509.09029.

[86] **CMS** Collaboration, "Transverse momentum spectra of inclusive b jets in pPb collisions at $\sqrt{s_{NN}} = 5.02$ TeV", *Phys. Lett. B* **754** (2016) 59–80, arXiv:1510.03373.

[87] J. Coupard, H. Damerau, *et al.*, "LHC Injectors Upgrade, Technical Design Report, Vol. II: Ions", Tech. Rep. CERN-ACC-2016-0041, CERN, Geneva, Apr 2016.

[88] **CMS** Collaboration, V. Karimaki, M. Mannelli, *et al.*, "The CMS tracker system project: Technical Design Report", CERN, Geneva, 1997.

[89] **CMS** Collaboration, "The CMS electromagnetic calorimeter project: Technical Design Report", CERN, Geneva, 1997.

[90] P. Adzic, "Energy resolution of the barrel of the cms electromagnetic calorimeter", *Journal of Instrumentation* **2** (2007), no. 04, P04004.

[91] **CMS** Collaboration, "The CMS hadron calorimeter project: Technical Design Report", CERN, Geneva, 1997.

[92] **CMS** Collaboration, E. Gulmez, "Phase1 upgrade of the CMS-HF Calorimeter", Tech. Rep. CMS-CR-2016-145, CERN, Geneva, Jun 2016.

[93] H. S. Budd, "CMS central hadron calorimeter", *Nucl. Phys. Proc. Suppl.* **54B** (1997) 191–197, arXiv:hep-ex/0102032.

[94] **CMS** Collaboration, "The CMS muon project: Technical Design Report", CERN, Geneva, 1997.

[95] **CMS** Collaboration, A. Tapper and D. Acosta, "CMS Technical Design Report for the Level-1 Trigger Upgrade", Tech. Rep. CERN-LHCC-2013-011. CMS-TDR-12, Jun 2013.

[96] **CMS** Collaboration, W. Adam *et al.*, "The CMS high level trigger", *Eur. Phys. J.* **C46** (2006) 605–667, arXiv:hep-ex/0512077.

[97] C. Eck, J. Knobloch, *et al.*, "LHC computing Grid: Technical Design Report. Version 1.06 (20 Jun 2005)", CERN, Geneva, 2005.

[98] **CMS Collaboration** Collaboration, G. L. Bayatyan, M. Della Negra, Foà, A. Hervé, and A. Petrilli, "CMS computing: Technical Design Report", CERN, Geneva, 2005. Submitted on 31 May 2005.

[99] T. D. Lee and M. Nauenberg, "Degenerate systems and mass singularities", *Phys. Rev.* **133** Mar (1964) B1549–B1562.

[100] T. Sjostrand, P. Eden, *et al.*, "High-energy physics event generation with PYTHIA 6.1", *Comput. Phys. Commun.* **135** (2001) 238–259, arXiv:hep-ph/0010017.

[101] G. Corcella, I. G. Knowles, *et al.*, "HERWIG 6.5 release note", arXiv:hep-ph/0210213.

[102] S. Catani, F. Krauss, *et al.*, "QCD matrix elements + parton showers", *JHEP* **11** (2001) 063, arXiv:hep-ph/0109231.

[103] B. Andersson, G. Gustafson, G. Ingelman, and T. Sjöstrand, "Parton fragmentation and string dynamics", *Physics Reports* **97** (1983), no. 2, 31 – 145.

[104] T. Sjostrand, "Monte Carlo Generators", in "High-energy physics. Proceedings, European School, Aronsborg, Sweden, June 18-July 1, 2006", pp. 51–74. 2006. arXiv:hep-ph/0611247.

[105] T. Sjöstrand, S. Mrenna, and P. Skands, "PYTHIA 6.4 physics and manual", *JHEP* **05** (2006) 026, arXiv:hep-ph/0603175.

[106] T. Sjostrand, S. Mrenna, and P. Z. Skands, "A Brief Introduction to PYTHIA 8.1", *Comput. Phys. Commun.* **178** (2008) 852–867, arXiv:0710.3820.

[107] J. Bjorken *Beam Line* **22** (1992), no. 4,.

[108] I. P. Lokhtin and A. M. Snigirev, "A Model of jet quenching in ultrarelativistic heavy ion collisions and high-p_{T} hadron spectra at RHIC", *Eur. Phys. J. C* **45** (2006) 211, arXiv:hep-ph/0506189.

[109] I. P. Lokhtin, L. V. Malinina, *et al.*, "Heavy ion event generator HYDJET++ (HYDrodynamics plus JETs)", *Comput. Phys. Commun.* **180** (2009) 779–799, arXiv:0809.2708.

[110] M. Cacciari, J. Rojo, G. P. Salam, and G. Soyez, "Jet Reconstruction in Heavy Ion Collisions", *Eur. Phys. J.* **C71** (2011) 1539, arXiv:1010.1759.

[111] **GEANT4** Collaboration, S. Agostinelli *et al.*, "GEANT4: A Simulation toolkit", *Nucl. Instrum. Meth.* **A506** (2003) 250–303.

[112] **CMS** Collaboration, "Precise Mapping of the Magnetic Field in the CMS Barrel Yoke using Cosmic Rays", *JINST* **5** (2010) T03021, arXiv:0910.5530.

[113] R. E. Kalman, "A new approach to linear filtering and prediction problems", *Transactions of the ASME–Journal of Basic Engineering* **82** (1960), no. Series D, 35–45.

[114] P. Billoir, "Progressive track recognition with a kalman-like fitting procedure", *Computer Physics Communications* **57** (1989), no. 1, 390 – 394.

[115] R. Frühwirth, "Application of kalman filtering to track and vertex fitting", *Nuclear Instruments and Methods in Physics Research Section A: Accelerators, Spectrometers, Detectors and Associated Equipment* **262** (1987), no. 2, 444 – 450.

[116] H. Bethe, "Experimental nuclear physics", vol. 1. John Wiley, 1953.

[117] **CMS** Collaboration, "Commissioning and Performance of the CMS Pixel Tracker with Cosmic Ray Muons", *J. Instrum.* **5** Nov (2009) T03007. 37 p.

[118] **CMS** Collaboration, "Measurement of Tracking Efficiency", Tech. Rep. CMS-PAS-TRK-10-002, CERN, 2010.

[119] T. W. Anderson, ed., "An introduction to multivariate statistical analysis", Wiley, 1984.

[120] L. Breiman, J. Friedman, R. Olshen, and C. Stone, "Classification and Regression Trees", Wadsworth and Brooks, Monterey, CA, 1984.

[121] J. R. Quinlan, "Induction of decision trees", *MACH. LEARN* **1** (1986) 81–106.

[122] J. R. Quinlan, "C4.5: Programs for machine learning", Morgan Kaufmann Publishers Inc., San Francisco, CA, USA, 1993.

[123] L. Breiman, "Random forests", *Machine Learning* **45** (2001), no. 1, 5–32.

[124] Y. Freund and R. E. Schapire, "Experiments with a new boosting algorithm", in "Proceedings of the Thirteenth International Conference on Machine Learning (ICML 1996)", L. Saitta, ed., pp. 148–156. Morgan Kaufmann, 1996.

[125] J. H. Friedman, "Greedy function approximation: A gradient boosting machine", *Annals of Statistics* **29** (2000) 1189–1232.

[126] X. Wu, V. Kumar, *et al.*, "Top 10 algorithms in data mining", *Knowledge and Information Systems* **14** (2008), no. 1, 1–37.

[127] J. C. Brient, "Improving the jet reconstruction with the particle flow method: An introduction", in "Calorimetry in particle physics. Proceedings, 11th International Conference, CALOR 2004, Perugia, Italy, March 29-April 2, 2004", pp. 445–451. 2004.

[128] H. Videau, "Energy flow or Particle flow - The technique of "energy flow" for pedestrians", in "International Conference on Linear Colliders - LCWS04", J.-C. Videau, H.; Brient, ed., pp. 105–120. Ecole Polytechnique Palaiseau, Paris, France, 2004.

[129] **CMS** Collaboration, F. Beaudette, "The CMS Particle Flow Algorithm", in "Proceedings, International Conference on Calorimetry for the High

Energy Frontier (CHEF 2013): Paris, France, April 22-25, 2013", pp. 295–304. 2013. arXiv:1401.8155.

[130] H. Bethe and W. Heitler, "On the stopping of fast particles and on the creation of positive electrons", *Proceedings of the Royal Society of London A: Mathematical, Physical and Engineering Sciences* **146** (1934), no. 856, 83–112.

[131] W. Adam, R. Frühwirth, A. Strandlie, and T. Todorov, "Reconstruction of electrons with the gaussian-sum filter in the cms tracker at the lhc", *Journal of Physics G: Nuclear and Particle Physics* **31** (2005), no. 9, N9.

[132] **CMS** Collaboration, "Underlying-Event Subtraction for Particle Flow", Tech. Rep. CMS-DP-2013-018, Jun 2013.

[133] P. Berta, M. Spousta, D. W. Miller, and R. Leitner, "Particle-level pileup subtraction for jets and jet shapes", *JHEP* **06** (2014) 092, arXiv:1403.3108.

[134] **CMS** Collaboration, "Determination of jet energy calibration and transverse momentum resolution in cms", *Journal of Instrumentation* **6** (2011), no. 11, P11002.

[135] W. R. Leo, "Techniques for Nuclear and Particle Physics Experiments: A How to Approach", Springer, 1987.

[136] W. Waltenberger, "Adaptive Vertex Reconstruction", Tech. Rep. CMS-NOTE-2008-033, CERN, Geneva, Jul 2008.

[137] R. Frühwirth, W. Waltenberger, and P. Vanlaer, "Adaptive Vertex Fitting", Tech. Rep. CMS-NOTE-2007-008, CERN, Geneva, Mar 2007.

[138] C. Weiser, "A Combined Secondary Vertex Based B-Tagging Algorithm in CMS", Tech. Rep. CMS-NOTE-2006-014, CERN, Geneva, Jan 2006.

[139] **CMS** Collaboration, "CMS JEC Run I legacy performance plots", CMS Detector Performance Note CMS-DP-2015-044, CERN, 2015.

[140] **CMS** Collaboration, "Measurement of jet fragmentation into charged particles in *pp* and PbPb collisions at $\sqrt{s_{NN}} = 2.76$ TeV", *JHEP* **10** (2012) 087, arXiv:1205.5872.

[141] **CMS** Collaboration, "Measurement of jet fragmentation in PbPb and pp collisions at $\sqrt{s_{NN}} = 2.76$ TeV", *Phys. Rev. C* **90** (2014) 024908, arXiv:1406.0932.

[142] **CMS** Collaboration, "Correlations between jets and charged particles in PbPb and pp collisions at $\sqrt{s_{\mathrm{NN}}} = 2.76$ TeV", *JHEP* **02** (2016) 156, arXiv:1601.00079.

[143] B. Alver *et al.*, "Importance of correlations and fluctuations on the initial source eccentricity in high-energy nucleus-nucleus collisions", *Phys. Rev.* **C77** (2008) 014906, arXiv:0711.3724.

[144] M. Spousta, "Flavor aspects of parton energy loss", in "The 8th International Conference on Hard and Electromagnetic Probes of High-energy Nuclear Collisions". 2016.

université PARIS-SACLAY | ÉCOLE DOCTORALE PHENIICS

Titre : L'asymmétrie de l'impulsion transverse des paires des jets de b dans les collisions d'ions lourds dans l'expérience CMS au LHC

Mots clefs : plasma de quarks et de gluons, jets b, l'asymmétrie de l'impulsion transverse, perdre d'énergie de partons

Résumé : Les collisions d'ions lourds à haute énergie produisent un nouvel état de la matière appelé le plasma de quarks et de gluons. Un parton traversant le plasma perds de l'énergie, en atténuant les gerbes hadroniques : c'est l'effet de "jet quenching". La dépendance du jet quenching dans la saveur du parton fournit des contraintes sur les modèles de perte d'énergie. Le déséquilibre d'une paire de jets issus de quarks b est une observable appropriée pour étudier ce phénomène. Cette thèse présente la mesure du déséquilibre en impulsion transverse des jets de b et des jets inclusifs (non-identifiés), dans des collisions PbPb a $\sqrt{s_{NN}} = 5.02$ TeV, réalisée avec le détecteur CMS au LHC pour une luminosité intégrée de 404 μb^{-1}. Aucune différence n'est observée dans le jet quenching entre les jets issus de partons légers et lourds. Une analyse des résultats à l'aide d'un modèle simple de perte d'énergie est présentée.

Title : Transverse momentum balance of b-jet pairs in heavy ion collisions with the CMS experiment at the LHC

Keywords : Quark gluon plasma, b-jets, transverse momentum imbalance, parton energy loss

Abstract : The collisions of heavy ions at high energy produce the new state of matter called the quark gluon plasma. A parton traversing the plasma loses its energy which results in the jet quenching phenomenon. The dependence of the jet quenching on the parton flavor provides constraints the models describing energy loss. The imbalance of b-jets is a very suitable observable to study this phenomena. This dissertation presents the measurement of the transverse momentum imbalance of b-jets and inclusive (non-identified) jets in PbPb collisions at $\sqrt{s_{NN}} = 5.02$ TeV which is performed with the CMS detector at the LHC with total integral luminosity of 404 μb^{-1}. No significant difference in jet quenching between light and heavy flavor jets is observed. The interpretation of results with a simple model of energy loss is performed.

Université Paris-Saclay
Espace Technologique / Immeuble Discovery
Route de l'Orme aux Merisiers RD 128 / 91190 Saint-Aubin, France